CHEMISTRY OF SOFC CATHODE SURFACES: FUNDAMENTAL INVESTIGATION AND TAILORING OF ELECTRONIC BEHAVIOR

Final Technical Report

Report period stop/start date: October 1, 2008 – September 30, 2013

Principal Author/s: PI: BILGE YILDIZ, MIT, CO-PI CLEMENS HESKE, UNLV

Date report was issued (month/year): 03-2014

DOE award number: DE–NT0004117

Name/address of submitting organization: Massachusetts Institute of Technology, 77 Massachusetts Avenue, Cambridge, MA 02139.

Disclaimer: This report was prepared as an account of work sponsored by an agency of the United States Government. Neither the United States Government nor any agency thereof, nor any of their employees, makes any warranty, express or implied, or assumes any legal liability or responsibility for the accuracy, completeness, or usefulness of any information, apparatus, product, or process disclosed, or represents that its use would not infringe privately owned rights. Reference herein to any specific commercial product, process, or service by trade name, trademark, manufacturer, or otherwise does not necessarily constitute or imply its endorsement, recommendation, or favoring by the United States Government or any agency thereof. The views and opinions of authors expressed herein do not necessarily state or reflect those of the United States Government or any agency thereof.

Abstract:

This project had three key contributions as summarized here:

1) Electron tunneling characteristics on $La_{0.7}Sr_{0.3}MnO_3$ (LSM) thin-film surfaces were studied up to 580°C in 10^{-3}mbar oxygen pressure, using scanning tunneling microscopy/ spectroscopy (STM/STS). A threshold-like drop in the tunneling current was observed at positive bias in STS, which is interpreted as a unique indicator for the activation polarization in cation oxygen bonding on LSM cathodes**.** Sr-enrichment was found on the surface at high temperature using Auger electron spectroscopy, and was accompanied by a decrease in tunneling conductance in STS. This suggests that Sr-terminated surfaces are less active for electron transfer in oxygen reduction compared to Mn-terminated surfaces on LSM.

2) Effects of strain on the surface cation chemistry and the electronic structure are important to understand and control for attaining fast oxygen reduction kinetics on transition metal oxides. Here, we demonstrate and mechanistically interpret the strain coupling to Sr segregation, oxygen vacancy formation, and electronic structure on the surface of $La_{0.7}Sr_{0.3}MnO_3$ (LSM) thin films as a model system. Our experimental results from x-ray photoelectron spectroscopy and scanning tunneling spectroscopy are discussed in light of our first principles-based calculations. A stronger Sr enrichment tendency and a more facile oxygen vacancy formation prevail for the tensile strained LSM surface. The electronic structure of the tensile strained LSM surface exhibits a larger band gap at room temperature, however, a higher tunneling conductance near the Fermi level than the compressively strained LSM at elevated temperatures in oxygen. Our findings suggest lattice strain as a key parameter to tune the reactivity of perovskite transition metal oxides with oxygen in solid oxide fuel cell cathodes.

3) Cation segregation on perovskite oxide surfaces affects vastly the oxygen reduction activity and stability of solid oxide fuel cell (SOFC) cathodes. A unified theory that explains the physical origins of this phenomenon is therefore needed for designing cathode materials with optimal surface chemistry. We quantitatively assessed the *elastic* and *electrostatic* interactions of the dopant with the surrounding lattice as the key driving forces for segregation on model perovskite compounds, LnMnO$_3$ (host cation Ln=La, Sm). Our approach combines surface chemical analysis with X-ray photoelectron and Auger electron spectroscopy on model dense thin films, and computational analysis with density functional theory (DFT) calculations and analytical models. Elastic energy differences were systematically induced in the system by varying the radius of the selected dopants (Ca, Sr, Ba) with respect to the host cations (La, Sm) while retaining the same charge state. Electrostatic energy differences were introduced by varying the distribution of charged oxygen and cation vacancies in our models. Varying the oxygen chemical potential in our experiments induced changes in both the elastic energy and electrostatic interactions. Our results quantitatively demonstrate that the mechanism of dopant segregation on perovskite oxides includes *both* the elastic and electrostatic energy contributions. A smaller size mismatch between the host and dopant cations and a chemically expanded lattice were found to reduce the segregation level of the dopant and to enable more stable cathode surfaces. Ca-doped $LaMnO_3$ was found to have the most stable surface composition with the least cation segregation among the compositions surveyed. The diffusion kinetics of the larger dopants, Ba and Sr, was found to be slower, and can kinetically trap the segregation at reduced

temperatures despite the larger elastic energy driving force. Lastly, scanning probe image-contrast showed that the surface chemical heterogeneities made of dopant oxides upon segregation were electronically insulating. The consistency between the results obtained from experiments, DFT calculations and analytical theory in this work provides a predictive capability to tailor the cathode surface compositions for high-performance SOFCs.

Table of Contents:

Electron Tunneling Characteristics on La0.7Sr0.3MnO3 Thin-Film Surfaces at High Temperature… p: 1-11

New Insights into the Strain Coupling to Surface Chemistry, Electronic Structure and Reactivity of La0.7Sr0.3MnO3… p:12-23

Cation size mismatch and charge interactions drive dopant segregation at the surfaces of manganite perovskites…. p:24-65

Characterization of the Surface Electronic Structure of Thin-Film Solid Oxide Fuel Cell Cathodes…. p:66-77

Electron Tunneling Characteristics on $La_{0.7}Sr_{0.3}MnO_3$ Thin-Film Surfaces at High Temperature

Khabiboulakh Katsiev[1], Bilge Yildiz[1*], Balasubramaniam Kavaipatti[2], and Paul A. Salvador[2]

[1]Department of Nuclear Science and Engineering, Massachusetts Institute of Technology, 77 Massachusetts Avenue, Cambridge, MA 02139, USA.

[2]Department of Materials Science and Engineering, Carnegie Mellon University, 149 Roberts Eng. Hall, Pittsburgh, PA 15213, USA.

*byildiz@mit.edu

We report on the electron tunneling characteristics on $La_{0.7}Sr_{0.3}MnO_3$ (LSM) thin-film surfaces up to 580°C in 10^{-3}mbar oxygen pressure, using scanning tunneling microscopy/ spectroscopy (STM/STS). A threshold-like drop in the tunneling current was observed at positive bias in STS, which is interpreted as a unique indicator for the activation polarization in cation-oxygen bonding on LSM cathodes**.** Sr-enrichment was found on the surface at high temperature using Auger electron spectroscopy, and was accompanied by a decrease in tunneling conductance in STS. This suggests that Sr-terminated surfaces are less active for electron transfer in oxygen reduction compared to Mn-terminated surfaces on LSM.

Perovskite-type mixed ionic-electronic conductor (MIEC) oxides are widely used as Solid Oxide Fuel Cell (SOFC) cathodes,[1] and their surface structure plays an important role in the electrocatalytic activity for oxygen reduction (OR).[2,3] A particularly interesting material in this context is $La_{(1-x)}Sr_xMnO_{3+\delta}$ (LSM)[4,5] – an MIEC with poor ionic conductivity. The underlying OR mechanisms involving electronic and ionic charge transport on SOFC cathodes are not fully understood[2], and the impact of different metal cations on the catalytic properties of the surface remains unclear.[6] Consequently, an improved understanding of the surface electronic and chemical state and its relation to the OR at the atomistic level is essential to the design of cathodes with enhanced electrocatalytic activity. In doing so, probing the surface electronic properties in conditions representative of the reaction temperatures and pressures is needed.[7]

We investigated the correlations of the surface composition of $La_{0.7}Sr_{0.3}MnO_3$ (LSM) model dense thin-films to their surface electronic structure and electronic and ionic exchange characteristics. We deployed an *in situ* approach combining surface sensitive probes of electronic structure and chemical state on the thin films – scanning tunneling microscopy and spectroscopy (STM/STS) and Auger electron spectroscopy (AES). Utilizing these surface sensitive probes, particularly the STM/STS, at as high temperatures and non-UHV conditions is thus far unique, and facilitates to relate the chemical and electronic state of the model cathode surfaces closely to the reaction environment of operational SOFC cathodes.

$La_{0.7}Sr_{0.3}MnO_3$ polycrystalline dense thin films of 10-100nm thickness were grown on single crystal (111) Yttria-stabilized Zirconia (YSZ) by pulsed laser deposition (PLD) at 800°C in 50 mTorr of O_2, and subsequently cooled to room temperature in 300 Torr O_2.[8]

The structural, electronic and compositional characterizations were performed in a UHV surface science system (by Omicron GmbH). The analysis chamber is equipped with a variable-

temperature AFM/STM (Omicron VT25), retractable low-energy electron diffraction (LEED) optics, electron gun and a cylindrical mirror energy analyzer (CMA) for AES. Auger electron spectra were acquired using a normal incidence 4.8keV electron beam. The samples were radiatively heated by a Pyrolytic Boron Nitride (PBN) heater during the annealing in oxygen for cleaning the surface, and the high temperature STM/STS and AES experiments. The heaters were degassed for cleanliness at high temperature prior to the experiments. A retractable oxygen doser equipped with a high precision leak valve was used for direct dosing the sample surface with oxygen during STM imaging and STS measurements. This set-up allowed to create a 10^{-3}mbar oxygen pressure, P_{O2}, localized in the vicinity of the sample's surface while the chamber base was at $P_{O2}=10^{-6}$mbar. AES to probe the sample cleanliness were performed at ~$2x10^{-10}$mbar at ambient temperature. AES to identify the relative changes in the La, Sr, and Mn content on the surface were performed at $P_{O2}=10^{-6}$ mbar in the chamber at sample temperatures from 20°C to 700°C.

The *in situ* cleaning of the as-grown films was performed by heating the samples to 500°C in oxygen at $P_{O2}=5x10^{-7}$ mbar for 30 min, which resulted in a significant reduction of the carbon adsorbates below the detection limit of the AES energy analyzer. STM at room temperature and high temperatures was performed in the constant-current mode using 80%Pt-20%Ir tips, with the tunneling current, *I*, in the 0.1 to 1 nA range and the sample at a bias voltage, *V*, in the -1 to 3V range. During the STS measurements, the bias voltage was varied from -3V to 3V in 20mV steps, with an acquisition time of 0.6 or 20 ms per voltage step for the I-V and dI/dV data, respectively. All the I-V curves discussed here represent an average behavior over the 15-20 subsequent spectra.

The STM performed on the 50nm-thick LSM film at room temperature (Fig. 1(a)) showed a textured surface structure. Two types of grains coexisted, without an apparent crystallographic orientation in the topographic images. First is the large island-type flat grains, with a size distribution from 70 to140nm, and clearly distinguishable step edges. The second type consists of smaller grains, with a size distribution from 30 to 50nm. The overall peak-to-valley height difference is 6 nm. The LSM film structure did not evidently change via grain coarsening or surface roughening during the STM/STS experiments at 580°C in $P_{O2}=10^{-3}$ mbar (Fig. 1(b)) lasting up to 24 hours. The optimized conditions allowing for high resolution imaging, down to step-edges (inset Fig.1(b)) at high temperature in non-UHV conditions were obtained. This was necessary for the STS measurements to stably probe the electronic properties of the LSM surface. All results presented in this paper belong to this specific sample.

Temperature-dependent *in situ* AES measurement in $P_{O2}=10^{-6}$mbar revealed enrichment of Sr and decrease of La on the surface (Fig.2(a)), resulting in an overall 15-27% increase in the (La+Sr)/Mn ratio at 600-700°C (Fig.2(b)). Particularly due to the significant increase in the (La+Sr)/Mn ratio above 1.0 accompanied with the Sr-enrichment, we attribute this evolution to a thermodynamically favored Sr-rich phase on the LSM surface during the AES experiment conditions. This observation is consistent with prior experimental results which report Sr segregation on the LSM surface[9,10] measured at room temperature in UHV conditions upon high temperature annealing in air, and often accompanied by changes in the Mn valence state.[11] Furthermore, these results are supported by recent *ab initio* hybrid density-functional calculations,[12] which predict the stable coexistence of (Sr,La)O- and MnO_2-phases on the surface at room temperature and the (Sr,La)O-phase on the surface as energetically more favorable at 800°C and $P_{O2}=0.2$ atm on LSM.

Electronic tunneling current on LSM surface exhibited a semiconductor-like band-gap behavior at room temperature and a metallic nature at 400-580°C (Fig. 3(a) and 3(b), acquisition time of 0.6 ms per voltage step). An increase in the tunneling conductance was found as the temperature increased to 400°C and 500°C, followed by a decrease at 580°C. The increase in the tunneling conductance reflected in the transition from a large band-gap (2.6eV) to metallic nature can't be caused mainly by the effect of the elevated temperature on a semiconductor.[13] Thermal excitation at 400°C is well below 2.6eV energy and cannot enable the transition to a metallic conductance in this case. While yet uncertain, we hypothesize that this transition is due to a structural transformation on the surface; for example, from an orthorhombic phase characterized by a strong Jahn–Teller distortion as an insulating paramagnetic state to a rhombohedral phase with a ferromagnetic metallic state.[14,15] The subsequent decrease in conductance from 500 to 580°C can also result from the thermodynamically driven changes in the surface structure and composition of the LSM. While no diffraction pattern was observed by LEED in this work, we identified a chemical change associated with Sr-segregation and A-site/B-site ratio changes on LSM surface, as discussed above for the temperature-dependent AES results (Fig. 2).

Electronic conductance of the LSM is associated with the Mn cation and its oxidation state. A p-type conductivity in LSM arises as a result of hole-doping through the increase in Mn^{4+}/Mn^{3+} ratio,[16] which depends on the A-site cation substitution and oxygen non-stoichiometry. We attribute the decreasing tunneling conductance measured with STS at 580°C (Fig. 3) to the evolution of a Sr-rich phase accompanied by the relative decrease of Mn on the surface as probed by AES at comparable conditions (Fig. 2). This result suggests that the A-site rich and Mn-poor surfaces are less active for electron exchange in oxygen reduction on LSM. We note that the STS and AES experiments reported here were carried out at different oxygen

pressures, 10^{-3}mbar and 10^{-6}mbar for STS and AES, respectively. $La_{0.7}Sr_{0.3}MnO_3$ retains oxygen stoichiometry between $P_{O2}=10^{-7}$-10^{-3}mbar at 800°C, and that this pressure decreases with lower temperature,[17] as in the experiments reported here. Therefore, both the AES and STS oxygen pressure conditions reported here are expected to retain similar oxygen stoichiometry on LSM, and thus the comparison between the AES and STS results are valid qualitatively.

The STS measured within the range from -3 V to +3 V with 20 ms acquisition time per voltage step at $P_{O2}=10^{-3}$mbar and elevated temperatures revealed a sudden drop in the tunneling current at a positive threshold bias (Fig. 4(a)). This differs from the STS spectra acquired with 0.6ms per voltage step (Fig. 3(b)). The threshold bias, V_{th}, decreased with increasing temperature, and was 2.6, 2.3, and 1.5 V at 400°C, 500°C, and 580°C, respectively (Fig. 4(b)). Similar threshold behavior was also observed on the 10 and 100 nm-thick LSM films (not reported here). STM imaging and the STS I-V spectra with the 0.6 ms acquisition-time was fully reproduced following the tunneling current drop in scans with a 20 ms acquisition time, thus proving that the tip was not altered.

The acquisition-time-, temperature-, and bias-dependent character of the tunneling drop on LSM suggests that the underlying phenomenon is an activated chemical reaction; with the acquisition time-dependence related to the yield, and the temperature- and bias-dependence related to the activation of the reaction. Since the surface is expected to have oxygen vacancies at high temperature, but investigated in a P_{O2} environment, we suggest that this chemical reaction might be a localized oxidation induced by the tunneling bias. While here we report this behavior for the first time for a perovskite surface at high temperature, a similar tip-induced nanometric oxidation accompanied by the drop in tunneling conductance was extensively studied for Si and GaAs surfaces at room temperature.[18,19] The observation for the bias-induced oxidation was

supported by an analytical model based on the Cabrera-Mott theory.[20] In the LSM surface region, positive bias leads to an upward bending of the electronic bands[21] and shifts the cation electronic states to higher energy, as schematically shown in Fig. 4(b) inset. The bias-induced band bending can increase the catalytic activity, resulting in the oxygen chemisorption localized at the tip – LSM surface region at high temperature. The consequent formation of oxidized sites is a possible mechanism explaining the tunneling drop in STS shown in Fig. 4. Recent *ab initio* studies[6,22] indicate that the favorable site for oxygen binding on LSM surface is atop Mn-cation. The valence band maximum of LSM (from -3 to 0 eV) consists of Mn(3*d*)-derived states that are split into t_{2g} and e_g bands.[14,23] Due to the p-type conductivity of LSM, the electron transfer to oxygen should take place from the t_{2g} levels.[24] The upward shift in the relative energies (Fig. 4(b)) of these Mn(3*d*)-derived states can increase the activity for the reaction with oxygen from the gas phase.[25,26] Based on this mechanism, we suggest that the threshold bias can serve as a unique probe of the activation polarization in cation-oxygen bonding on LSM cathode surface.

In summary, we investigated the electron tunneling characteristics on LSM thin-film surfaces using STM/STS up to 580°C in oxygen gas environment. To the best of our knowledge, this is the first STM/STS investigation of LSM at as high temperatures and non-UHV conditions close to the reaction environment of operational SOFC cathodes. A threshold-like drop in the tunneling current was observed at positive bias in STS at high temperature, and is interpreted as a unique indicator for the activation polarization in cation-oxygen bonding on the surface. AES revealed Sr-enrichment on the surfaces from 500 to 700°C, and was accompanied by a decrease in tunneling conductance in STS. This suggests that the Mn-terminated surfaces are more active for electron transfer in oxygen reduction compared to the Sr-rich surfaces on LSM. These

findings can contribute to the atomic-scale understanding of the electrocatalytic properties on LSM cathodes, and serve as a key for the design of desirable cathodes for SOFCs.

We thank Department of Energy Office of Fossil Energy for financial support under award no. DE–NT0004117, and Clemens Heske and Hoydoo You for constructive discussions. This work was performed in part at the Center for Nanoscale Systems, which is supported by the National Science Foundation under award no. ECS-0335765.

[1] S. C. Singhal, Solid State Ionics **135**, 305 (2000).

[2] S. B. Adler, Chem. Rev. **104,** (10) 4791 (2004)

[3] F. S. Baumann, J. Fleig, M. Konuma, U. Starke, H.-U. Habermeier, and J. Maier, J. Electrochem. Soc. **152,** (10) A2074 (2005)

[4] V. Brichzin, J. Fleig, H.-U. Habermeier, G. Cristiani, and J. Maier, Solid State Ionics **499,** 152 (2002)

[5] G. J. la O', B. Yildiz, S. McEuen, and Y. Shao-Horn, J. Electrochem. Soc. **154,** (4) B427 (2007)

[6] Y.-L. Lee, D. Morgan, J. Kleis, and J. Rossmeisl, Proc. of the 214th Meeting of the Electrochem. Soc., Hawaii, USA, October 2008

[7] A. Kolmakov and D.W. Goodman, Catal. Lett. 7**0,** 93 (2000)

[8] K. R. Balasubramaniam, S. Havlia, P. A. Salvador, H. Zheng, and J. Mitchell, Appl. Phys. Lett. **91**, 232901 (2007)

[9] H. H. Kumigashira, K. Horiba, H. Ohguchi, K. Ono, M. Oshima, N. Nakagawa M. Lippmaa, M. Kawasaki, and H. Koinuma, Appl. Phys. Lett. **82**, 3430 (2003).

[10] R. Bertacco, J.P. Contour, A. Barthelemy, and J. Olivier, Surf. Sci. **511,** 366 (2002).

[11] M. Backhaus-Ricoult, Solid State Ionics **177**, 2195 (2006).

[12] S. Piskunov, E. Heifets, T. Jacob, E. A. Kotomin, D. E. Ellis, and E. Spohr, Phys. Rev. B **78**, 121406R (2008)

[13] K. Seeger "Semiconductor physics: an introduction" 9th Edition, Springer (2004)

[14] A. Urushibara, Y. Moritomo, T. Arima, A. Asamitsu, G. Kido, and Y. Tokura, Phys. Rev. B **51,** 14103 (1995)

[15] M. P. de Jong, V. A. Dediu, C. Taliani, and W. R. Salaneck, J. Appl. Phys. **94**, 7292 (2003)

[16] C. Zender, Phys. Rev. **82,** 403 (1951)

[17] J. Mizusaki, Y. Yonemura, H. Kamata, K. Ohyama, N. Mori , H. Takai , H. Tagawa , M. Dokiya , K. Naraya, T. Sasamoto , H. Inaba , and T. Hashimoto, Solid State Ionics **132**, 167 (2000)

[18]Y. Okada, Y. Iuchi, M. Kawabe, and J. S. Harris Jr., J. Appl. Phys. **88**, 1136 (2000)

[19] D. Stievenard and B. Legrand, Progr. Surf. Sci. **81**, 112 (2006)

[20] J. A. Dagata, F. Perez-Murano, G. Abadal, K. Morimoto, T. Inoue, J. Itoh, and H. Yokoyama, Appl. Phys. Lett. **76**, 2710 (2000)

[21] R. M. Feenstra, Y. Dong, M. P. Semtsiv, and W. T. Masselink, Nanotech. **18,** 044015 (2007)

[22] Y. Choi, M. C. Lin, and M. Liu, Angew. Chem. Int. Ed. **46**, 7214 (2007)

[23] A. Chikamatsu, H. Wadati, H. Kumigashira, M. Oshima, A. Fujimori, N. Hamada, T. Ohnishi, M. Lippmaa, K. Ono, M. Kawasaki, and H. Koinuma, Phys. Rev. B **73**, 195105 (2006)

[24] H. Kamata, Y. Yonemura, J. Mizusaki, H. Tagawa, K. Narayato and T. Sasamoto, J. Phys. Chem. Solids **56**, 943 (1995)

[25] Ph. Avouris, R. E. Walkup, A. R. Rossi, H. C. Akpati, P. Nordlander, T. -C. Shen, G. C. Abeln and J. W. Lyding, Surf. Sci. **363,** 368 (1996)

[26] O Bikondoa, CL Pang, R Ithnin, CA Muryn, H Onishi, and G Thornton, Nat. Mater. **5,** 189 (2006)

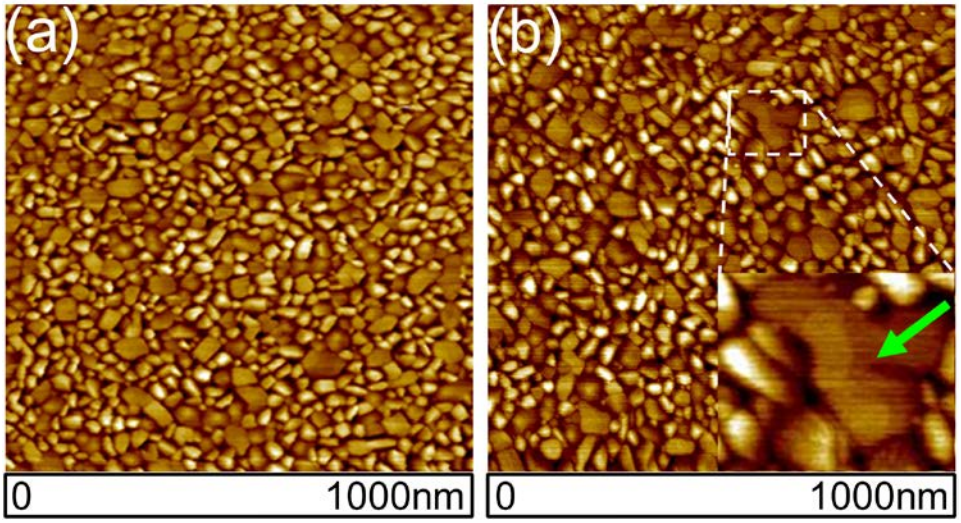

Figure 1. (Color online) Topography (1x1 μm^2) of the 50nm-thick dense thin-film LSM surface imaged with tunneling conditions of 2 V and 1 nA at (a) room temperature in ultra-high vacuum, and (b) 580°C, $P_{O2}=10^{-3}$ mbar. The inset, 150x137 nm^2, in (b) shows the step-edge resolution on the island-type flat grains (the location of the inset is shown by dashed lines).

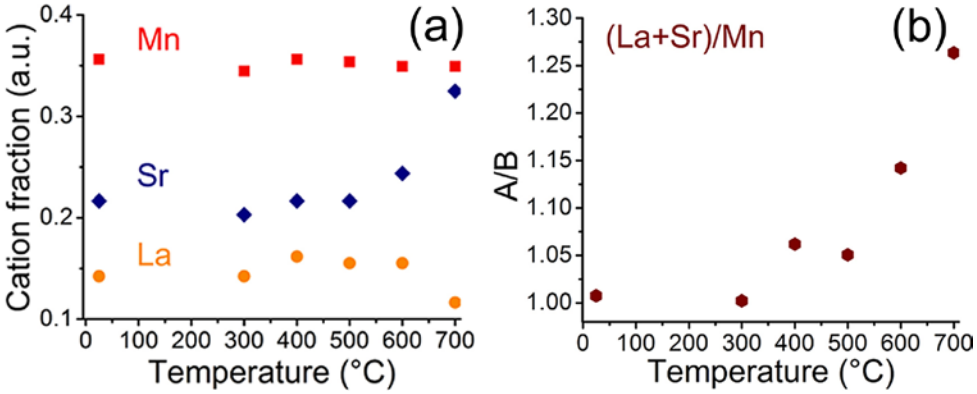

Figure 2. (Color online) Temperature dependent AES in 10^{-6} mbar oxygen pressure revealed (a) Sr enrichment, accompanied by a decrease in La at the surface above 500°C, while Mn remained unchanged. (b) (La+Sr)/Mn ratio showed an overall relative increase in the A site cations. The quantification in the AES data was performed based on the La_{MNN}, Sr_{LMM}, Mn_{LMM}, and O_{KLL} transitions. The error bar range in the experimental data was estimated to be <2%.

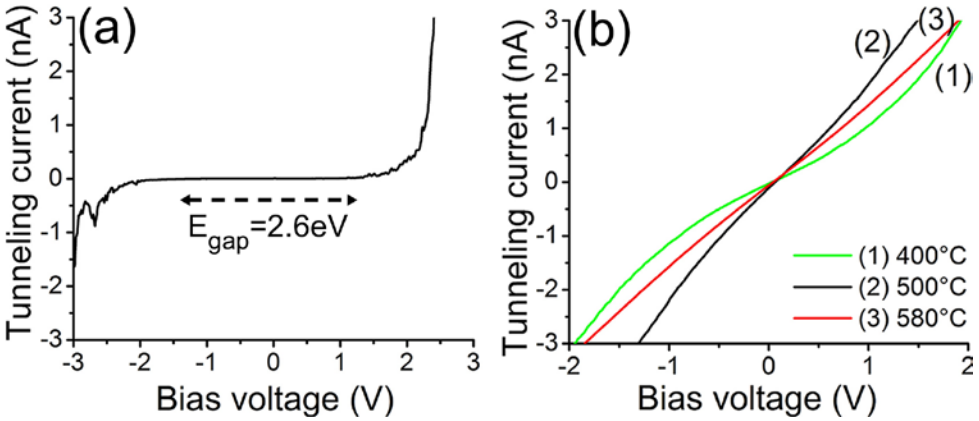

Figure 3. (Color online) Tunneling current spectra acquired on the surface of the 50 nm-thick LSM at (a) room temperature, and (b) 400, 500 and 580°C with the acquisition time of 0.6 ms per voltage step.

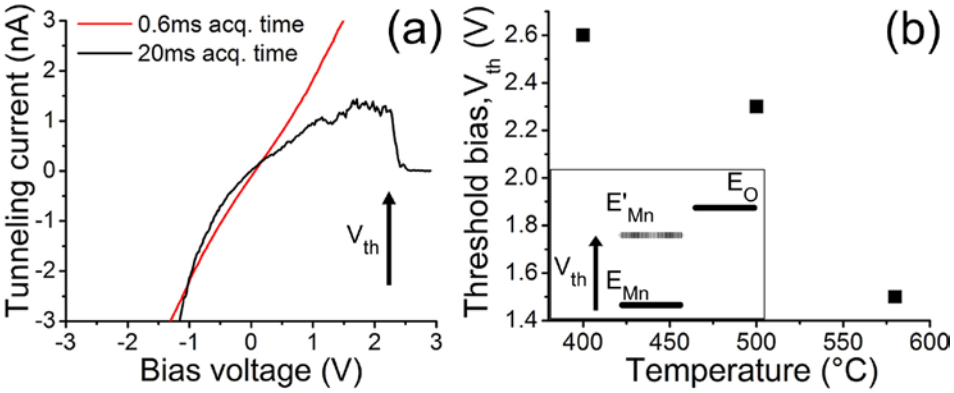

Figure 4. (Color online) (a) Tunneling conductance spectra acquired on the surface of the 50nm-thick LSM at 580°C (acquisition time of 0.6 and 20 ms per voltage step), and (b) the threshold bias as a function of temperature. The inset in (b) schematically shows the cation energy levels (E_{Mn}) shifting upward (E'_{Mn}) at positive bias, and approaching the oxygen electronic levels (E_O).

New Insights into the Strain Coupling to Surface Chemistry, Electronic Structure and Reactivity of $La_{0.7}Sr_{0.3}MnO_3$

Helia Jalili[1†], Jeong Woo Han[1,2†], Yener Kuru[1,2,3], Zhuhua Cai[1,2], and Bilge Yildiz[1,2*]

[1]*Laboratory for Electrochemical Interfaces,* [2]*Department of Nuclear Science and Engineering,*
[3]*Department of Materials Science and Engineering,*
Massachusetts Institute of Technology, 77 Massachusetts Avenue, Cambridge, MA 02139, USA

Abstract

Effects of strain on the surface cation chemistry and the electronic structure are important to understand and control for attaining fast oxygen reduction kinetics on transition metal oxides. Here, we demonstrate and mechanistically interpret the strain coupling to Sr segregation, oxygen vacancy formation, and electronic structure on the surface of $La_{0.7}Sr_{0.3}MnO_3$ (LSM) thin films as a model system. Our experimental results from x-ray photoelectron spectroscopy and scanning tunneling spectroscopy are discussed in light of our first principles-based calculations. A stronger Sr enrichment tendency and a more facile oxygen vacancy formation prevail for the tensile strained LSM surface. The electronic structure of the tensile strained LSM surface exhibits a larger band gap at room temperature, however, a higher tunneling conductance near the Fermi level than the compressively strained LSM at elevated temperatures in oxygen. Our findings suggest lattice strain as a key parameter to tune the reactivity of perovskite transition metal oxides with oxygen in solid oxide fuel cell cathodes.

Table of Contents Graphic

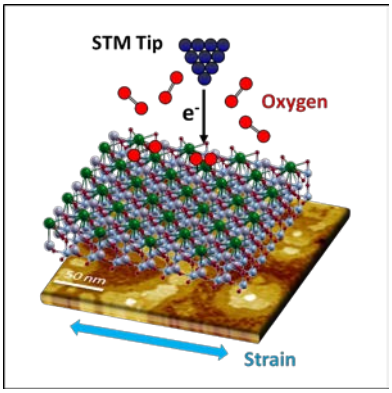

Keywords – Perovskite oxide, strain, surface, segregation, electronic structure, scanning tunneling microscopy, density functional theory

* To whom correspondence should be addressed. Email: byildiz@mit.edu
†These authors contributed equally to this work.

The relation of surface cation chemistry and surface electronic structure to oxygen reduction reaction (ORR) kinetics remains an outstanding question to this day in the search for highly active cathodes for Solid Oxide Fuel Cells (SOFCs). While traditionally perovskite type transition metal oxides have been extensively investigated as SOFC cathodes,[1,2] more recent studies highlight the potential of layered oxide cathodes.[3-5] On the surface of the perovskite structured $La_{1-x}Sr_xMnO_3$, a widely used and studied SOFC cathode material,[1,2,6-8] the fractional presence of constituent cations can deviate from the nominal bulk stoichiometry significantly,[9-13] due to an enrichment of Sr or La cations on the surface. It has been possible to control the bulk magnetic and electronic properties of perovskite thin films by manipulating their lattice parameters with different growth conditions, hydrostatic pressure, or use of substrates with a different lattice mismatch to the films.[14-18] Furthermore, impact of the lattice strain on the surface electronic structure and reactivity has been long demonstrated for low temperature noble metal electrocatalysts.[19,20] On the other hand, the role of lattice strain on the surface cation and anion chemistry, electronic structure and ionic transport, which all influence the ORR activity of SOFC-related oxides, is attracting its due interest only recently.

We have recently demonstrated, from first principles-based calculations, that the epitaxial strain up to a critical tensile strain value favors oxygen-vacancy formation as well as oxygen adsorption on another widely studied SOFC cathode, $LaCoO_3$.[21] Experiments validating the direct role of strain on the reactivity with oxygen and oxygen transport in SOFC materials have been yet scarce. Sase et al. showed that the oxygen surface exchange rate at the hetero-interface of $La_{0.6}Sr_{0.4}CoO_3$ / $(La,Sr)_2CoO_4$ thin films is larger by three orders of magnitude compared to the single-phase cobaltite surfaces.[22] A reasonable hypothesis that could explain the enhanced oxygen exchange at that interface region is the role of local strains. Studies on fluorite systems have suggested strong coupling of biaxial strain also to the oxygen ion diffusion.[23-25]

In this letter, we report our results, interpreted in light of our first principles-based calculations, on the strain-induced changes in the surface chemical and electronic state of $La_{0.7}Sr_{0.3}MnO_3$ (LSM) as a model system. We assessed two key parameters for reactivity with oxygen as a function of strain: 1) Chemical environment on the LSM surface, in particular the segregation of Sr cations; experimentally probed with angle resolved X-ray Photoelectron Spectroscopy, and computationally assessed through segregation energy calculations. 2) Surface electronic structure; experimentally probed using Scanning Tunneling Microscopy and Spectroscopy (both at ambient and *in situ* at elevated temperatures), and computationally predicted with *ab initio* calculations.

Epitaxial 10 nm thick LSM films, grown by pulsed laser deposition[26] on (001) $SrTiO_3$ (STO) and (001) $LaAlO_3$ (LAO), are the model materials in this study. The XRD results (Figure S1) indicate that both films are fully strained with the (001) out of plane orientation. The film on STO has approximately 0.8 % in-plane tensile strain whereas the film on LAO is under -2.1 % in-plane compression at room temperature. The expected strain in LSM films at the deposition temperature of

850 ^{o}C is +0.6 % and -2.3 % based on the differences of the thermal expansion coefficients of LSM, STO, and LAO. The surface of LSM films grown on both substrates, hereafter denoted as LSM/LAO and LSM/STO, has well-resolved and atomically smooth terraces with different lateral sizes (Figure 1-a, c). The height profiles on these terraces show that the height difference between each layer is 4.0±0.3 Å (Figure 1-b, d), in good agreement with the lattice parameter of the LSM (3.88 Å). The overall morphology on these two substrates is similar, while the size of these terraces on LSM/LAO is smaller.

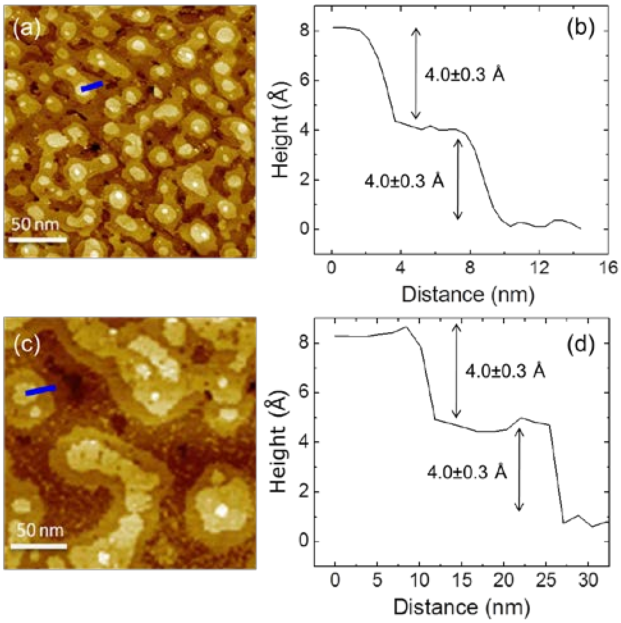

Figure 1: Surface morphology (a, c) and height profile (b, d) of the 10 nm thick LSM/LAO (a, b) and LSM/STO (c, d) films at room temperature. Blue bars in (a) and (c) show the position of the line profiles in (b) and (c).

The La 3*d*, La 4*d*, Sr 3*d* and Mn 2*p* emissions in XPS, normalized by their corresponding cross-sectional values, were used for assessing the relative presence of Sr on the A-site.[9,10] The La 4*d* and Sr 3*d* emissions have similar kinetic energies, with a mean free path (MFP) of 20 Å.[9] The La 3*d* and Mn 2*p* also have similar kinetic energies, with an MFP of 12 Å,[9] enabling a shallower probing depth near the surface compared to the La 4*d* and Sr 3*d*. These spectra were measured at two angles, 0° and 70°, between the surface normal and the detector position - measurements at 70° are more surface sensitive. To deduce the relative enhancement of Sr on/near the LSM surface, the Sr/(La+Sr) ratio was assessed using both the La 3*d* and the La 4*d* emissions, the $Sr_{3d}/(La_{4d}+Sr_{3d})$ and $Sr_{3d}/(La_{3d}+Sr_{3d})$ in Figure 2a and b, respectively, and the Mn/La ratio was assessed using the La 3*d* emission, the Mn_{2p}/La_{3d} in Figure 2c. All emissions reported in Figure 2 were evaluated at 70°. $Sr_{3d}/(La_{4d}+Sr_{3d})$, shown in Figure 2a, is almost the same, 0.36-0.37, on LSM/LAO and LSM/STO, and is larger than the bulk nominal value of Sr/(La+Sr)=0.3. This result implies that the near-surface

region of both LSM films is Sr–rich, and the total Sr fraction on the A-site within the top nearly 20 Å depth is the same regardless of the sign or magnitude of strain. By using the La_{3d} emission (photoelectrons with a 10 Å MFP, nearer the surface) in computing the $Sr_{3d}/(La_{3d}+Sr_{3d})$, a larger Sr/(La+Sr) value is found for LSM/STO (0.51+/- ???) compared to that for LSM/LAO (0.72+/- ???) (Figure 2b). This suggests a further enrichment of Sr, and an accompanying deficiency of La in the top few layers of the tensile strained LSM grown on STO. The Mn_{2p}/La_{3d} ratio (also with a MFP of 10 Å) in Figure 2c gives further evidence to the La deficiency on LSM/STO, and indirectly to the enhanced tendency of Sr segregation onto LSM/STO.

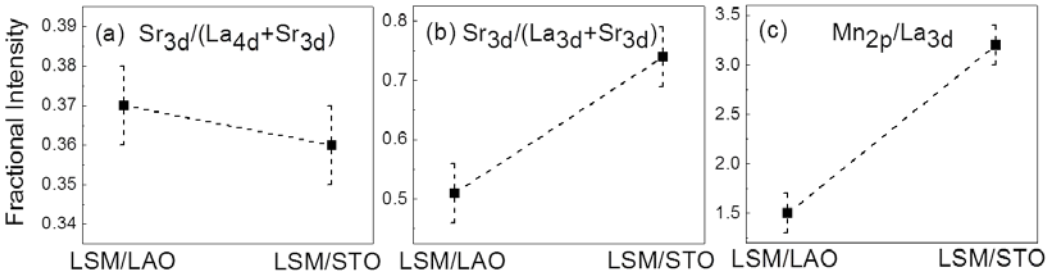

Figure 2: Relative intensities assessed from (a) $Sr_{3d}/(La_{4d}+Sr_{3d})$, (b) $Sr_{3d}/(La_{3d}+Sr_{3d})$ and (c) Mn_{2p}/La_{3d}, all normalized by the corresponding cross-sectional values, for LSM/LAO and LSM/STO, obtained from the spectra at the 70° emission angle. (The dashed lines are guide to the eye.)

We interpret the above result in light of our first principles-based calculations (in the framework of Density Functional Theory (DFT)) of Sr segregation energy, E_{seg}, and vacancy formation energy, E_{vac}, as a function of strain. We assessed two models, one with 25% (X_{Sr}=1/4) and another one 50% (X_{Sr}=1/2) Sr on the A site on the LSM surface as described with Figure S5 in Supplementary Information. We included the role of surface oxygen vacancies in the evaluation of E_{seg}, using the X_{Sr}=1/2 model. From the results shown in Figure 3a, we first note that Sr favors to segregate to the surface regardless of the amount and sign of strain from -3.5% to +2%. If an element's atomic size is larger and/or its cohesive energy is less than that of the other constituents, it segregates more easily to the surface.[27] Here, the ionic radius of Sr (1.12 Å) is larger than that of La (1.06 Å) and the surface tension of Sr (0.29 J/m^2), which is representative of its cohesive energy, is less than that of La (0.74 J/m^2).[28] In the range of strain values assessed here, the surface of the X_{Sr}=1/4 model (black curve) shows the stronger tendency to enrich Sr compared to the X_{Sr}=1/2 model (red curve). Steric hindrance effects between the dopants allows them to segregate more to the surfaces with low concentrations of Sr than with high concentrations.[29] Furthermore, surface oxygen vacancy induces Sr surface enrichment more strongly.[12,30] More importantly, for all three cases shown in Figure 3a, we predict that Sr segregation tendency increases as the strain increases from compressive (-3.5%) to tensile (up to 2%). Consistently with this, and as a potentially additional driving force for Sr enrichment, oxygen vacancy formation also becomes more facile in the same strain range. As

shown in Figure 3b, The oxygen vacancy formation is more favorable at the subsurface (MnO_2 layer) than on the top surface ((La,Sr)O layer), consistent with prior reports.[31] The strain response is qualitatively similar for both the top surface and the subsurface layer, and favors easier oxygen vacancy formation as the strain increases from compressive (-3.5%) to tensile (up to 2%). For explaining the increasing tendency of Sr enrichment with strain, we take the space change around a Sr atom as the key measure. Figure 3c shows the difference between the Sr-O bond length on the surface and the Sr-O bond length in the bulk, obtained from the LSM model with X_{Sr}=1/4 (Figure 3d) as a function of strain. As the strain increases from compressive to tensile, the Sr-O bond length on the LSM surface is stretched relatively more than that in the bulk. This creates relatively more space on the surface, as shown by the increase of Δd(Sr-O). Relatively larger available space may enable easier substitution of Sr on the surface, and thus, lower the segregation energy. These first principles-based calculations qualitatively support and explain our experimental observations in Figure 2, favoring more Sr on the surface of tensile strained LSM/STO. Our experimental and theoretical results are qualitatively in good agreement and clearly show that the tensile strain facilitates Sr segregation to the surface of LSM while the compressive strain relatively suppresses this behavior.

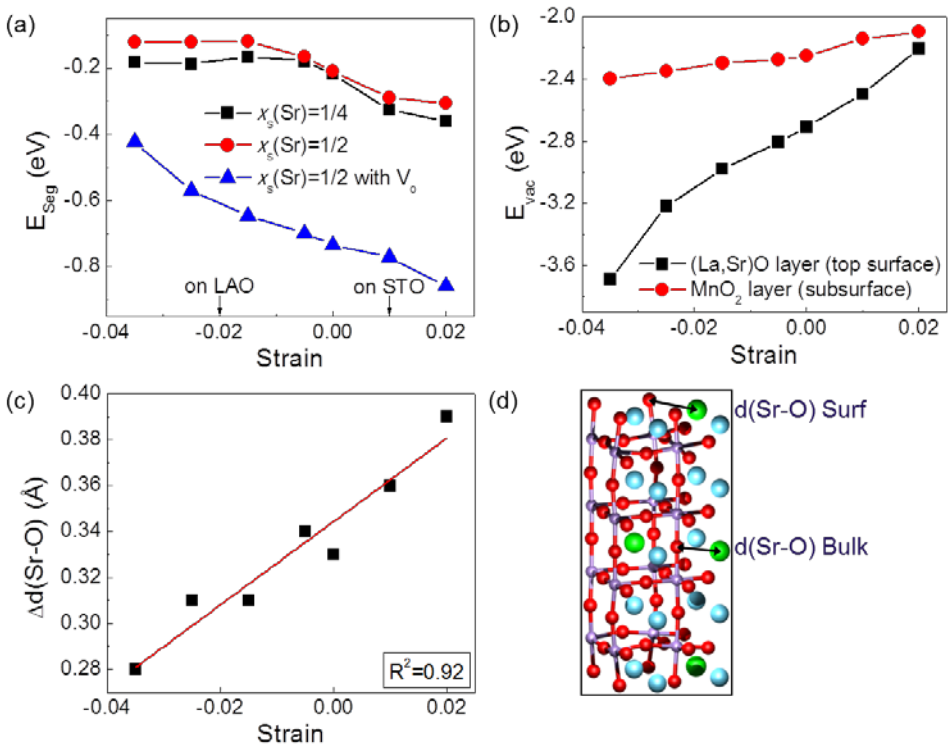

Figure 3: (a) Surface segregation energies of Sr calculated from the LSM models with X_{Sr}=1/4, X_{Sr}=1/2, and X_{Sr}=1/2 including a surface oxygen vacancy under different strain states. By our definition, a more negative E_{seg} favors the Sr more strongly on the surface compared to in the bulk. (b) Oxygen vacancy formation energy as a function of strain calculated from the LSM model with X_{Sr}=1/2, including one oxygen vacancy formed at the LaO layer (top surface) or at the MnO_2 layer (subsurface). By our definition, a less negative E_{vac} favors the formation of vacancy more easily on the surface. (c) the difference between the Sr-O bond length on the surface, d(Sr-O)Surf, and the Sr-O

bond length in the bulk, d(Sr-O)Bulk, as a function of strain, and (d) the Sr-O bond lengths shown in the unit cell.

Electronic structure is strongly coupled to the surface reactivity of the material.[32] Here we compare the electronic density of states using tunneling spectroscopy, probing the occupied and unoccupied states on LSM surfaces near the Fermi level both at room temperature and at an elevated temperature in oxygen. LSM surfaces at room temperature exhibited an energy gap between the occupied (negative sample bias) and unoccupied (positive sample bias) states (Figure 4a), with a smaller gap of 0.9±0.2 eV on LSM/LAO compared to 2.1±0.2 eV on LSM/STO. In prior tunneling studies on LSM and related perovskite thin films, differences in electronic characteristics at room temperature or below were attributed to the co-existence of paramagnetic insulating and ferromagnetic metallic regions on the surface, and were related to the differences in the local Mn-O bond lengths, nanoscopic disorder,[33] oxidation,[34] and formation of oxygen vacancy defects.[35] We note that our LSM films of ~10nm thickness are fully strained and the observation of semiconducting-like energy gap at room temperature is in good agreement with previous reports on fully strained manganite films,[34,36] and with our recent work[13,37] on textured LSM films on zirconia substrates with a large lattice mismatch to LSM. The larger band gap found on LSM/STO compared to that on LSM/LAO may, in part, be related directly to the strain state differences (both magnitude and sign) on these films.

We assess the qualitative and direct relation between the epitaxial lattice strain and the electronic structure, in particular the energy gap, on LSM surface by performing density of states (DOS) calculations on LSM (001). Previous DFT calculations show that LSM is half-metallic at 0 K.[38,39] To overcome or minimize the 0K-limitation in comparing the DOS predictions to our experimentally measured DOS at finite temperature, we need to at least represent the finite temperature magnetism of LSM[38] in our simulations. For this purpose, we imposed in our models the spin states of Mn (μ_B=1.0) known to be predominant at room temperature.[40] This approach allows us to model the LSM closer to its finite temperature structure[41] than the 0K ground state. As shown in Figure S6, the total DOS for each strain in LSM has a band gap, implying that our approach represents the band gap character of LSM at room temperature. Although our calculation results do not match quantitatively to our experimentally measured values of the energy gap, they qualitatively capture the trend that the band gap increases as the epitaxial strain changes from compressive to tensile (Figure 4b). It is known that DFT systemically underestimates band gaps due to the inherent lack of derivative discontinuity and delocalization errors, but the resulting qualitative trends are considered reliable.[42] The strain dependence of the energy gap that we obtained by the DFT calculations is therefore reasonably consistent with and supports our tunneling spectra results at room temperature. On the basis of our experimental and theoretical observations, we conclude that the bi-axial lattice strain can

induce direct changes in the surface electronic structure of LSM, determined here as the differences in the energy gap between the occupied and unoccupied states.

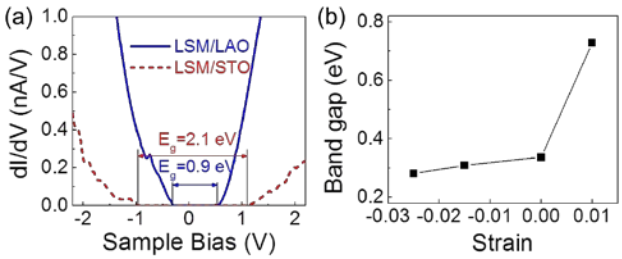

Figure 4: (a) Tunneling spectra on LSM/LAO (blue, solid line) and LSM/STO (red, dashed line), showing the energy gap, E_g, for both samples. (b) The band gap obtained from the DFT calculations of total density of states on LSM (001) as a function of strain.

The picture, however, reverses for the tunneling conductance and density of states at elevated temperatures, presented in Figure 5 at 500°C. Both of the abovementioned films exhibit no gap between the occupied and unoccupied states (Figure 5c) at 500 ^{o}C, but a significantly larger tunneling conductance and DOS (represented by dI/dV) prevails on LSM/STO surface. The transition from the presence of an energy gap to a metallic-like electronic structure may arise from the delocalization of the charge carriers at elevated temperatures, possibly accompanied by a transition from the ferromagnetic insulator to a paramagnetic metal (for x>0.3) structure,[40] or due to the formation of oxygen vacancies on the surface that create defect states in the band gap.[35,43] The thermal excitations at 500°C are not sufficient to enable the closure of 0.9-2.1 eV energy gap. Moreover, and importantly for the focus of this paper, this transition at high temperature is stronger with a larger density of states near the Fermi level for the tensile strained LSM/STO compared to the compressively strained LSM/LAO. Taking the density of states near the Fermi level (0V sample bias) as a measure of reactivity,[32] our results suggest that tensile strain state on LSM may favor electron transfer to and reactivity with oxygen at elevated temperatures in solid oxide fuel cells. We hypothesize that this difference in the electronic structure on LSM surface, directly or indirectly due to the strain state, could arise from the following two possible mechanisms. The first mechanism is associated with the formation of oxygen vacancies on the surface,[31] which modifies the *d* band structure of the neighboring transition metals and can induce states in the gap.[44,45] More facile formation of oxygen vacancies on the tensile strained LSM/STO, as shown in Figure 3b, and thus, an increase of the defect states that enhances the density of states near the Fermi level is a reasonable explanation. The second mechanism is related to the possible phase changes or restructuring on LSM[34] as a function of temperature and Sr content.[40] The precise role of surface defects and restructuring in governing the high temperature electronic structure and reactivity of strained LSM requires further experimental and theoretical investigation.

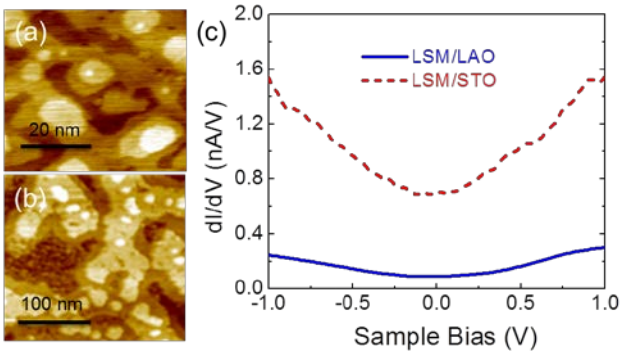

Figure 5: The surface structure on (a) LSM/LAO and (b) LSM/STO was stable at 500 °C in 10^{-3} mbar oxygen, with no evident change in morphology. (c) The tunneling spectra (dI/dV, proportional to the density of states) on LSM/LAO (blue, solid line) and LSM/STO (red, dashed line), taken at 500° C in 10^{-3} mbar of oxygen.

In summary, we demonstrated the effects of epitaxial strain on the surface cation chemistry and the surface electronic structure of LSM as a model system, both at room temperature and at elevated temperatures. A larger tendency for Sr enrichment is prevalent for the tensile strained LSM surface, owing to the relatively larger space available for the Sr cation on the surface compared to that in the bulk with increasing tensile strain. While the electronic structure exhibits the presence of an energy gap between the occupied and unoccupied states at room temperature, favoring a smaller band gap for the compressively strained LSM, the picture reverses at elevated temperatures. At 500 °C in 10^{-3} mbar of oxygen, both LSM film surfaces exhibit metallic-like behavior, and the tensile strained LSM has enhanced density of states near the Fermi level compared to the compressively strained LSM. These results illustrate the importance of lattice strain in controlling the high temperature surface chemistry and electronic structure for oxygen reduction activity on SOFC cathodes. In-depth probing and analysis of such correlations on a broad range of materials and conditions are essential towards advancing our understanding of how the surface state, including the presence of strain, relates to the oxygen reduction activity on oxide cathodes. Integration of surface sensitive *in situ* techniques and first principles-based simulations, as demonstrated here, is a necessary approach for this goal.

Experimental Methods

X-ray diffraction (XRD) measurements were performed employing a PANalytical Expert Pro MPD diffractometer to determine the phase purity and the strain states. Scanning tunneling microscopy / spectroscopy (STM/STS) at room temperature as well as at elevated temperatures was used to investigate the surface morphology and electronic structure of the strained films. The measurements were performed in a modified ultra high vacuum (UHV) system designed by Omicron Nanotechnology, Inc., with a variable temperature scanning tunneling microscope. Chemical state of

the surfaces were probed using angle resolved X-ray photoelectron spectroscopy (XPS) using a five-channel hemispherical electron analyzer, equipped in the same chamber with the STM. Casa XPS software was used to assess the spectra and calculate the relative intensity of each constituent by employing the Shirley background. Total intensity of each constituent was normalized by their corresponding cross section values from Scofield's table. Carbon contamination was removed from the surfaces of the air-exposed LSM films by heating them in oxygen pressure of 5×10^{-5} mbar at 500 ^{o}C for at least 30 min in the UHV chamber. All the STM, STS, and XPS results reported here were obtained after the cleaning process. Pyrolytic Boron Nitride (PBN) heater was used to evenly heat the LSM films during the cleaning process as well as during the STM experiments at high temperatures. STM measurements were performed in the constant-current mode using Pt/Ir tips, with a bias voltage of 1-2 V applied to the tip and a tunneling current of 200-500 pA.

Computational Method

Plane wave DFT calculations were performed using the Vienna *ab initio* simulation package (VASP)[46] to assess the surface Sr segregation energetics, from -3.5% (compressive) to +2% (tensile) on LSM. We employed the generalized gradient approximation (GGA) parameterized by Perdew and Wang[47] along with the projector augmented wave (PAW) method[48] to describe the ionic cores. To avoid the self-interaction errors that occur in the traditional DFT for strongly correlated electronic systems, we employed the DFT+*U* method, with a correction parameter of U-J = 4 eV.[49] All calculations used a plane wave expansion cutoff of 400 eV and included spin polarization. The DFT-optimized cubic lattice constant of LSM was 3.93 Å, in good agreement with the experimental value of 3.88 Å. This bulk structure of $LaMnO_3$ was cleaved along the (001) plane, with the (La,Sr)O-terminated surface, to construct a surface consistent with our PLD-grown epitaxial films. 2D-planar lattice strain was imposed by elongating the simulation cell in the *x* and *y* directions and relaxing the cell configuration and dimension in the *z* direction. The slab model is 15.5 Å thick and contains 9 atomic symmetric layers with the middle 3 layers constrained in their bulk positions. The symmetric slab was chosen to avoid the fictitious dipole moment. We have chosen a (2×2) surface unit cell and a 4×4×1 Monkhorst-Pack *k*-point mesh, which gives a convergence of ~0.5 meV/atom. For the DOS calculations, the *k*-point mesh is increased to 8×8×1 centered at Γ using the tetrahedron method with Blöchl corrections.[50]

Acknowledgement

We thank Paul Salvador for providing the samples for this investigation, the US–DOE, Office of Fossil Energy, Grant No. DE–NT0004117, and Basic Energy Sciences, Grant No. DE-SC0002633 for financial support, and the National Science Foundation for computational support through the TeraGrid Advanced Support Program, Grant No. TG–ASC090058.

Supporting Information Available: 1) X-ray diffraction patterns, 2) X-ray photoelectron spectra (XPS), and 3) Scanning tunneling spectra (STS) taken on $La_{0.7}Sr_{0.3}MnO_3$ films grown on $SrTiO_3$ (STO) and $LaAlO_3$ (LAO); 4) the DFT model construction and description, and 5) the calculated total density of states on LSM(001) that shows a change in the band gap value as a function of strain. This material is available free of charge via the Internet at http://pubs.acs.org.

References

(1) Adler, S. B. Factors Governing Oxygen Reduction in Solid Oxide Fuel Cell Cathodes. *Chem. Rev.* **2004,** *104*, 4791-4843.

(2) Jacobson, A. J. Materials for Solid Oxide Fuel Cells. *Chem. Mater.* **2010,** *22*, 660-674.

(3) Chroneos, A.; Parfitt, D.; Kilner, J. A.; Grimes, R. W. Anisotropic Oxygen Diffusion in Tetragonal $La_2NiO_{4+\delta}$: Molecular Dynamics Calculations. *J Mater Chem* **2010,** *20*, 266-270.

(4) Tarancón, A.; Burriel, M.; Santiso, J.; Skinner, S. J.; Kilner, J. A. Advances in Layered Oxide Cathodes for Intermediate Temperature Solid Oxide Fuel Cells. *J Mater Chem* **2010,** *20*, 3799-3813.

(5) Kushima, A.; Parfitt, D.; Chroneos, A.; Yildiz, B.; Kilner, J. A.; Grimes, R. W. Interstitialcy Diffusion of Oxygen in Tetragonal $La_2CoO_{4+\delta}$. *Phys. Chem. Chem. Phys.* **2011,** *13*, 2242-2249.

(6) Choi, Y.; Lynch, M. E.; Lin, M. C.; Liu, M. Prediction of O_2 Dissociation Kinetics on $LaMnO_3$-Based Cathode Materials for Solid Oxide Fuel Cells. *J. Phys. Chem. C* **2009,** *113*, 7290-7297.

(7) Mastrikov, Y. A.; Merkle, R.; Heifets, E.; Kotomin, E. A.; Maier, J. Pathways for Oxygen Incorporation in Mixed Conducting Perovskites: A DFT-Based Mechanistic Analysis for (La, Sr)$MnO_{3-\delta}$. *J. Phys. Chem. C* **2010,** *114*, 3017-3027.

(8) Co, A. C.; Birss, V. I. Mechanistic Analysis of the Oxygen Reduction Reaction at (La,Sr)MnO_3 Cathodes in Solid Oxide Fuel Cells. *J. Phys. Chem. B* **2006,** *110*, 11299-11309.

(9) Dulli, H.; Dowben, P. A.; Liou, S. H.; Plummer, E. W. Surface Segregation and Restructuring of Colossal-Magnetoresistant Manganese Perovskites $La_{0.65}Sr_{0.35}MnO_3$. *Phys. Rev. B* **2000,** *62*, R14629-R14632.

(10) Bertacco, R.; Contour, J. P.; Barthélemy, A.; Olivier, J. Evidence for Strontium Segregation in $La_{0.7}Sr_{0.3}MnO_3$ Thin Films Grown by Pulse Laser Deposition: Consequences for Tunnelling Junctions. *Surf. Sci.* **2002,** *511*, 366-372.

(11) Wu, Q.-H.; Liu, M.; Jaegermann, W. X-ray Photoelectron Spectroscopy of $La_{0.5}Sr_{0.5}MnO_3$. *Mater. Lett.* **2005,** *59*, 1980-1983.

(12) Fister, T. T.; Fong, D. D.; Eastman, J. A.; Baldo, P. M.; Highland, M. J.; Fuoss, P. H.; Balasubramaniam, K. R.; Meador, J. C.; Salvador, P. A. In Situ Characterization of Strontium Surface Segregation in Epitaxial $La_{0.7}Sr_{0.3}MnO_3$ Thin Films as a Function of Oxygen Partial Pressure. *Appl. Phys. Lett.* **2008,** *93*, 151904/1-151904/3.

(13) Katsiev, K.; Yildiz, B.; Balasubramaniam, K.; Salvador, P. A. Electron Tunneling Characteristics on $La_{0.7}Sr_{0.3}MnO_3$ Thin-Film Surfaces at High Temperature. *Appl. Phys. Lett.* **2009,** *95*, 092106/1-092106/3.

(14) Daoudi, K.; Tsuchiya, T.; Yamaguchi, I.; Manabe, T.; Mizuta, S.; Kumagai, T. Microstructural and Electrical Properties of $La_{0.7}Ca_{0.3}MnO_3$ Thin Films Grown on $SrTiO_3$ and $LaAlO_3$ Substrates Using Metal-Organic Deposition. *J. Appl. Phys.* **2005,** *98*, 013507/1-013507/6.

(15) Gebhardt, U.; Kasper, N. V.; Vigliante, A.; Wochner, P.; Dosch, H.; Razavi, F. S.; Habermeier, H. U. Formation and Thickness Evolution of Periodic Twin Domains in Manganite Films Grown on $SrTiO_3$(001) Substrates. *Phys. Rev. Lett.* **2007,** *98*, 096101/1-096101/4.

(16) Razavi, F. S.; Rao, G. V. S.; Jalili, H.; Habermeier, H. U. Pressure Induced Phase Transition in Periodic Microtwinned Thin Film of $La_{0.88}Sr_{0.1}MnO_3$. *Appl. Phys. Lett.* **2006,** *88*, 174103/1-174103/3.

(17) Ding, Y.; Haskel, D.; Tseng, Y.-C.; Kaneshita, E.; van Veenendaal, M.; Mitchell, J. F.; Sinogeikin, S. V.; Prakapenka, V.; Mao, H.-K. Pressure-Induced Magnetic Transition in Manganite ($La_{0.75}Ca_{0.25}MnO_3$). *Phys. Rev. Lett.* **2009,** *102*, 237201/1-237201/4.

(18) Rata, A. D.; Herklotz, A.; Nenkov, K.; Schultz, L.; Dörr, K. Strain-Induced Insulator State and Giant Gauge Factor of $La_{0.7}Sr_{0.3}CoO_3$ Films. *Phys. Rev. Lett.* **2008,** *100*, 076401/1-076401/4.

(19) Mavrikakis, M.; Hammer, B.; Nørskov, J. K. Effect of Strain on the Reactivity of Metal Surfaces. *Phys. Rev. Lett.* **1998,** *81*, 2819-2822.

(20) Strasser, P.; Koh, S.; Anniyev, T.; Greeley, J.; More, K.; Yu, C.; Liu, Z.; Kaya, S.; Nordlund, D.; Ogasawara, H.*et al.* Lattice-Strain Control of the Activity in Dealloyed Core–Shell Fuel Cell Catalysts. *Nat. Chem.* **2010,** *2*, 454-460.

(21) Kushima, A.; Yip, S.; Yildiz, B. Competing Strain Effects in Reactivity of $LaCoO_3$ with Oxygen. *Phys. Rev. B* **2010,** *82*, 115435/1-115435/6.

(22) Sase, M.; Yashiro, K.; Sato, K.; Mizusaki, J.; Kawada, T.; Sakai, N.; Yamaji, K.; Horita, T.; Yokokawa, H. Enhancement of Oxygen Exchange at the Hetero Interface of $(La,Sr)CoO_3/(La,Sr)_2CoO_4$ in Composite Ceramics. *Solid State Ionics* **2008,** *178*, 1843-1852.

(23) Garcia-Barriocanal, J.; Rivera-Calzada, A.; Varela, M.; Sefrioui, Z.; Iborra, E.; Leon, C.; Pennycook, S. J.; Santamaria, J. Colossal Ionic Conductivity at Interfaces of Epitaxial ZrO_2:$Y_2O_3/SrTiO_3$ Heterostructures. *Science* **2008,** *321*, 676-680.

(24) Kushima, A.; Yildiz, B. Oxygen Ion Diffusivity in Strained Yttria Stabilized Zirconia: Where is the Fastest Strain? *J Mater Chem* **2010,** *20*, 4809-4819.

(25) Schichtel, N.; Korte, C.; Hesse, D.; Janek, J. Elastic Strain at Interfaces and its Influence on Ionic Conductivity in Nanoscaled Solid Electrolyte Thin Films-Theoretical Considerations and Experimental Studies. *Phys. Chem. Chem. Phys.* **2009,** *11*, 3043-3048.

(26) Balasubramaniam, K. R.; Havelia, S.; Salvador, P. A.; Zheng, H.; Mitchell, J. F. Epitaxial Stabilization and Structural Properties of $REMnO_3$ (RE = Dy,Gd,Sm) Compounds in a Layered, Hexagonal ABO_3 Structure. *Appl. Phys. Lett.* **2007,** *91*, 232901/1-232901/3.

(27) Han, J. W.; Kitchin, J. R.; Sholl, D. S. Step Decoration of Chiral Metal Surfaces. *J. Chem. Phys.* **2009,** *130*, 124710/1-124710/8.

(28) Lu, H. M.; Jiang, Q. Surface Tension and Its Temperature Coefficient for Liquid Metals. *J. Phys. Chem. B* **2005,** *109*, 15463-15468.

(29) Sayle, T. X. T.; Parker, S. C.; Catlow, C. R. A. Surface Segregation of Metal Ions in Cerium Dioxide. *J. Phys. Chem.* **1994,** *98*, 13625-13630.

(30) Caillol, N.; Pijolat, M.; Siebert, E. Investigation of Chemisorbed Oxygen, Surface Segregation and Effect of Post-Treatments on $La_{0.8}Sr_{0.2}MnO_3$ Powder and Screen-Printed Layers for Solid Oxide Fuel Cell Cathodes. *Appl. Surf. Sci.* **2007,** *253*, 4641-4648.

(31) Lee, Y.-L.; Morgan, D. Prediction of Surface Oxygen Vacancy Concentrations of $(La_{1-x}Sr_x)MnO_3$. *ECS Trans.* **2009,** *25*, 2769-2774.

(32) Groß, A. *Theoretical Surface Science: A Microscopic Perspective*, 2nd ed.; Springer-Verlag: Berlin, 2009.

(33) Bibes, M.; Balcells, L.; Valencia, S.; Fontcuberta, J.; Wojcik, M.; Jedryka, E.; Nadolski, S. Nanoscale Multiphase Separation at $La_{2/3}Ca_{1/3}MnO_3/SrTiO_3$ Interfaces. *Phys. Rev. Lett.* **2001,** *87*, 067210/1-067210/4.

(34) Fuchigami, K.; Gai, Z.; Ward, T. Z.; Yin, L. F.; Snijders, P. C.; Plummer, E. W.; Shen, J. Tunable Metallicity of the $La_{5/8}Ca_{3/8}MnO_3$(001) Surface by an Oxygen Overlayer. *Phys. Rev. Lett.* **2009,** *102*, 066104/1-066104/4.

(35) Szot, K.; Speier, W.; Carius, R.; Zastrow, U.; Beyer, W. Localized Metallic Conductivity and Self-Healing during Thermal Reduction of $SrTiO_3$. *Phys. Rev. Lett.* **2002,** *88*, 075508/1-075508/4.

(36) Okawa, N.; Tanaka, H.; Akiyama, R.; Matsumoto, T.; Kawai, T. Effects of Film Thickness on Surface Flatness and Physical Properties in $La_{1-x}Sr_xMnO_3$ Thin Films Investigated by Scanning Tunneling Microscopy. *Solid State Comm.* **2000,** *114*, 601-605.

(37) Khabibulakh, K.; Yildiz, B.; Kavaipatti, B.; Salvador, P. Correlations of Electronic and Chemical State on $La_{0.7}Sr_{0.3}MnO_3$ Dense Thin-Film Cathode Surfaces. *ECS Trans.* **2009,** *25*, 2309-2318.

(38) Pruneda, J. M.; Ferrari, V.; Rurali, R.; Littlewood, P. B.; Spaldin, N. A.; Artacho, E. Ferrodistortive Instability at the (001) Surface of Half-Metallic Manganites. *Phys. Rev. Lett.* **2007,** *99*, 226101/1-226101/4.

(39) Ma, C.; Yang, Z. Q.; Picozzi, S. Ab Initio Electronic and Magnetic Structure in $La_{0.66}Sr_{0.33}MnO_3$: Strain and Correlation Effects. *J. Phys. Condens. Matter.* **2006,** *18*, 7717-7728.

(40) Urushibara, A.; Moritomo, Y.; Arima, T.; Asamitsu, A.; Kido, G.; Tokura, Y. Insulator-Metal Transition and Giant Magnetoresistance in $La_{1-x}Sr_xMnO_3$. *Phys. Rev. B* **1995,** *51*, 14103-14109.

(41) Pandey, S. K.; Kumar, A.; Patil, S.; Medicherla, V. R. R.; Singh, R. S.; Maiti, K.; Prabhakaran, D.; Boothroyd, A. T.; Pimpale, A. V. Investigation of the Spin State of Co in $LaCoO_3$ at Room Temperature: Ab Initio Calculations and High-Resolution Photoemission Spectroscopy of Single Crystals. *Phys. Rev. B* **2008,** *77*, 045123/1-045123/7.

(42) Sholl, D. S.; Steckel, J. A. *Density Functional Theory : A Practical Introduction*; John Wiley & Sons, Inc.: Hoboken, NJ, 2009.

(43) Diebold, U.; Li, S.-C.; Schmid, M. Oxide Surface Science. *Annu. Rev. Phys. Chem.* **2010,** *61*, 129-148.

(44) Ganduglia-Pirovano, M. V.; Hofmann, A.; Sauer, J. Oxygen Vacancies in Transition Metal and Rare Earth Oxides: Current State of Understanding and Remaining Challenges. *Surf. Sci. Rep.* **2007,** *62*, 219-270.

(45) Kim, Y. S.; Kim, J.; Moon, S. J.; Choi, W. S.; Chang, Y. J.; Yoon, J. G.; Yu, J.; Chung, J. S.; Noh, T. W. Localized Electronic States Induced by Defects and Possible Origin of Ferroelectricity in Strontium Titanate Thin Films. *Appl. Phys. Lett.* **2009,** *94*, 202906/1-202906/3.

(46) Kresse, G.; Furthmuller, J. Efficient Iterative Schemes for Ab Initio Total-Energy Calculations Using a Plane-Wave Basis Set. *Phys. Rev. B* **1996,** *54*, 11169-11186.

(47) Perdew, J. P.; Chevary, J. A.; Vosko, S. H.; Jackson, K. A.; Pederson, M. R.; Singh, D. J.; Fiolhais, C. Atoms, Molecules, Solids, and Surfaces: Applications of the Generalized Gradient Approximation for Exchange and Correlation. *Phys. Rev. B* **1992,** *46*, 6671-6687.

(48) Blöchl, P. E. Projector Augmented-Wave Method. *Phys. Rev. B* **1994,** *50*, 17953-17979.

(49) Wang, L.; Maxisch, T.; Ceder, G. Oxidation Energies of Transition Metal Oxides within the GGA+U Framework. *Phys. Rev. B* **2006,** *73*, 195107/1-195107/6.

(50) Blöchl, P. E.; Jepsen, O.; Andersen, O. K. Improved Tetrahedron Method for Brillouin-Zone Integrations. *Phys. Rev. B* **1994,** *49*, 16223-16233.

Cation size mismatch and charge interactions drive dopant segregation at the surfaces of manganite perovskites

Wonyoung Lee*, Jeong Woo Han*, Yan Chen, Zhuhua Cai and Bilge Yildiz§

Laboratory for Electrochemical Interfaces, Department of Nuclear Science and Engineering, Massachusetts Institute of Technology, 77 Massachusetts Avenue, Cambridge, Massachusetts 02139, United States

* These two authors contributed equally to this work.

§ Corresponding author: byildiz@mit.edu

Abstract

Cation segregation on perovskite oxide surfaces affects vastly the oxygen reduction activity and stability of solid oxide fuel cell (SOFC) cathodes. A unified theory that explains the physical origins of this phenomenon is therefore needed for designing cathode materials with optimal surface chemistry. We quantitatively assessed the *elastic* and *electrostatic* interactions of the dopant with the surrounding lattice as the key driving forces for segregation on model perovskite compounds, LnMnO$_3$ (host cation Ln=La, Sm). Our approach combines surface chemical analysis with X-ray photoelectron and Auger electron spectroscopy on model dense thin films, and computational analysis with density functional theory (DFT) calculations and analytical models. Elastic energy differences were systematically induced in the system by varying the radius of the selected dopants (Ca, Sr, Ba) with respect to the host cations (La, Sm) while retaining the same charge state. Electrostatic energy differences were introduced by varying the distribution of charged oxygen and cation vacancies in our models. Varying the oxygen chemical potential in our experiments induced changes in both the elastic energy and electrostatic interactions. Our results quantitatively demonstrate that the mechanism of dopant segregation on perovskite oxides includes *both* the elastic and electrostatic energy contributions.

A smaller size mismatch between the host and dopant cations and a chemically expanded lattice were found to reduce the segregation level of the dopant and to enable more stable cathode surfaces. Ca-doped $LaMnO_3$ was found to have the most stable surface composition with the least cation segregation among the compositions surveyed. The diffusion kinetics of the larger dopants, Ba and Sr, was found to be slower, and can kinetically trap the segregation at reduced temperatures despite the larger elastic energy driving force. Lastly, scanning probe image-contrast showed that the surface chemical heterogeneities made of dopant oxides upon segregation were electronically insulating. The consistency between the results obtained from experiments, DFT calculations and analytical theory in this work provides a predictive capability to tailor the cathode surface compositions for high-performance SOFCs.

1. Introduction

Cation segregation at the surface and the interfaces of transition metal oxides impacts the reactions that are often critical to the overall device performance in a range of device applications, including solid oxide fuel cells[1-9], oxygen permeation membranes[10,11], batteries[12-15], magnetic[16-19], catalytic[20,21] and ferroelectric[22,23] materials. In particular, cation segregation on perovskite oxide surfaces impacts tremendously the reactivity and stability of solid oxide fuel cell (SOFC) cathodes.[1,3,4,6-8,24,25] The slow rate of oxygen reduction reaction (ORR), which is generally agreed to be limited by the surface exchange reactions on mixed ionic electronic conducting cathodes,[26,27] imposes the main barrier for implementation of high-performance SOFCs at intermediate temperatures (500-700 °C).[28,29] To attain highly reactive and stable cathode surfaces for fast ORR kinetics, it is important to tailor the catalytic activity of transition metal oxide cathode with a thorough knowledge of the surface composition and structure at the atomic level. The surface of the SOFC cathodes, typically made from perovskite-related oxides, is not static, and the structure and chemistry are driven dynamically by the surrounding environments at elevated temperatures, in oxygen partial pressure, and under electrochemical potentials. The complexity of these surfaces and the harsh environments that they function in have prohibited thus far the development of clear fundamental principles that relate their surface

state to the ORR kinetics. This is important not only for the reactivity but also for the durability of the electrodes.

Cation segregation at the surface of perovskite oxides has been a commonly observed phenomenon that has direct relations to cathode reactivity and stability in ORR.[5,30-33] An example is the Sr enrichment at the surface of $La_{1-x}Sr_xMnO_3$ (LSM) and $La_{1-x}Sr_xCoO_3$ (LSC) that are widely studied cathodes. Upon dopant segregation, the surface can exist in different chemical phases, including the perovskite-termination structure with the Sr replacing La on the A-site at the surface[30,31], and phase separation in the form of Ruddlesden-Popper (RP) phases[32] or dopant-oxides (e.g., SrO).[1,5,34] At the surface of LSM, the concentration of Sr dopant was shown to increase with decreasing oxygen pressure[31] and increasing temperature (> 500 ºC).[33] On another well-studied perovskite, $SrTiO_3$ (STO), the surface was drastically altered by formation of Sr-rich RP phases in oxidizing conditions and Ti-rich phases in reducing conditions.[35] Furthermore, such surface segregates of secondary phases can form a spatially heterogeneous surface chemistry and structure, as found on LSC[1] in our previous work and on STO[36]. Each surface structure formed upon cation segregation is associated with different ORR reactivity. A unified theory that explains the physical origins of dopant segregation on perovskite-related oxides is therefore needed for designing cathode materials with optimal surface chemistry for fast and stable ORR kinetics.

Thermodynamic and kinetic conditions that drive surface segregation and transitions between possible surface phases/structures on perovskite oxides have not been well explored and explained. The different surface free energies (surface bond breaking) and the different atomic sizes (lattice strain) of the elements cause surface segregation to reduce the free energy of the system.[19,37-41] Especially, on metal oxides of ionic nature, the existence of a space-charge layer near the surface also provides a strong chemical potential to drive segregation.[42-46] Therefore, it is reasonable to say that the key driving forces to segregation originates from the *elastic* and *electrostatic* interactions of the dopant with the surrounding lattice in a perovskite oxide. The specific mechanisms that manifest these interactions are related to: 1) the size mismatch between the dopant and host cations and the associated elastic energy minimization by pushing the larger or smaller dopant to free surfaces or interfaces[18,19,38,47]; and 2) the charged defect

interactions, such as a strong association of dopant cations with oxygen vacancies, which can drive the dopants to positively charged interfaces where oxygen vacancies are in abundance,[44] as well as with polar surfaces. We provide this description of the contributors to dopant segregation in analogy to the vacancy-dopant association energy in bulk oxides. Vacancy-dopant association generally contains two terms: the elastic interactions arising from the size mismatch of dopants with host cations and the Coulombic term which reflects the electrostatic attraction between the constituents.[48]

Recently, Harrison has hypothesized that the surface charging on the (La,Sr)MnO_3 is the origin of the segregation of Sr at the surface of LSM.[49] On the (100) surface of $La_xSr_{1-x}MnO_3$, AO planes with a uniform distribution of Sr and La cations take a charge of $+e(1-x)$ per A-site. Terminating such a set of charged planes leaves an effective surface charge of $\pm e(1-x)/2$ per A-site. Harrison's work constructed an electrostatic model of the interaction of Sr with the charged surfaces on LSM. With this model, it was shown that the large energy associated with a charged surface could be minimized by depleting the La and increasing the Sr concentration at and near the surface of LSM. This result would seem to give compelling evidence that the surface charging is a source of the segregation of the dopant at the surface of LSM. On the other hand, only this electrostatic contribution alone cannot provide an accurate quantitative prediction of the large extents of segregation on such materials as acknowledged in the same work,[49] and as also shown in our results later in this paper. Past work on titanates have suggested the importance of both the elastic and electrostatic interactions in determining cation segregation on the surface.[50] However, the analysis remained at a phenomenological level, and the electrostatic interaction was considered to be based on only the effects of surface adsorbates. An alternative model that can be discussed is the kinetic demixing phenomenon when the material is subjected to an oxygen chemical potential gradient across.[51] However, significant cation segregation is found on many perovskite surfaces even without the presence of a gradient of oxygen chemical potential, therefore, we believe this model cannot explain the intrinsic drivers to cation segregation.

In this paper, we quantitatively assessed the electrostatic and elastic energy minimization as two main driving forces of dopant segregation at the surface of manganite-based perovskite oxides,

LnMnO_3. The host cation *Ln*=La was used in our experiments and *Ln*=La and Sm were used in our computational work as the model material systems. We probed the surface chemistry and structure with X-ray photoelectron (XPS) and Auger electron spectroscopy (AES) on model dense thin films. The effects of the elastic energy on the cation segregation were investigated by varying the size mismatch between the dopant (Ca, Sr, Ba) and host cation in the perovskite thin films. The effects of the electrostatic energy on the cation rearrangements were investigated with control of the oxygen chemical potential during the annealing of thin films and with control of the distribution of charged defects in our models. Density functional theory (DFT) calculations and analytical models were used to elucidate the underlying physics of cation segregation, including the kinetic effects, and to quantitatively decouple the contribution of the elastic and electrostatic energy to segregation. We show, using image-contrast between atomic force microscopy (AFM) and scanning tunneling microscopy (STM), that the surface chemical heterogeneities upon dopant segregation were electronically insulating, and thus, they are expected to hinder the ORR kinetics. Our results demonstrate that the mechanism of dopant segregation on perovskite oxides includes important contributions from both the elastic and the electrostatic energy – a smaller size mismatch between the dopant and host cations, a chemically expanded lattice, and reduction of the surface positive charge can reduce the segregation level of the A-site dopant and enable more stable cathode surfaces.

2. Approach

We hypothesized that the elastic and electrostatic interactions are the key driving forces of cation segregation on perovskite oxide surfaces. To quantitatively assess these two contributions, we experimentally determined the chemical composition and structures of dopant-enriched surfaces of the $LaMnO_3$ films upon annealing at elevated temperatures in varying oxygen pressures. We interpreted our experimental results quantitatively and predictively using DFT-calculations and analytical models. The parameters that affect the magnitude of the two driving forces were varied in our experiments and computational models; in particular, the dopant size, the lattice parameter, and the distribution of charged vacancies.

We note that our DFT calculations focused on the dopant segregation within the perovskite-terminated surface lattice by simply replacing the host cation with the dopant, while our experiments showed ultimately heterogeneous phase separation at the surface. Enrichment of the dopant on the A-site sub-lattice at the surface would lead to a larger concentration of the dopant at the surface compared to the bulk nominal level. If the concentration of the segregated dopants increases beyond the solubility limit at the perovskite surface at elevated temperatures, phase-separated particles such as $SrO/Sr(OH)_2$ or layered RP phases can form.[1,32] The calculated total segregation energy on the perovskite lattice is a quantitative measure of the increase in the concentration of dopant cations on the perovskite surface. This quantity at the same time indicates the extent of the new phase formation because the secondary phases will form only following the increase in dopant cation concentration beyond the solubility limit at the surface. Therefore, our computational approach here is applicable in assessing the "tendency" to restructure or phase-separate because of dopant segregation at the surface, even if the possible secondary phases are not explicitly captured in our models. The following sub-sections describe the method details in our approach.

2.1. Experimental methods

2.1.1. Thin film fabrication

In the experimental part of our investigation, epitaxial dense thin films of $La_{0.8}D_{0.2}MnO_3$ (D=Ca, Sr, Ba) with the same crystallographic orientation were used as model system. The use of such thin film model systems enabled us to eliminate the effects of a complex microstructure on the segregation process, and to focus on the key parameters that we controlled for varying the extent of elastic and electrostatic energy as the drivers to segregation. Three sets of dense thin films were fabricated with the three different dopants, $La_{0.8}Ca_{0.2}MnO_3$ (LCM), $La_{0.8}Sr_{0.2}MnO_3$ (LSM), and $La_{0.8}Ba_{0.2}MnO_3$ (LBM). We chose Ca, Sr, and Ba as the dopants because they have the same formal charge of +2, but different ionic radii, as shown in the Table 1. By varying only the size of the dopant cations but not their charge, we systematically induced the elastic energy differences in the system while maintaining the same electrostatic interactions of the dopant. The largest size mismatch between the dopant and host cations on the A-site was in the LBM film, followed by LSM and LCM. In our computational work, we further extended

the results to doped $SmMnO_3$, where a larger mismatch between the host and these dopants prevailed compared to the $LaMnO_3$ system.

Table 1. Size mismatch, denoted as $(R_{dopant}-R_{host})/R_{host}$ (%), between the dopant and host cations in $LaMnO_3$ and $SmMnO_3$. Shannon's ionic radii[52] are used as the cation radii, R.

Host cation	Dopant cation		
	Ca^{2+}	Sr^{2+}	Ba^{2+}
La^{3+}	-1.5	+5.9	+18.4
Sm^{3+}	+8.1	+16.1	+29.8

Constituent powders were prepared by a modified Pechini or polymer precursor synthesis method.[53] High purity $La(NO_3)_3{\cdot}6H_2O$ (99.9 % purity), $Ca(NO_3)_2{\cdot}4H_2O$ (99.98 % purity), $Sr(NO_3)_2$ (99.97 % purity), $Ba(NO_3)_2$ (99.999 % purity), and $Mn(NO_3)_2{\cdot}4H_2O$ (99.98 % purity) (all precursors from Alfa Aesar) were dissolved at the stoichiometric ratio in distilled water with citric acid. Ethylene glycol was then added and the solution was heated till self-combustion occurred. The as-synthesized powders were subsequently calcined at 1100 °C for 6 hrs in air with ramping rate of 3 °C/min. The powders were ground in an agate mortar and pestle, and were uniaxially pressed to produce 1 inch diameter target. The target was sintered at 1300 °C in air for 20 hrs with ramping rate of 3 °C/min. All films with a thickness of about 20 nm were deposited on single-crystal $SrTiO_3$ (STO) (100) substrates using pulsed laser deposition (PLD). Highly epitaxial films of (100) orientation were obtained in all three sets of compositions to avoid microstructural effects on the segregation behavior. PLD was performed with a KrF excimer laser at a wavelength of 248 nm and laser beam energy of 550 mJ/pulse at 10 Hz, at 815 ºC with an oxygen pressure of 10 mTorr and with the target-to-substrate distance of 6 cm. After deposition, the sample was cooled at 10 °C/min to room temperature in an oxygen pressure of 10 Torr.[30]

2.1.2. Thin film characterization

A Veeco/Digital Instrument Nanoscope IV was used to perform tapping mode atomic force microscopy (AFM) for characterizing the surface morphology.

A Physical Electronics Model 700 Auger electron spectroscopy (AES) was used to identify the surface cation content, with the ability to detect lateral heterogeneities in cation compositions with high spatial resolution at the nm-scale. Incident electrons of 25 keV and 10 nA were used for both SEM imaging and the Auger electron excitation. The Ba MNN, Sr LMM, La MNN, and Mn LMM Auger emissions were measured for quantifying the surface cation composition using peak-to-peak intensities of the tight-scans. The sampling depths of these AES electrons are ~4.0 nm for Ba MNN, ~8.5 nm for Sr LMM, ~4.0 nm for La MNN, and ~4.0 nm for Mn LMM.[54]

Angle-resolved X-ray photoelectron spectroscopy (AR-XPS) was used to identify the cation chemistries with near-surface depth resolution on thin films. The Omicron EA 125 hemispherical analyzer and Omicron DAR 400 Mg/Al dual anode nonmonochromated X-ray source were used with Mg Kα X-ray (1253.6 eV) operated at 300 W. CasaXPS 2.3.15 software was used for spectral analysis and compositional quantification. While most samples were examined in their as-annealed conditions, the as-deposited samples were examined after removing carbon contamination from their surfaces prior to the analysis. This was done by heating the samples in an oxygen pressure of 5×10^{-5} mbar at 500 °C for 1.5 h in the UHV chamber.[1] Spectra were acquired with emission angles from 0 ° to 80 ° as defined relative to the surface normal. For the excitation energy of 1253.6 eV, the sampling depths of these photoelectrons at normal emission are ~6.5 nm for Sr 3d, Ba 4d, and La 4d, ~5.5 nm for Ca 2p, and ~4.0 nm for Mn 2p.[54] At the emission angle of 80°, the sampling depth of each element are approximately 20 % of those at the emission angle of 0°, making the measurements significantly more surface sensitive.

Although the high surface sensitivity obtained by AR-XPS provides a unique benefit to explore the extreme surface properties, it also results in incomplete information about the actual amount of segregated dopants when there are significant chemical and structural heterogeneities at the surface upon segregation. As we present in the Results, dopant segregation after annealing resulted in the formation of particles that were clustered at the surface with 20-400 nm in width and 2-40 nm in height. Because the segregate particles were much higher than the penetration depth of the AR-XPS analysis, an apparent decrease of dopant cation content was found from

the AR-XPS quantification upon annealing, while the spatially resolved AES showed a clear and significant enrichment of dopant cations (Ba and Sr in particular) at the surface. To compensate for this geometry-related artifact and to more accurately obtain the amount (extent) of dopant enrichment upon annealing, we combined the calculated the cation composition from AR-XPS and the geometric information from AFM. The procedure is described in Supporting Information. All cation spectra acquired with two emission angles were used to calculate the relative cation intensity ratios after two sequential normalization procedures. First, cation intensity ratios obtained from two emission angles were normalized by dividing cation intensity ratio at the emission angle of 80 ° by that at the emission angle of 0 °; for example, $[Ba/Mn]_{\theta=80°}/[Ba/Mn]_{\theta=0°}$ in case of the LBM films. By dividing cation intensity ratios obtained, we minimized the possible quantification errors, which arose from the different attenuation depths of different binding energies of cations. Second, all cation intensity ratios were presented with respect to the as-deposited samples to compare the relative changes in each cation composition as a function of temperature. This ratio then provides the measure of dopant segregation at the surface as a function of annealing. This series of normalization procedures allow a direct comparison of the surface segregation among the three sets of thin films.

Scanning tunneling microscopy (STM) was employed to investigate the surface morphology and electronic structure on the thin films. The measurements were performed in a modified UHV system (VT-STM, Omicron Nanotechnology). Data were acquired in the constant-current mode using etched Pt/Ir tips, with a sample bias voltage of 1-2 V and a tunneling current of 10-50 pA. The measurements were performed after sample cleaning at 500 ºC for 1.5 hr in ~3×10^{-3} mbar of oxygen. The sample was then cooled down to room temperature slowly in the same oxygen pressure.

Ex situ X-ray diffraction (XRD) 2θ-ω scans were performed to determine the crystal structure, the phase purity, and the strain states of the thin films. The measurements employed a high resolution four-circle Bruker D8 Discover diffractometer, equipped with a Göbel mirror, four-bounce Ge(022) channel-cut monochromator, Eulerian cradle, and a scintillation counter, using Cu Kα1 radiation.

2.1.3. Annealing conditions

The samples were annealed in different oxygen pressures as a function of temperature. Samples annealed in air were subjected to a heating ramp rate of 10 °C/min and maintained at the set temperature for 1 hr in a tube furnace. After annealing at the desired temperature for 1 hr, the samples were cooled down to ~300 °C with a cooling ramp rate of 20 °C/min. The samples were then directly transferred to the UHV chamber for subsequent XPS analysis, preserving the surface states at elevated temperature and minimizing the possible surface contamination. Separate sets of samples were annealed for 1 hr at each temperature in lower oxygen pressures in the UHV chamber with the base pressure of ~1×10^{-6} mbar and ~1×10^{-9} mbar. The XPS and AES measurements were performed in ~1×10^{-9} mbar for all samples. XPS measurements on samples annealed in ~1×10^{-9} mbar were performed *in situ* at high temperature. All other measurements were performed upon cooling the samples.

2.2. Computational methods and models

Similarly to the experimental model systems, the elastic energy differences were introduced by varying the dopant size with respect to the host cation while keeping the same charge state. $LaMnO_3$ and $SmMnO_3$ were used as the host lattice, and Ca, Sr, and Ba as the dopants (see Table 1). Electrostatic energy differences were introduced by constructing seven different models with varying concentration and distribution of charged oxygen vacancies and A-site cation vacancies.

2.2.1. Density functional theory calculations

We performed plane wave DFT calculations using the Vienna *ab initio* simulation package (VASP).[55] We employed the generalized gradient approximation (GGA) parameterized by Perdew and Wang[56] along with the projector augmented wave (PAW) method[57] to describe the ionic cores. To avoid the self-interaction errors that occur in the traditional DFT for strongly correlated electronic systems, we employed the DFT+*U* method within Dudarev's approach[58] accounting for the on-site Coulomb interaction in the localized *d* orbitals, with an effective U-J = 4 eV.[30,59,60] All calculations used a plane wave expansion cutoff of 400 eV and included spin polarization. Geometries were relaxed using a conjugate gradient algorithm until the forces on

all unconstrained atoms were less than 0.03 eV/Å. The description of the surface segregation energy calculation is presented in the Supporting Information, and the same approach was reported in our recent work on LSM[30].

2.2.2. Analytical models

Our DFT calculations for segregation energy, E_{segr}, as described in Supporting Information, can only provide the total energetics upon dopant segregation in the system. To quantitatively decouple each contribution and to investigate if indeed E_{segr} can be described as the sum of elastic energy, $E_{elastic}$, and electrostatic energy, $E_{electrostatic}$, we calculated each of the two interaction energies from conventional analytical models. By this analysis, the relative importance of the elastic and electrostatic interactions to the segregation can also be evaluated.

2.2.2.1. Elastic energy

One of the main driving forces of dopant segregation in solid solutions is the relaxation of the strain energy generated around dopant cations with sizes larger or smaller than the host cation. An analytic model for the elastic energy of a misfitting solute was proposed by Friedel,[61] and used here to calculate the elastic energy of dopants in the perovskite manganite oxides.

$$E_{elastic} = -\frac{24\pi G K r_a r_b (r_a - r_b)^2}{3K r_a + 4G r_b}, \qquad (1)$$

where K is the bulk modulus of the solute, G is the shear modulus of the solvent, and r_a and r_b are the cation radii of the solute and solvent species, respectively. The equation was deduced from the continuous linear elasticity for the elastic energy released when an odd-sized atom is transferred from the bulk onto the strain-free surface of the alloy. It was originally developed for metal solid solutions,[61] but has also been used to predict an elastic strain energy contribution to the enthalpy of segregation for oxide solutions.[39-41] Eq. (1) has the advantage of simplicity to estimate the elastic energy, but it has some limitations. First, it can only be applicable to dilute solutions. Second, the lattice strain due to the size mismatch should be fully relaxed when a larger dopant segregates to the surface.

To systematically induce elastic energy differences in our computational model, we varied the radius of selected dopant cations with respect to the host cation on the A-site as shown in Table 1. In Eq. (1), we used Shannon's ionic radii[52] that describes the physical size of ions in a solid, considering the coordination number and spin state. Among the pairs of dopants and hosts we examined, Ba dopant in $SmMnO_3$ has the maximum size difference, +29.8%, while Ca dopant in $LaMnO_3$ has the minimum size difference, -1.5%. As shown in Table S1 in Supporting Information, the bulk (shear) modulus for each dopant (host) was calculated in a bulk molecular unit, $AMnO_3$ (A= La, Sm, Ca, Sr, and Ba), using DFT. For the modulus calculations, we employed the stress-strain approach[62] to directly calculate the stress tensor. Once the stress tensor components were computed, the elastic constants matrix was derived, from which we obtained the bulk and shear moduli.

2.2.2.2. Electrostatic energy

The charge interactions between the dopants, the oxygen and cation vacancies and the polar surfaces were considered as another important driving force to cation segregation on the perovskite oxides. Here first we justify how oxygen vacancies at the surface can contribute to the electrostatic attraction of the A-site dopants to the surface, based on the presence of a positively charged surface and a space charge zone. Formation energy of oxygen vacancies is typically smaller at the surface compared to the bulk of oxides, including that on the $LaMnO_3$.[63-65] For example, approximately 10^6 times higher vacancy concentration at the surface than in the bulk was predicted for $La_{0.1}Sr_{0.9}MnO_3$ under typical SOFC operating conditions of $pO_2=10^0$ atm and 1173 K. In the doped manganites, formation of oxygen vacancies (that are positively charged) upon reduction of the material is associated with electron release into the material. If electrons are localized on the transition metal (Mn in $LaMnO_3$), then they significantly contribute to electrostatic interactions. By performing Bader charge analysis upon DFT calculations, we confirmed that in our models, electrons localize at the Mn cation upon creation of an oxygen vacancy, as expected. If the created oxygen vacancies and localized electrons stay together at the surface layer, making an electroneutral surface, they would contribute no net electrostatic attraction to charged dopant defects. However, an increase of oxygen vacancies at the surface layer makes a "positively charged surface" on the mixed ionic electronic conducting (MIEC) oxides,[27] similar to those studied in our calculations. Such positively charged surface is

then accompanied by a decrease of oxygen vacancy concentration and an increase of electrons beneath the surface in the diffuse space charge layer (associated with a positive space charge potential).[27,66,67] This configuration of a "positive surface", and "the electrons (negative) being more in the space charge zone beneath the surface" would further contribute to the electrostatic attraction of the negatively charged dopant defect (Ca^{2+}, Sr^{2+}, Ba^{2+} on the La^{3+}-site) to the surface and its repulsion from beneath the surface. Consequently, under all conditions where the surface is positively charged and accompanied by electrons localized in the space charge layer beneath the surface, the MIEC surface would electrostatically attract the negatively charged dopant defects. The spatial extent and strength of the space charge zone depends on the material, for example more extensive on $SrTiO_3$ compared to that on heavily doped manganites whose Debye screening length (~1 nm)[68] is shorter than that of $SrTiO_3$.

All dopants used here, Ca, Sr, and Ba have a formal charge of +2, while the hosts have +3 charge. The oxygen vacancies have a formal charge of +2 and the A-site (*Ln*) cation vacancies have -3 charge state.[49,69] Assuming that $LnMnO_3$ is purely ionic, we calculated electrostatic energy by Coulomb's law as below;

$$E_{electrostatic} = \sum -\frac{Q_1 Q_2}{4\pi\varepsilon R_{12}}, \qquad (2)$$

where Q_1 and Q_2 are two charges separated by a distant R_{12} in a medium of dielectric constant ε. We took $\varepsilon = 56.17\,\varepsilon_0$ caculated by Islam *et al.*[70,71] as a static dielectric constant of $LnMnO_3$, where ε_0 is the vacuum permittivity. From this equation, it is expected that a surface oxygen vacancy of formal charge +2 attracts the dopant that substituted the host (this complex has a formal charge of -1), driving the dopant to toward the surface on the host sub-lattice. We considered the sum of the charge interactions between a dopant and all the ions (La, dopant, Mn, and O) within the separation distance between the two charged defects we modeled in Figure 2, not just the interaction between the two point charge defects at the surface and in the bulk. This approach then resembles the Generalized Born (GB) method,[72] taking into account at least partially the screening imposed by other atoms than the two point charges. A more accurate GB

method could be used here to improve the precision of the calculated electrostatic energy contribution to the total segregation energy.

The DFT models used in our simulations are limited in size (an inherent limitation of DFT beyond our work), and thus, we cannot capture explicitly the space charge zone described above. Instead, we impart the electrostatic energy differences by varying the distribution of oxygen and A-site cation vacancies in the DFT model (Figure 1). In this way, we also generalize the role of electrostatic interactions in cation segregation regardless of the strength of space charge in a given composition. Seven models were constructed with different configurations of oxygen and cation vacancies through the thin film models. While at the low oxygen pressure, the concentration of oxygen vacancies dominates, in the high oxygen pressure range A-site cation vacancies are expected to be dominant over the oxygen vacancies in these compounds.[73,74] Furthermore, A-site deficient perovskites were often intentionally synthesized to attain better interface stability and performance.[75-77] In Figure 1, the models are listed in the order of increasing attractive interaction to the dopant at the surface. For example, in model 1, a surface cation vacancy (of charge 3-) repels the dopant on the A-site (of charge 1-) from the surface. In addition, an oxygen vacancy (of charge 2+) near the dopant in the bulk attracts the dopant. As a result, the dopant prefers to remain in the bulk. On the other hand, in model 7, a surface oxygen vacancy attracts the dopant. Simultaneously, a cation vacancy near the dopant in the bulk prefers the host cation relative to the dopant cation. Therefore, segregation of the dopant to the surface is very favorable due to the combination of the attractive interaction toward the surface and the repulsive interaction from the bulk. Although we cannot consider every possible configuration of defect distributions here, these models can describe a trend in the interaction between the dopant and charged vacancies in the context of segregation; model (2) a cation vacancy at the surface, (3) an oxygen vacancy in the bulk, (5) an oxygen vacancy at the surface, (6) a cation vacancy in the bulk, (1) the combination of (2) and (3), and (7) the combination of (5) and (6). There is a dopant in the bulk without any vacancies in model 4, which is assumed to represent the segregation purely due to elastic strain energy and surface polarity.

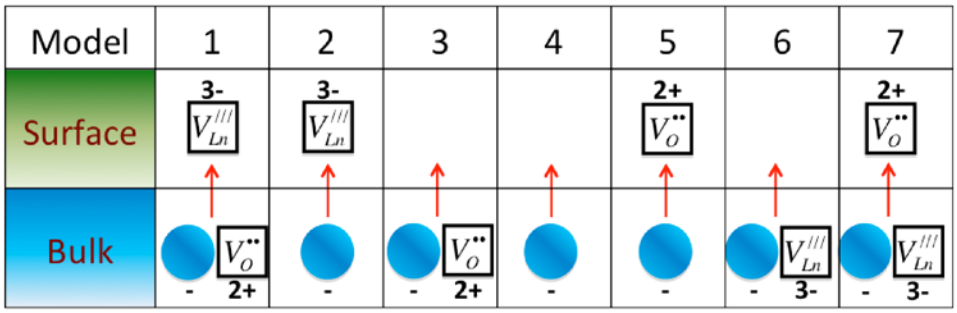

Figure 1. Seven models to represent different electrostatic interactions that are induced by controlling the distribution of charged oxygen and cation vacancies in DFT and analytical models. The blue sphere represents the dopant. Cation vacancy, V_{Ln}''', has a formal charge of -3, and the defect complex of dopant in V_{Ln}''' has -1 charge, while $V_O^{\cdot\cdot}$ has +2 charge state. The numbering from 1 to 7 is in the order of increasing attractive electrostatic force to the dopant at the surface.

3. Results and discussion

We first present our experimental results which show that: 1) the smaller dopant (Ca) segregates less and maintains a more uniform surface structure compared to the larger cations Sr and Ba (elastic effect), and 2) the low oxygen pressure reduces the extent of dopant segregation due either to the chemical expansion of the lattice (elastic effect) and/or a reduction of the space charge (electrostatic effect) in the doped $LaMnO_3$ films. Next, we computationally assess the dopant segregation quantitatively, explain the governing mechanisms in our experimental findings on $LaMnO_3$ surface, and extend predictively to other materials, in particular the $SmMnO_3$.

3.1. Experimental Results

3.1.1. Heterogeneous surface structure upon dopant segregation correlates with dopant size

First we report the surface structure upon annealing in air (high oxygen pressure) as a function of temperature. Doped $LaMnO_3$ film surfaces showed substantial structural changes upon thermal annealing at elevated temperatures in air, with a clear dependency on the size mismatch between the dopant and host cations. Figure 2(a) shows the surface morphology of doped $LaMnO_3$ films as a function of annealing temperature (shown at selected temperatures) obtained by tapping mode AFM. As-deposited film surfaces were very uniform and smooth with an RMS roughness of less than 1 nm. Annealing at high temperatures, however, induced structural changes in the form of surface particles on the film, and the extent of these structural changes followed the order of the size mismatch between the dopant and host cations. Later we will show that these particles are made of dopant-oxides. For LBM films, the surface particles appeared by 430 ºC, and they grew larger and higher upon annealing at higher temperatures. For LSM films, they appeared by 630 ºC, and grew larger with annealing temperature similarly to LBM films. For LCM films, in contrast, no structural change was found up to 830 ºC within the AFM resolution. The temperature at which the particle formation was observed and the dimension of these surface particles suggest that the LBM films are most active to form such surface phases, followed by LSM and LCM films. Furthermore, the actual amount (volume) of rearranged cations in the form of surface particles also followed the order of the size mismatch. Figure 2(b) shows the volume of the surface particles per projected unit area (calculated from the AFM images taking into account both the areal size and height profiles) as a function of annealing temperature. The volume of surface particles was the largest on LBM films, followed by LSM, and none for LCM. We note that the size mismatch between the dopant and host cations on the A-site follows the same order, the largest for Ba and the smallest for Ca. This correlation suggests that the elastic energy difference in the system due to the dopant-host cation size mismatch plays an important role in cation rearrangements at the surface; the larger size mismatch drives cation segregation more actively toward the surface to minimize the elastic energy in the system, and ultimately form the surface phases. All the chemical analysis presented in the following sections support this argument.

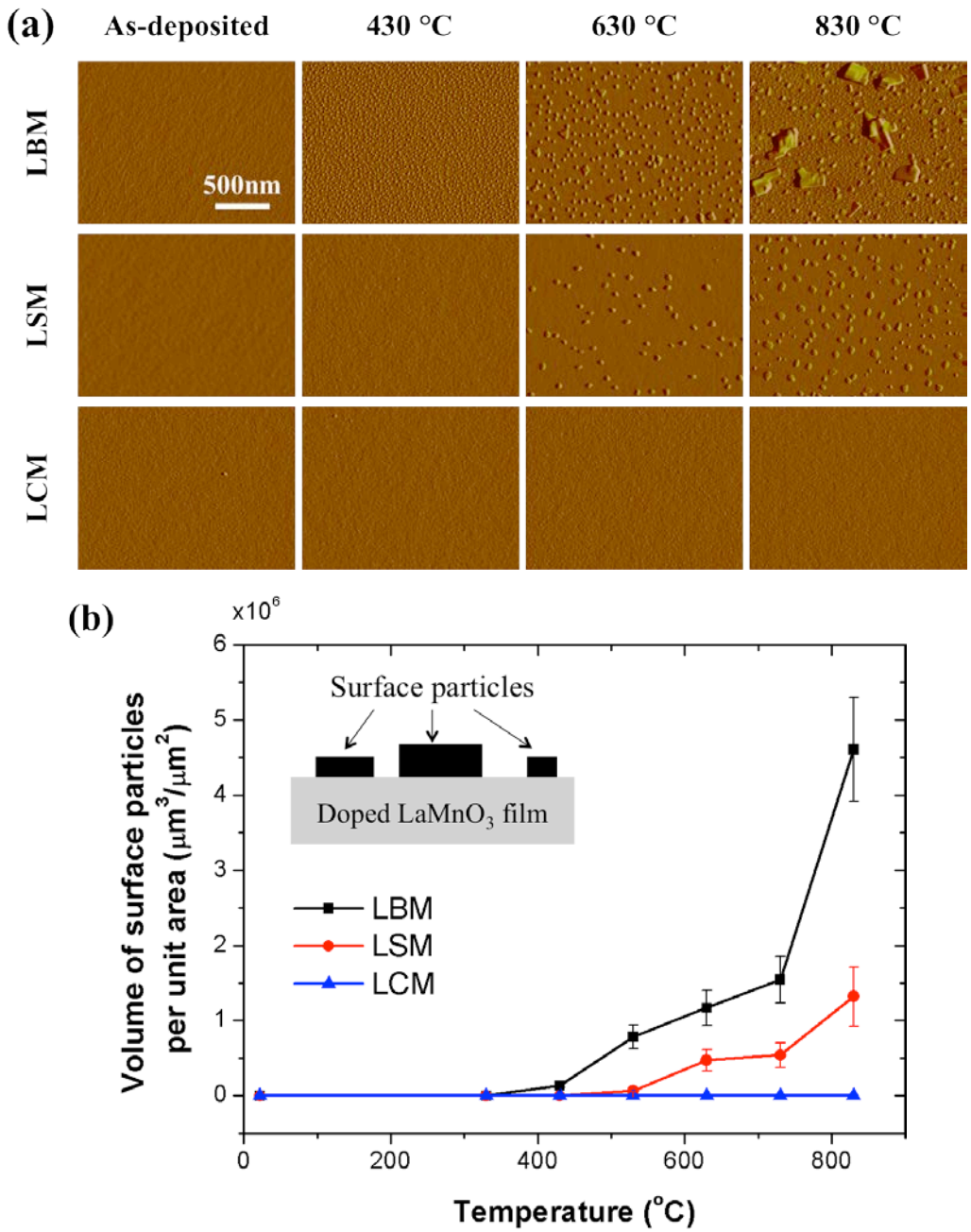

Figure 2. (a) AFM amplitude images of the Ba-, Sr- and Ca-doped $LaMnO_3$ thin film surfaces as a function of annealing temperature. Each column represents the surface morphology after annealing in air for 1 hr at the temperatures stated on the top. Each row represents the surface morphology of LBM, LSM, and LCM. (b) The volume per unit area of the surface particles, calculated from the AFM images, as a function of annealing temperature for LCM, LSM and LBM.

3.1.2. Heterogeneous surface chemistry upon dopant segregation correlates with dopant size

The changes in surface chemistry, concurrently with the structural changes presented above, were also found to be significant, and correlated strongly with the size mismatch between the dopant and host cations. Figure 3 shows the normalized cation intensity ratios from the near-surface region of the doped $LaMnO_3$ thin films with the three dopants. The detailed quantification and normalization process was described in Section 2.1.2. Dopant-to-Mn (D/Mn) ratios increased with the annealing temperature (Figure 3(a)). The chemical changes upon annealing were larger with the larger size mismatch between the dopant and host cations, consistently with the structural changes observed by AFM. LBM films (the largest size mismatch) showed the greatest increase in D/Mn ratios, followed by LSM films. LCM (the smallest size mismatch) films showed the smallest extent of dopant segregation at the surface. The observed dependency of structural and chemical changes on the size mismatch among the A-site cations substantiates that the elastic energy minimization plays a key role in cation rearrangements as a driving force. However, clearly the size mismatch is not the only player, because even Ca was found to enrich at the surface despite the fact that its size deviates from La only a very small fraction. Moreover, Figure 3(b) shows that the dopant-to-La (D/La) ratios also increased with annealing temperatures similarly to the behavior of D/Mn ratios in Figure 3(a). The increase of D/Mn and D/La ratios concurrently with the appearance of surface particles indicates that these surface particles are mainly composed of the dopant cations. The high-resolution analysis of the core level photoemission spectra of the dopant cations with different emission angles was performed to enable a quantitative analysis of the chemical environment as a function of depth from the film surface in a non-destructive way.[1,30] This analysis helps to deduce if the dopant segregation is associated with a secondary phase formation or if it takes place on the perovskite-terminated lattice. The concomitant increase of surface components with the total increase of dopant content at the surface indicates that the segregated dopant may form a non-perovskite coordination at the surface. (see Figures S3 and S4 in Supporting Information).

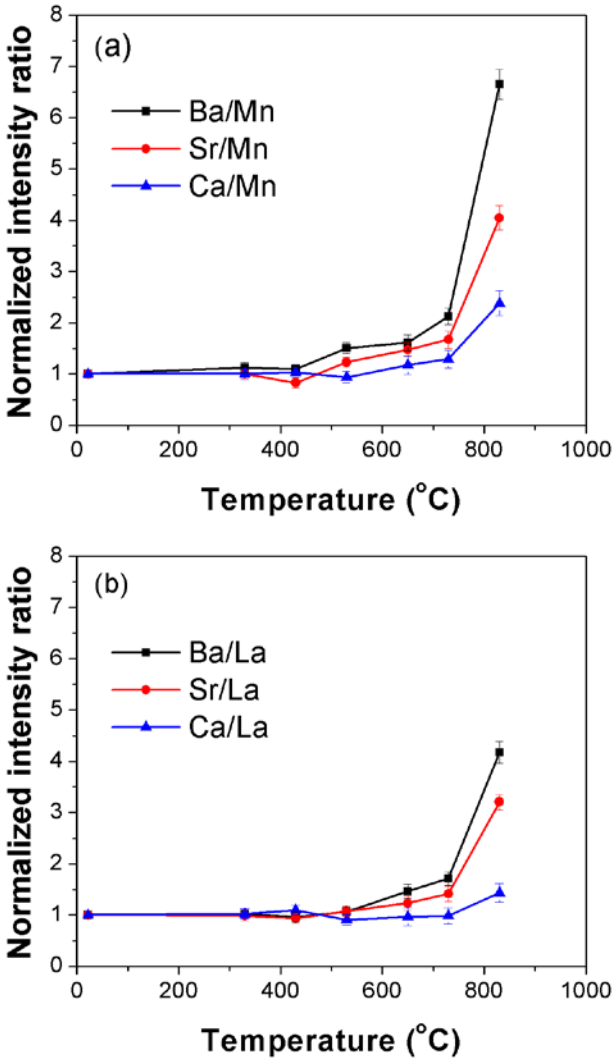

Figure 3. Normalized cation intensity ratios quantified by AR-XPS and AFM as a function of annealing temperature. (a) D/Mn ratios and (b) D/La ratios.

Formation of dopant-enriched secondary phases, which was inferred from the analysis in Figures S3 and S4, was further supported by subsequent localized measurements of chemical composition using AES. Figure 4(a-d) shows the elemental maps on LBM films annealed at 830 °C. Brighter color represents higher intensity of each element. A higher concentration of Ba and lower concentrations of La and Mn were found in the surface particles. Figure 4(e-f) shows the localized chemical intensity ratios acquired on top of surface particles (solid markers) and away from those phases (open markers). A significantly higher concentration of Ba in surface

particles was found compared to that on the as-deposited films, substantiating that these particles are mainly composed of Ba in secondary phases. Away from those phases, however, the concentration of Ba was lower than that on the as-deposited films, indicating the depletion of Ba on those regions. From this we conclude that the dopant cations separate out from the near-surface region, cluster and form the surface phases with a heterogeneous distribution, causing the depletion of dopant cations away from the surface particles. This behavior is similar to the Sr segregation structure that we found on LSC films in our prior work.[1] The LSM film surfaces in this work also behaved similar to the LBM films - agglomeration of Sr to form the surface particles and depletion of Sr on the rest of film surface (see Figure S5 in Supporting Information). The LCM films, however, showed no noticeable formation of surface particles after annealing up to 830 °C, as shown in Figure 2.

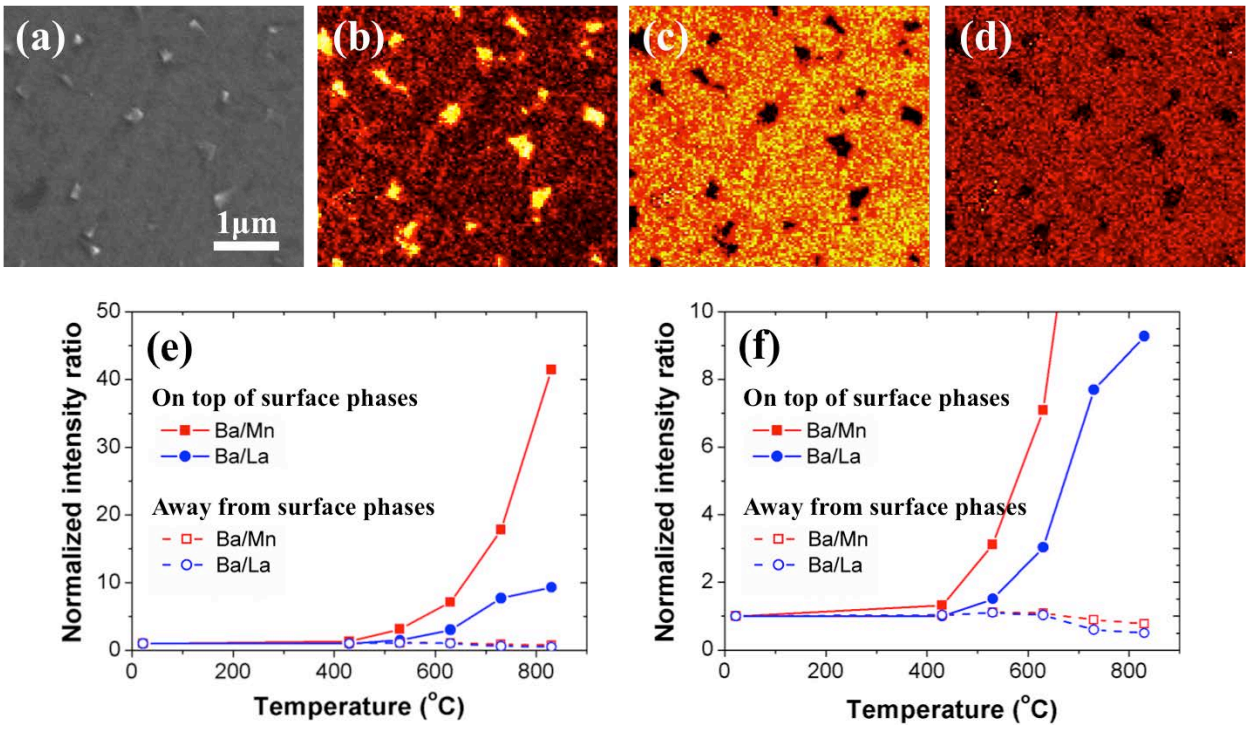

Figure 4. (a) SEM image on the annealed LBM films, and AES elemental maps deduced from (b) Ba MNN, (c) La MNN, and (d) Mn LMM. Point spectra on top of surface particles (solid markers) and away from surface particles (open markers): (e) normalized cation intensity ratio in full scale, and (f) plot that is zoomed into the maximum intensity ratio of 10 from (e).

We now turn our attention to the dependence of the geometry and chemistry of the surface heterogeneities on the dopant size. Figure 5 compares the D/Mn intensity ratios deduced from AES maps on the three films after annealing at 830 °C in air for 1 hr. LBM and LSM films showed formation of surface particles that were secondary phases with dopant-enrichment in them, while LCM films showed a uniform distribution of cations. Lateral dimension of these surface phases reveals that they were the largest on LBM films, and no noticeable formation of such heterogeneous secondary phases existed on LCM films. This behavior is consistent with the AFM analyses of surface particles in Figure 2. D/Mn ratios show that the dopant-enrichment at the surface is the highest on LBM films, and the least on LCM films, consistently with the AR-XPS analyses shown in Figure 3.

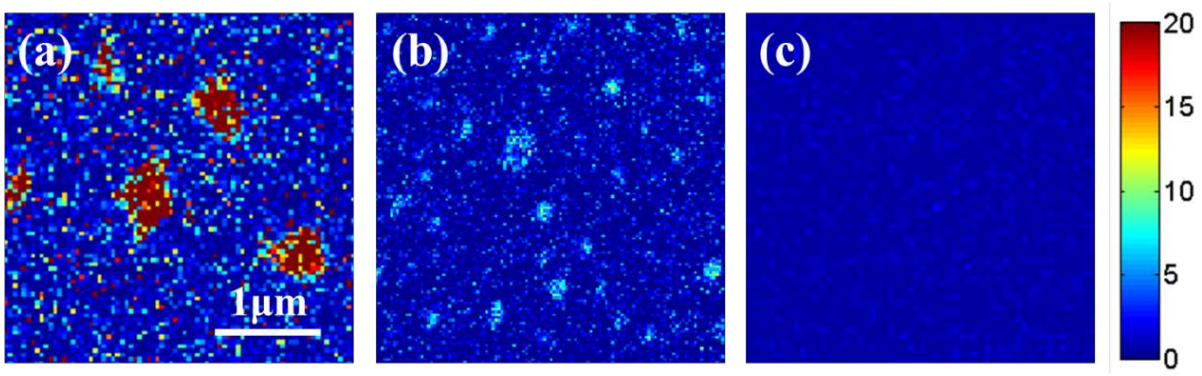

Figure 5. Cation intensity ratio maps on the three films after annealing at 800 °C for 1 hr. (a) Ba/Mn on LBM, (b) Sr/Mn on LSM, and (c) Ca/Mn on LCM.

From the structural and chemical analysis presented thus far, we conclude that: 1) the size mismatch between the dopant-host cations contribute significantly to the segregation of the dopant cations and secondary phase formation at the surface, 2) the larger size mismatch results in more cation rearrangements, and 3) dopant cations separate out more actively than the host cation to form dopant-rich secondary phases that are distributed heterogeneously at the surface. This dependency on the size mismatch substantiates that the elastic energy minimization plays an important role in cation rearrangements as a driving force. The larger ionic radius of the Ba^{2+} and Sr^{2+} than the La^{2+} ions is associated with larger lattice distortions compared to that with Ca^{2+}. The elastic energy in the doped $LaMnO_3$ films is minimized and a thermodynamic

equilibrium is reached by pushing the misfit dopants to the surface and relieving the accumulated strain in the film during annealing.[78] The relatively higher chemical stability of the Ca-doped $LaMnO_3$ film surface can then be ascribed to the relatively small size of Ca^{2+} that is very close to the size of La^{2+}. Thus, it is easier to accommodate Ca^{2+} in the bulk $LaMnO_3$ compared to the Ba^{2+} and Sr^{2+} cations. Indeed, the Ca-doped $LaMnO_3$ films showed a relatively smaller amount of dopant segregation, but there still existed Ca enrichment at the surface at elevated temperature despite its matching size to La^{2+}. This is where the electrostatic interaction must also be taken into account.

3.1.3. Oxygen pressure affects the dopant segregation via lattice parameter and charged defect distribution

We hypothesized that the elastic and electrostatic energy minimization together are responsible for describing the aforementioned cation rearrangements at the surface at elevated temperature. Here we provide another parameter, the oxygen pressure, as a means to deduce partially the effect of the elastic and electrostatic interactions of the dopants with the surface. The quantitative assessment of the contribution of the elastic and electrostatic energy to the cation rearrangements will be discussed with the theoretical and computational results in the Section 3.2 in detail.

By varying oxygen partial pressure, we impact the material: 1) structurally by expanding or contracting the oxide films, by the so-called ‘chemical expansivity’ phenomenon[78-82] (associated with the elastic energy), and 2) chemically by altering the distribution of charged point defects and localized electrons (associated with the electrostatic interaction). First, the oxygen pressure during annealing changes the lattice parameters of perovskite oxide films: the higher oxygen pressure incorporates oxygen into the lattice and contracts the lattice, while the lower oxygen pressure expands the lattice upon oxygen loss.[78,83-85] The changes in the lattice parameter directly couples to the elastic energy of the thin films as the driving force for cation rearrangements. Second, because the formation energy of oxygen vacancies is typically smaller at the surface compared to the bulk of oxides[63,64], a high concentration of oxygen vacancies is expected on the top surface compared to bulk. Beneath the positively charged surface of a mixed ionic electronic conductor oxide, a space charge layer can exist with an increase in

electron concentration. By decreasing the oxygen pressure and reducing the doped manganite films, the electronic charge carrier density increases and thus the Debye screening length would decrease. Therefore, one can expect a decrease in the spatial extent and strength of the space charge region in reducing conditions. Such changes in the re-distribution of positively charged oxygen vacancies and negatively charged electrons couple to the electrostatic energy.

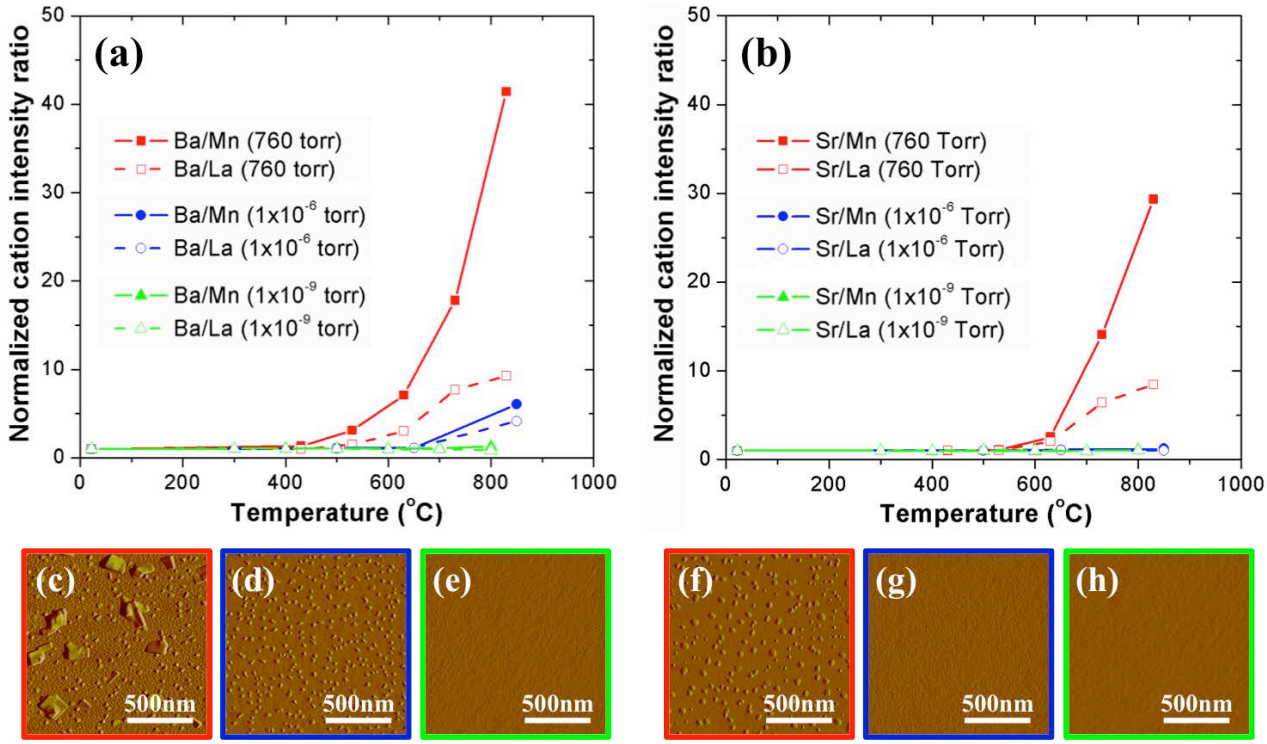

Figure 6. Normalized cation intensity ratios from point analyses using AES on (a) LBM and (b) LSM films. Surface morphology of LBM films after annealing at (c) 830 °C in 760 Torr, (d) 850 °C in 1×10^{-6} Torr, and (e) 800 °C in 1×10^{-9} Torr. Surface morphology of LSM films after annealing at (f) 830 °C in 760 Torr, (g) 850 °C in 1×10^{-6} Torr, and (h) 800 °C in 1×10^{-9} Torr.

To assess the effects of oxygen pressure during annealing on the surface chemistry and structure, three oxygen pressures were considered, 760 Torr (air), 1×10^{-6} Torr, and 1×10^{-9} Torr. Normalized cation intensity ratios were acquired by a point analysis of AES on top of surface phases (or from the background film surface if no secondary features existed). The extent of dopant segregation was found to be largest for thin films annealed in air (760 Torr), and to decrease with decreasing oxygen pressure, as shown by the D/Mn and D/La ratios in Figure 6(a)

and (b) for the LBM and LSM films, respectively. The changes in surface morphology (Figure 6(c-h)) were the largest after annealing in the highest oxygen pressure, while no noticeable changes were observed in the lowest oxygen pressure. Combined structural and chemical investigation clearly demonstrates the effects of the oxygen pressure during annealing: the higher oxygen pressure drives cations more toward the surface with segregation and secondary phase formation. Note that the dependency of cation rearrangements on the size mismatch among the host-dopant cations was still prevalent in the different oxygen pressures. After annealing in 1×10^{-6} Torr oxygen, for example, LBM films showed sizeable changes in the chemistry and structure at the surface, while LSM films did not show any discernible changes at or below 1×10^{-6} Torr.

This dependency of surface segregation on oxygen pressure found on the LBM, LSM and LCM films in this work was similar to that found on $La_{0.6}Sr_{0.4}Co_{0.2}Fe_{0.8}O_3$,[86] whose underlying reasons were not presented before. We make another analogy here to a recent result reported on the effect of electrochemical potential on the Sr segregation on $La_{0.75}Sr_{0.25}Cr_{0.5}Mn_{0.5}O_{3\pm\delta}$ thin film model electrodes.[87] In that work, cathodic polarization (reducing condition) was found to decrease the strontium surface concentration while anodic polarization (oxidizing condition) increased the strontium accumulation at the electrode surface. However, the underlying mechanisms were not clarified.

As noted above, there are two possible mechanisms that we hypothesized, by which the lower oxygen pressures can impact the surface dopant segregation; via the chemical expansion of the lattice, and via the change in the concentration and distribution of oxygen vacancies. In support of the first, substantial changes of the out-of-plane lattice parameters were found as a function of oxygen pressure. Figure 7 shows the high-resolution XRD patterns for the LBM, LSM, and LCM films with out-of-plane lattice parameters at each process step (as-deposited, annealed in 760 Torr, and annealed in 1×10^{-9} Torr). The lattice parameters decreased after annealing in the high oxygen pressure due to oxygen incorporation into the lattice, and increased after annealing at low oxygen pressure due to oxygen loss from the lattice. The out-of-plane lattice parameter of the as-deposited films (e.g. 3.993 Å for LBM) being higher than that of the bulk (e.g. 3.891 Å for LBM) showed that the films were oxygen deficient. It is known that manganite films

prepared by PLD are usually oxygen deficient with larger out-of-plane lattice parameters.[85,88,89] After annealing at 830 °C in 760 Torr, the out-of-plane lattice parameter decreased (e.g. to 3.883 Å from 3.993 Å for LBM). Annealing in the high oxygen pressure oxidizes Mn^{3+} to Mn^{4+} upon oxygen incorporation, resulting in the decrease of the out-of-plane lattice parameter.[89-91] After annealing at 800 °C in 1×10^{-9} Torr, in contrast, the out-of-plane lattice parameter increased (e.g. to 4.007 Å from 3.993 Å for LBM). At the low oxygen pressure, the oxygen vacancy formation in the films reduces Mn^{4+} to Mn^{3+}, resulting in an expansion of lattice unit cell.[78,85,88-91] The in-plane lattice parameters were expected to remain constant upon annealing because of the epitaxial coherency to the substrate.[85] The changes in the out-of-plane lattice parameters directly affected the volume in the films, and hence, the elastic strain energy in the system. This directly levers the tendency to cation rearrangements at the surface. Decrease in the out-of-plane lattice parameters upon annealing in 760 Torr (or upon oxygen uptake) drives the cations to segregate toward the surface to minimize the elastic energy in the system. Annealing in 1×10^{-9} Torr, however, increased the out-of-plane lattice parameters. Such chemically expanded lattice provides more space to accommodate the larger dopant cations in the bulk lattice, reducing the dopant elastic energy, and suppressing the dopant segregation at the surface.

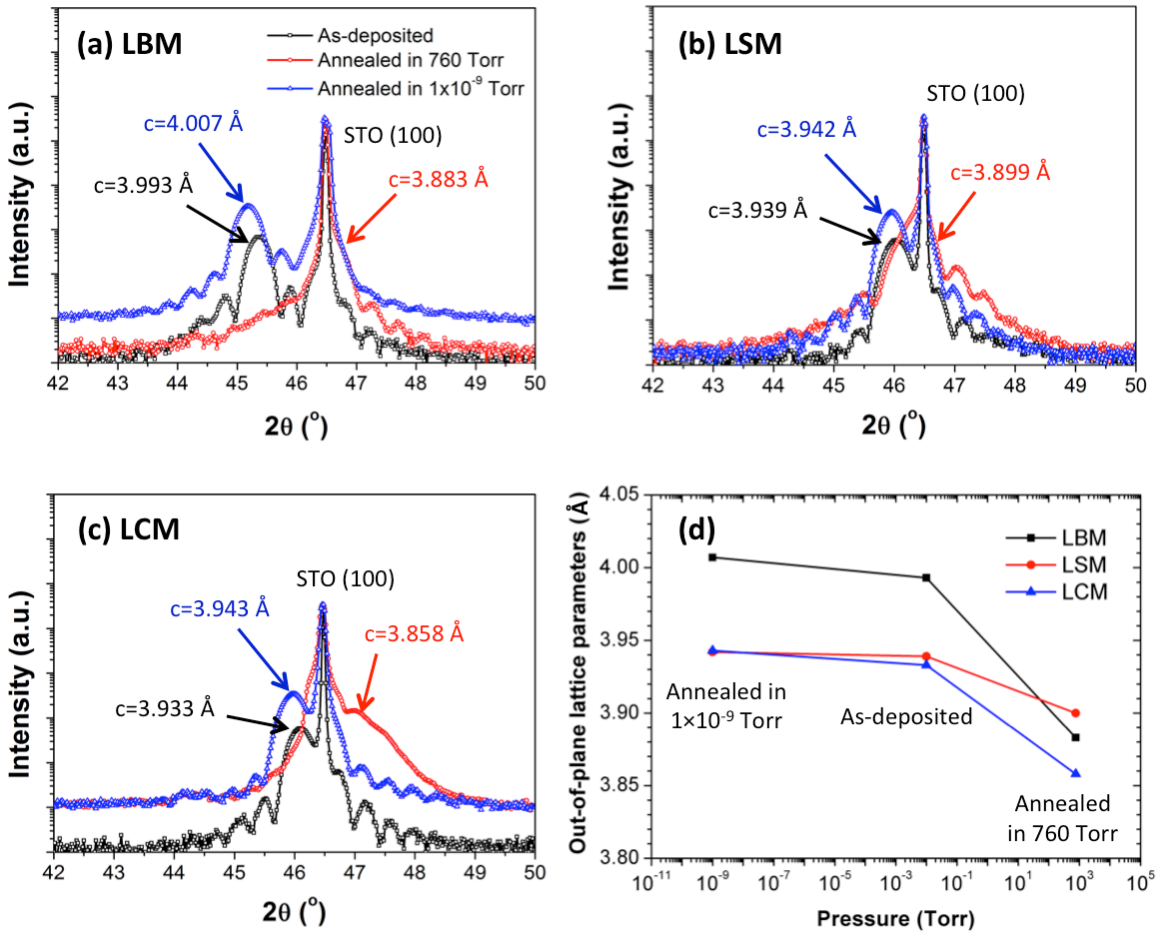

Figure 7. The high-resolution XRD patterns with out-of-plane lattice parameters at each process step of (a) LBM, (b) LSM, and (c) LCM films. Black, red, and blue lines represent the as-deposited, annealed in 760 Torr, and annealed in 1×10^{-9} Torr, respectively. (d) Out-of-plane lattice parameters of three films at each process step as a function of pressure.

In relation to the second mechanism by which oxygen pressure can affect dopant segregation, we provide the following discussion. Annealing at high temperatures reduces the oxide film and creates oxygen vacancies. The concentration and distribution of created oxygen vacancies depend on the oxygen pressure during the annealing. Approximately 10^6 times higher vacancy concentration at the surface than in the bulk (10^{-3} on surface and 10^{-9} in bulk) was predicted for $La_{0.1}Sr_{0.9}MnO_3$ under typical SOFC operating conditions at $pO_2=10^0$ atm and 1173 K.[80] Such higher concentration of oxygen vacancies at the top surface form a positive core compared to the bulk of the film. The space charge effects with a positive surface and a negative

subsurface[27,66,67] (discussed in section 2.2.2.2) results in a strong Coulombic attraction of the dopant cations to segregate toward the surface (see Figure S6 in Supporting Information, and bottom right in Figure 12). Note that the width of this space charge layer is expected to be narrow because of the short (~1 nm) screening length for heavily doped $LaMnO_3$.[68] Annealing in the very low oxygen pressures (10^{-6} - 10^{-9} Torr), on the other hand, creates a large concentration of oxygen vacancies throughout entire thickness of the oxide films because of the reduction in the free energy of vacancy formation at the low oxygen chemical potential. Furthermore, the concentration gradient of oxygen vacancies when annealed in the low oxygen pressures increases, for example going from 10^{-5} in the bulk to 10^{-1} at the surface of $La_{0.1}Sr_{0.9}MnO_3$ at $pO_2=10^{-9}$ atm and 1173 K.[80] Therefore, we expected a greater segregation of the dopant as the oxygen pressure decreases. However, we observed the opposite: dopant segregation decreased significantly with lowering the oxygen pressure in our experiments. This can be attributed to two possible hypothesis; first one related to the weakening of the electrostatic driver, and the second one related to the dominating extent of chemical expansion discussed above. The first can arise due to a change in the distribution of localized electrons. By decreasing the oxygen pressure and reducing the doped manganite films, the charge carrier density increases, and thus the Debye screening length would decrease. Therefore, one can expect a decrease in the spatial extent and strength of the space charge region beneath the surface in reducing conditions, and a weakening of the electrostatic attraction of the negatively charged dopant defects to the surface. The second hypothesis is based on the lattice expansion in reducing conditions. The observed lattice expansion of these manganite films in the low oxygen pressure (recall Figure 7) is substantial. Such a large chemical expansion (keeping the dopant cations in the bulk lattice) can dominate even if there were an increase of electrostatic attraction to the dopant cations, and suppress the cation segregation tendency at the surface in low oxygen pressure. In this experiment, we have direct experimental proof for the chemical expansion effect and we believe that one to be the dominant mechanism reducing the segregation at the lower oxygen pressures that we surveyed.

We excluded the possibility that the lower formation enthalpies of oxides and/or carbonates cause the different tendency to cation rearrangements. The standard formation enthalpies of bulk oxides and carbonates, however, provide no evidence to describe the observed trends in

cation rearrangements (Table S2 in Supporting Information). Furthermore, the surface carbonate phases, including $BaCO_3$, $SrCO_3$, $CaCO_3$, $La_2(CO_3)_3$, and $MnCO_3$, could be excluded on our samples due to the absence of a C 1s peak corresponding to the carbonate signature at temperatures above 500 °C (Figure S7 in Supporting Information). Lastly, when independent samples were annealed in pure O_2, the formation of secondary phase particles and the substantial increase in the D/Mn and D/La ratios at the surface were found again (Figures S8 and S9 in Supporting Information), very similar to the films annealed in air reported here. This similarity substantiates that the secondary phase formation involves mainly O_2 and not CO_2. As a result, we deduce that the secondary phases at the surface were dopant-enriched oxides and/or hydroxides rather than dopant-enriched carbonates.

3.2. Computational results

As discussed above, it is difficult to quantitatively separate out the structural and chemical effects of the oxygen pressure on the dopant segregation at the surface in experiments, while both effects can play a significant role. However, we turn now to computational results to show explicitly that charged defect interactions also play an important role in the segregation of dopants, and explain quantitatively the concerted role of both the elastic and electrostatic energy on this phenomenon. We note that the space charge effects described above are beyond the size scales that can be captured by DFT models currently. Therefore, we assessed the effect of charged defect distribution from the surface to the bulk of the $LnMnO_3$ films using hypothetical models without having to constrain the near-surface configuration as a space charge. In this way, we also generalize the role of electrostatic interactions in cation segregation regardless of the strength of space charge in a given composition.

3.2.1. Dopant segregation driven by elastic and electrostatic energy

Dopant segregation energy, E_{segr}, for the seven electrostatic interaction models with the three dopants on both $LaMnO_3$ and $SmMnO_3$ surfaces obtained from our DFT+*U* calculations and Eq. (S1) is shown in Figure 8(a) and (b). For both materials, two distinct trends are found; (1) the larger dopant cation segregates more strongly toward the surface; (2) the model where the dopant experiences the larger electrostatic attraction to the surface and the larger electrostatic

repulsion from the bulk shows a stronger tendency to enrich the dopant at the surface. For model 4, where there are no charged defects in the system, the negative segregation energy arises from the elastic energy effect as well as the electrostatic interaction of the dopant with the polar surface[49] on the *Ln*MnO_3 films. According to Eq. (1), elastic energy depends on the size difference between the host and dopant cations. If we plot E_{segr} from the DFT calculations for model 4 on each surface as a function of R_{dopant}-R_{host}, we observed an almost linear correlation between them (see Figure 8(c)). For both the $LaMnO_3$ and $SmMnO_3$ surfaces, therefore, the largest dopant, Ba (blue marks and line in Figure 8(a) and (b)), introduces the largest elastic energy into the system, and thus, is associated with a larger (negative) segregation energy and strongest tendency to enrich at the surface. The radius of Sm cation is smaller than that of La, and this causes a larger size difference of the host with respect to the dopants. Therefore, the segregation tendency of all three dopants on the $SmMnO_3$ surface was greater than that on the $LaMnO_3$. Importantly, we note that the predicted dependency of the segregation energy on the dopant size was well consistent with the surface chemical and structural analyses on the doped $LaMnO_3$ films in our experiments, reported in Figures 2-6. This consistency with the experimental results as well as the predictive extension of this behavior to $SmMnO_3$ by our calculations confirms that indeed the elastic energy minimization is an important contributor to dopant segregation on perovskite oxides.

It is clear that the electrostatic interaction variation in our models only depends on the distribution of oxygen- and cation-vacancies. Therefore, it is independent of the size of the dopant and host cations. We confirm this by plotting the changes in E_{segr} in Figure 8(a) and (b) relative to the E_{segr} of model 4 where there are no charged vacancies. In this case, all the relative segregation energies for each dopant converge approximately into one line that is consistent with the electrostatic energy obtained by Coulomb's law for each defect configuration (see Figure S10 in Supporting Information). This result clearly demonstrates that the electrostatic interaction of the dopant with the lattice defects is also an important contributor to dopant segregation on perovskite oxides.

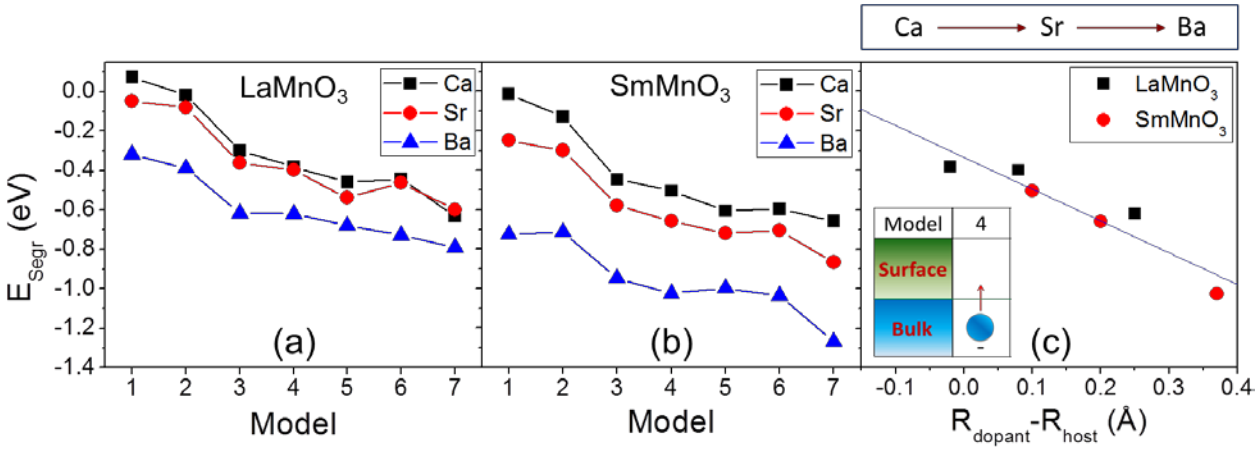

Figure 8. Surface segregation energies of Ca, Sr, and Ba dopants on (a) $LaMnO_3$ and (b) $SmMnO_3$ surfaces within the different electrostatic interaction models (1-7) described in Figure 1. Recall that the electrostatic attraction of the dopant to the surface increases from model 1 to model 7. (c) E_{segr} for model 4 on $LaMnO_3$ and $SmMnO_3$ as a function of R_{dopant}-R_{host}. The model 4 is illustrated in the inset.

3.2.2. Deconvoluting the contributions of the elastic and electrostatic energy in dopant segregation

Our next goal is to resolve quantitatively the contribution from the elastic and electrostatic interactions to the dopant segregation at the surface, and to examine if indeed E_{segr} can be represented as the sum of $E_{elastic}$ and $E_{electrostatic}$. As we noted in the previous section, it has been impossible to entirely decouple these two contributions experimentally, even when we varied the oxygen pressure. For this purpose, we used the analytical models (Sec. 2.2.2) to calculate both the elastic and electrostatic energies and compared them to the DFT-calculated total segregation energies. For each dopant, the elastic energy is *constant* over the seven electrostatic models, but strongly depends on the size difference between the dopant and the host cations. On the other hand, the electrostatic energy is shown with the same red curve in Figure 9(a-f) as function of the type of the defect configuration model, but independent of the dopant-host cation size mismatch. The two energy contributions are added (blue lines in Figure 9(a-f)) to compare them with the DFT-calculated total E_{segr} (black line in Figure 9(a-f)). Overall, the sum of two energy contributions was in reasonable agreement with the DFT-calculated E_{segr} on both surfaces within 0.16 ± 0.15 eV, which demonstrates that the elastic and electrostatic energies are

two important contributors to the segregation phenomenon. Especially for the Ba dopant, the agreement was seemingly very good within 0.01 ± 0.14 eV. For Ca and Sr dopants, however, the sum of the two energy contributions from the analytical models underestimated the DFT-calculated E_{segr} by 0.24 ± 0.09 eV. Such deviation between the DFT calculated E_{segr} and that calculated from the elastic and electrostatic energy models among all compositions is attributed to the possibility of other contributors, such as the surface polarization effect on manganites[92-94] that we did not explicitly assess. However, we emphasize that the surface polarization effect is inherently present in our DFT calculations. This can be realized from the negative E_{segr} value even for model 4 in Ca-doped $LaMnO_3$ where no charged vacancies are present and where the size of Ca and La are very close to each other.

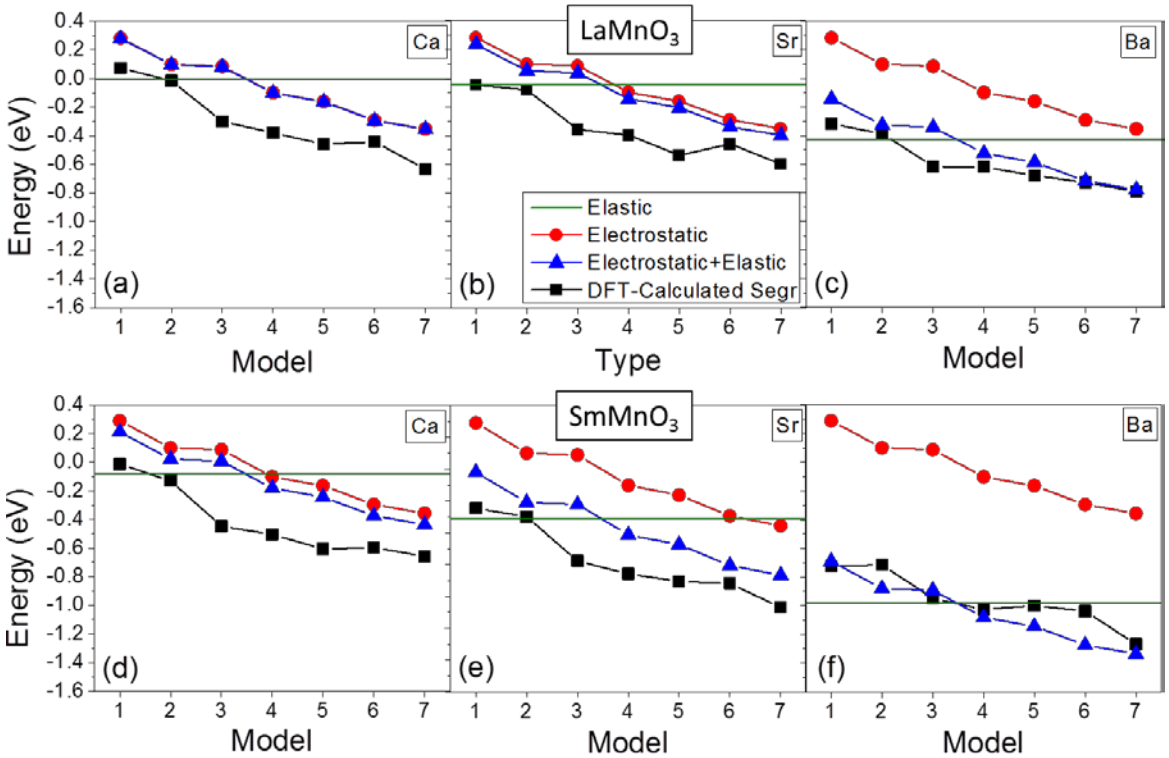

Figure 9. Comparison of the DFT-calculated total segregation energy, E_{segr}, with the one calculated analytically as the sum of the elastic and electrostatic energy. The green, red, blue and black lines denote the analytically calculated elastic energy, electrostatic energy, sum of electrostatic and elastic energies and DFT-calculated E_{segr}, respectively, as a function of model 1-7.

Inaccuracies in the analytical models are also among the possible sources of the deviation between the DFT results and the analytical model results. Friedel equation[61] (Eq. (1)) cannot perfectly describe our system due to its limitations as noted above; the dopant concentration in our model is not infinitely dilute; and due to the limited size of our supercell the lattice strain energy induced by the larger dopant would not be fully relaxed upon the segregation. In addition, for elastic energy calculations, we have used Shannon's ionic radii that are valid for purely ionic systems; on the other hand, the perovskite systems that we deal with here are not fully ionic. For electrostatic energy, Coulomb's law (Eq. (2)) was employed, but it is also valid for the purely ionic materials. In spite of these, Figure 9 clearly shows that the elastic and electrostatic energies are major contributors to the segregation of dopant on the *Ln*MnO_3 surfaces.

Based on the results in Figure 9, it is possible to predict the segregation energy to a large extent simply by the sum of the elastic and electrostatic energies that can be calculated from the analytic models described in Sec. 2.2.2. Using these models can make an efficient route to estimate the trends in the enhancement or depletion behavior of dopants on a range of perovskite oxides without having to perform many of the computationally expensive DFT calculations. For the different types of perovskite oxides, the elastic and electrostatic contributions to the E_{segr} would vary. For example, LSC, another widely studied SOFC cathode,[28,95-97] is known to be a relatively more elastic material than LSM with a Young's modulus (64.4 GPa for $La_{0.8}Sr_{0.2}CoO_3$ at room temperature[98]) smaller than that of LSM (129 GPa for $La_{0.67}Sr_{0.33}MnO_3$ at room temperature[99]). LSC also reduces more easily to form more oxygen vacancies at the surface compared to LSM,[100] inducing larger electrostatic attraction to the dopants. We can therefore expect that the elastic energy contribution to dopant segregation on LSC is less while the electrostatic energy contribution is more compared to that on LSM.

3.2.2. Diffusion kinetics of dopant cations

Sections above discussed the driving forces to segregation in the context of thermodynamics of this phenomenon. Kinetics of the unit processes involved in the segregation is also important to consider because at a given temperature and time the surface composition is an outcome of the combined effects of thermodynamics and kinetics. For this purpose, the diffusion of segregating

cations must be carefully considered. We performed NEB calculations for cation diffusion with the vacancy exchange mechanism for each dopant and host cation in the bulk and near the surface of the *Ln*MnO_3 system. The faster a cation diffuses, the quicker it can enrich at the surface given a driving force to it to migrate to the surface. Opposite to the results from the thermodynamic driving role of the elastic energy (Sec. 3.2.1), the larger cation was found to diffuse slower toward the surface with a higher migration energy barrier (Figure 10). For example, Ba dopant has ~1.9 eV higher migration barrier than Ca both in the bulk and at the surface of $LaMnO_3$. This suggests that, while Ba is more strongly driven to the surface due to elastic energy minimization, its high migration barrier would lead to slower segregation kinetics. At reduced temperatures, the segregation process of the large cation may be kinetically hindered.

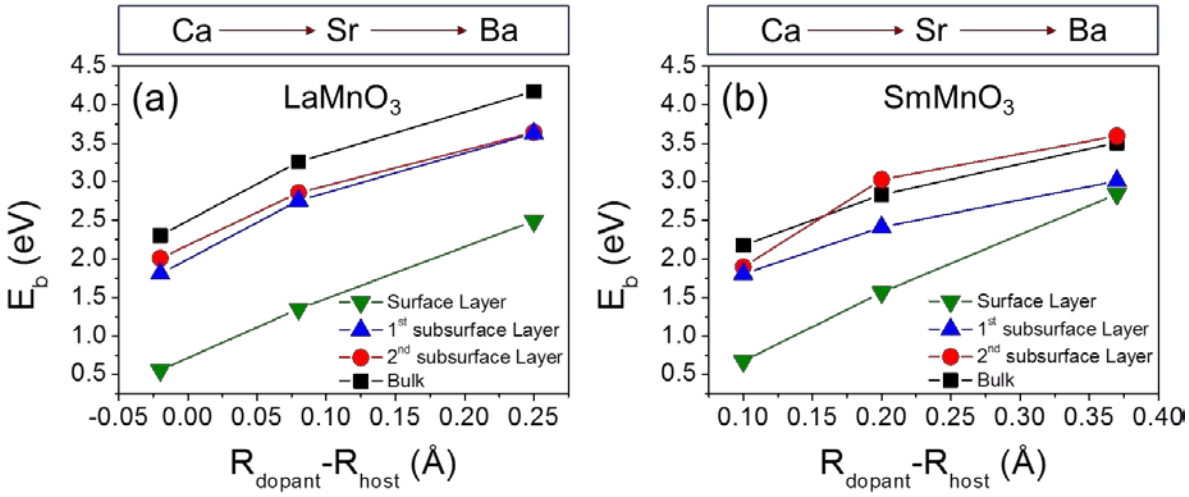

Figure 10. Migration energy barrier, E_b, of cation vacancies in (a) $LaMnO_3$ and (b) $SmMnO_3$ as a function dopant cation (size mismatch between the dopant and host cations, R_{dopant} - R_{host}) for diffusion of the dopant between each atomic layer from the surface into the bulk.

Overall the migration barriers for these cations in the bulk of the manganites were predicted to be large, ranging as ~2.2 - 4.2 eV. The considerably large migration barrier of cation vacancies in the bulk perovskite oxides was also reported in the literature; calculated values of 3.93 eV in $LaMnO_3$[101], 4.70 eV[102] or 4.52 eV[103] in $LaGaO_3$, and 4.00 eV in $LaFeO_3$[104] for La vacancy diffusion, and experimental activation energy of 4.98 eV in $LaCrO_3$[105] and 3.32 eV in $LaFeO_3$[106]

for La diffusion. This range of values is consistent with our DFT results in Figure 10. More importantly, we found that the migration barrier of these cations was significantly lower at the near surface (i.e. from the first subsurface layer to the surface) than in the bulk, by ~1.5 eV on both the $LaMnO_3$ and $SmMnO_3$ considered here. Specifically, we examined the change in the diffusion barrier of cation vacancies as a function of distance from the surface. For both materials, the cation migration was more facile as the position was closer to the top surface. This is attributed to the easier relaxation and flexibility of the structure near the surface, causing the dopant to migrate more easily than in the bulk.[107,108] As a result, the spatial extent of cation segregation is expected to be limited to the near-surface region and is not spread largely to the bulk of the material unless at very high temperatures.

3.3. Implications to electronic properties and electrochemical activity

The heterogeneous chemistry observed at the surface of the LBM and LSM films upon dopant segregation is expected to be associated with a heterogeneously distributed electronic and electrochemical behavior at the surface. Here we attempt to infer the impact of cation segregation and phase separation on the ORR kinetics at the cathode surface. Specifically, we investigated the correlation between the chemical heterogeneity and the electron transfer properties at the surface by contrasting the images obtained from two scanning probe techniques, AFM and STM. The result is demonstrated for LSM in Figure 11 that shows the surface image of LSM films after annealing at 830 °C in air with the two techniques. Interestingly, surface particles, which we confirmed to be secondary phases, appeared with similar lateral dimensions and shapes, but with opposite height contrast - protrusions with AFM scanning (i.e., higher profiles compared to the film surface), and depressions with STM scanning (i.e., lower profiles compared to the film surface). This contrast originates from the different sources for height profile information in these two techniques.[109] AFM scanning is associated directly with the true geometrical height. In contrast, the STM scanning is associated with the density of states at given bias voltage between the tip and the sample. Even if the feature is geometrically protruding from the surface, it appears depressed if the feature is less conducting or insulating compared to the rest of the film surface. This observation is supported by the drastically different energy gaps between the pristine LSM film and insulating SrO

phases; 2.1-2.6 eV for LSM films from our previous work[30,33] and 5.7-5.9 eV for SrO[110]. Therefore, this image contrast provides a direct evidence that the secondary phases formed upon dopant segregation are electronically more insulating than the rest of the film surface. Such insulating phases hinder the charge transfer on the cathode surfaces, lowering the rate of oxygen reduction on the cathode.[1,34,111,112] Annealed LBM film surfaces also showed a similar contrast between the AFM and STM images, presented in Figure S11 in Supporting Information.

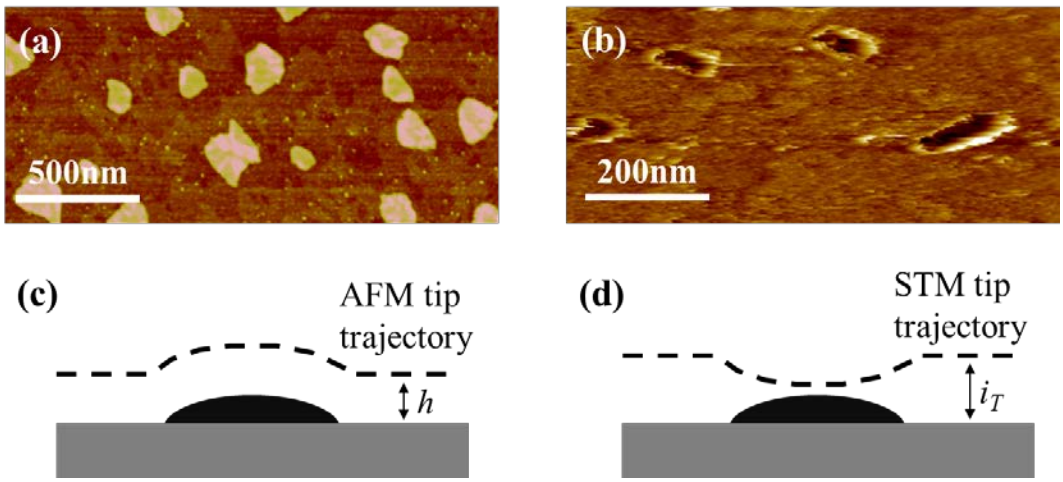

Figure 11. Surface morphology of LSM films after annealing at 830 °C in air (a) by AFM and (b) by STM. The imaging mechanism is illustrated schematically (c) for AFM and (d) for STM. The dashed line represents the tip trajectory. *h* represents the true separation distance between the tip and the sample in AFM imaging, and i_T represents constant tunneling current that is maintained by varying the separation distance if the surface is electronically heterogeneous.

4. Conclusion

We demonstrated that the dopant cations on the A-site segregate toward the surface of the manganite based perovskite oxides: 1) to minimize the elastic energy due to a mismatch of the dopant and host cation sizes, and 2) to minimize the electrostatic energy due to the interactions between the dopant and the charged defects at the surface and in the space charge zone near the surface, in addition to the surface polarity effects discussed earlier.[49] To systematically induce elastic energy differences in the model system, *Ln*MnO_3, we varied the radius of the selected dopants (Ca, Sr, Ba) with respect to the host cations (La, Sm) while maintaining the same

charge. In annealing experiments, we varied the oxygen chemical potential, whose expected impact is two-fold; elastic energy via the chemical expansion, and the electrostatic interactions via the redistribution of charged defects near the surface. The integration of XPS, AES, XRD, AFM, and STM in our approach enabled us to characterize the extent of dopant segregation and structural transformations at the surface of model dense thin films. DFT calculations and analytical models enabled us to interpret our experiments, to quantitatively decouple the contributions of the elastic and electrostatic energy to the segregation thermodynamics, and to assess the kinetics of dopant diffusion. We found that the assessment of segregation energies based on the dopant elastic energy and electrostatic energy is reasonably accurate compared to the DFT results. This provides a practical means to predict and design perovskite oxide composition with minimal detrimental effects of cation segregation. Our findings on the dopant segregation behavior are summarized in Figure 12.

A smaller size mismatch between the host and dopant cations was found to suppress dopant segregation. In this study, the least segregation at the surface was predicted computationally for the Ca-La pair (the most for the Ba-Sm pair) and the same was observed experimentally. The diffusion kinetics of the larger dopants, Ba and Sr, was found to be slower, and can kinetically trap the segregation at reduced temperatures despite the larger elastic energy driving force. Because the cation migration was found to be more facile closer to the top surface, the spatial extent of cation segregation is expected to be enhanced in the near-surface region. The dopant segregation is significant at the high oxygen pressure, and was found to decrease in the low oxygen pressure at the same elevated temperatures. This was attributed to two possible mechanisms. First is the chemical expansion of the doped $LaMnO_3$ in the low oxygen pressures and contraction in the high oxygen pressures. In the former, the bulk lattice expands to accommodate the misfit large dopants and reduces the dopant strain energy. Second is the change in the distribution of charged species near the surface. In low oxygen pressure, the space charge effect is expected to decrease because of an increase in the charge carrier density, weakening the electrostatic attraction of the dopant defects to the surface. We demonstrated direct evidence of the chemical expansion/contraction effect on the cation segregation, using the lattice parameters deduced from high-resolution XRD patterns as a function of the oxygen

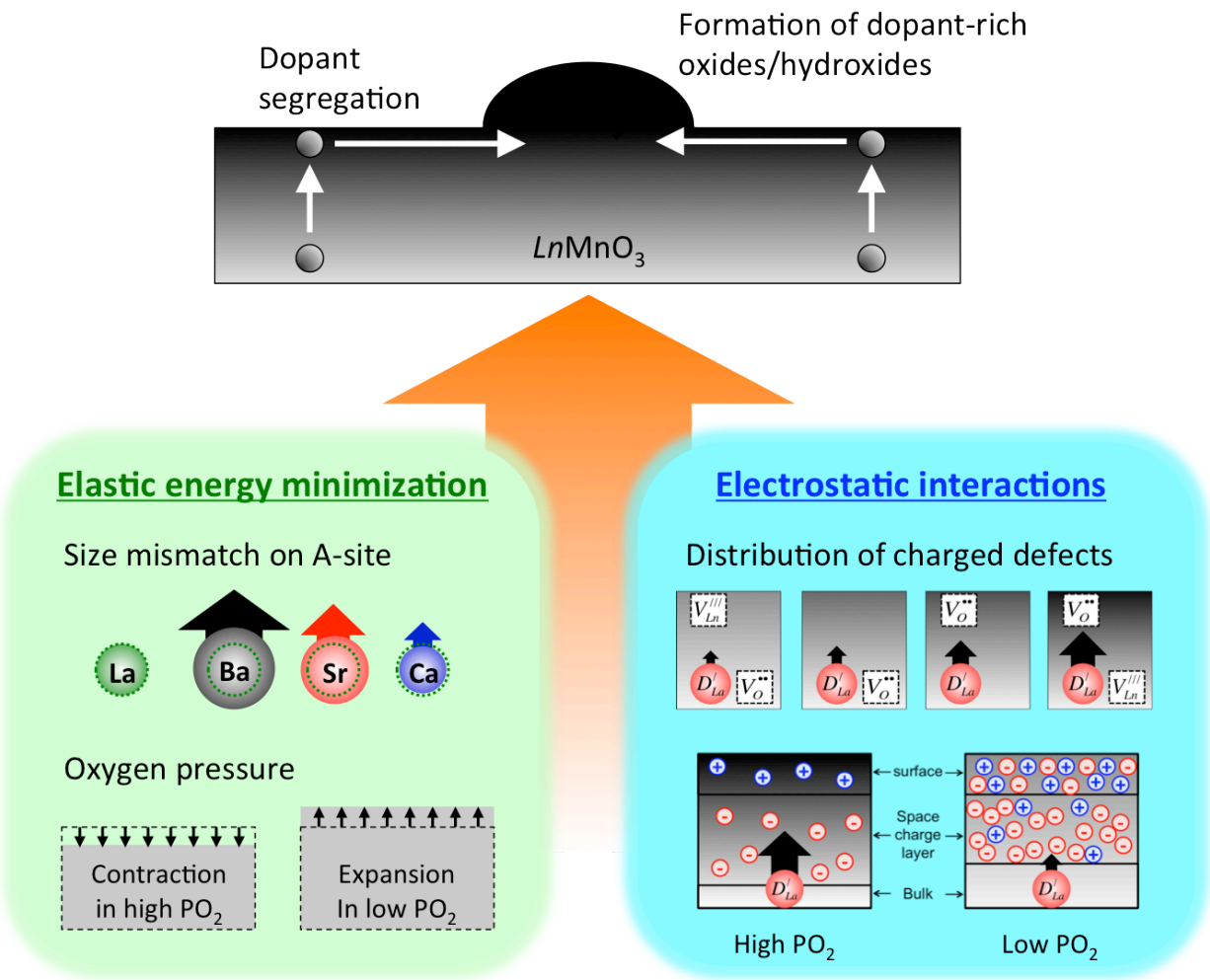

Figure 12. Illustration of the mechanisms that drive dopant segregation to the surface of *Ln*MnO_3.

pressure. We believe the chemical expansion to be the dominant factor that suppresses the segregation at the lower oxygen pressures. Segregation of Ba and Sr induced a heterogeneous structure and chemistry at the surface, in the form of dopant-oxides. Image-contrast between the topography recorded by AFM and STM revealed that these surface chemical heterogeneities were electronically insulating. Such insulating secondary phases at the surface are expected to hinder the charge transfer in ORR on the cathode surface.

We believe that the mechanisms that we identified to govern the cation segregation on the doped *Ln*MnO_3 films are actually applicable to a wider family of perovskite oxide surfaces. Both the

elastic and electrostatic interactions must be quantitatively taken into account in assessing the surface segregation of cations on this fascinatingly complex and technologically important family of materials. Systematic investigation of chemical, structural, and electrical impact of dopant segregation on such systems is important for a range of applications, including oxygen permeation membranes, batteries, magnetic and ferroelectric materials as well as fuel cells. Further in-depth studies on how these cation rearrangements correlate to the electrochemical activity and stability under a broader range of conditions is essential towards advancing our predictive capabilities to design optimal SOFC cathode surfaces.

Supporting Information

Figure S1, chemical analysis on heterogeneous surfaces with combination of AR-XPS and AFM; Figure S2, calculation of surface segregation energy with DFT-simulation; Figures S3 and S4, analysis of the high-resolution photoelectron spectra from the dopant core level emissions; Figure S5, localized chemical composition and structure on the annealed LSM films; Figure S6, schematic illustration of the local distribution of charged species at and near the surface; Figure S7, C 1s peak analysis as a function of temperature at two emission angles, Figures S8 and S9, surface structure and chemistry on LBM films upon annealing in different gas conditions; Figure S10, DFT-calculated surface segregation energies of Ca, Sr, and Ba dopant; Figure S11, surface structure of annealed LBM films images with AFM and STM; Table S1, DFT-calculated bulk (shear) modulus; and Table S2, standard enthalpies of formation for the possible secondary phases. This material is available free of charge via the Internet at http://pubs.acs.org.

Acknowledgements

The authors gratefully acknowledge the financial support from the US-DOE - Office of Fossil Energy, Grant No. DE-NT0004117 for the experimental component of this work, and Basic Energy Sciences, Grant No.DE-SC0002633 for the computational component of this work; the National Science Foundation for computing support through the XSEDE Program, Grant No.TG-ASC090058 and TG-DMR110004; Caroline Ross and Harry Tuller at MIT for the use of their PLD system, and Jae Jin Kim for his help on PLD target fabrication.

References

(1) Cai, Z.; Kubicek, M.; Fleig, J.; Yildiz, B.: *Chem. Mater.* **2012**, *24*, 1116-1127.
(2) Cai, Z.; Kuru, Y.; Han, J. W.; Chen, Y.; Yildiz, B.: *J. Am. Chem. Soc.* **2011**, *133*, 17696-17704.
(3) Chen, Y.; Jung, W.; Cai, Z.; Kim, J. J.; Tuller, H. L.; Yildiz, B.: *Energy Environ. Sci.* **2012**, *5*, 7979-7988.
(4) Crumlin, E. J.; Mutoro, E.; Ahn, S.-J.; la O', G. J.; Leonard, D. N.; Borisevich, A.; Biegalski, M. D.; Christen, H. M.; Shao-Horn, Y.: *J. Phys. Chem. Lett.* **2010**, *1*, 3149-3155.
(5) Jiang, S.: *J. Solid State Electrochem.* **2007**, *11*, 93-102.
(6) Jung, W.; Tuller, H. L.: *Energy Environ. Sci.* **2012**, *5*, 5370-5378.
(7) Kubicek, M.; Limbeck, A.; Frömling, T.; Hutter, H.; Fleig, J.: *J. Electrochem. Soc.* **2011**, *158*, B727-B734.
(8) Mutoro, E.; Crumlin, E. J.; Biegalski, M. D.; Christen, H. M.; Shao-Horn, Y.: *Energy Environ. Sci.* **2011**, *4*, 3689-3696.
(9) Shin, T. H.; Ida, S.; Ishihara, T.: *J. Am. Chem. Soc.* **2011**, *133*, 19399-19407.
(10) Tsai, C.-Y.; Dixon, A. G.; Ma, Y. H.; Moser, W. R.; Pascucci, M. R.: *J. Am. Ceram. Soc.* **1998**, *81*, 1437-1444.
(11) Yang, L.; Tan, L.; Gu, X.; Jin, W.; Zhang, L.; Xu, N.: *Ind. Eng. Chem. Res.* **2003**, *42*, 2299-2305.
(12) Levi, E.; Mitelman, A.; Aurbach, D.; Brunelli, M.: *Chem. Mater.* **2007**, *19*, 5131-5142.
(13) Yabuuchi, N.; Lu, Y.-C.; Mansour, A. N.; Chen, S.; Shao-Horn, Y.: *J. Electrochem. Soc.* **2011**, *158*, A192-A200.
(14) Yoon, W.-S.; Paik, Y.; Yang, X.-Q.; Balasubramanian, M.; McBreen, J.; Grey, C. P.: *Electrochem. Solid-State Lett.* **2002**, *5*, A263-A266.
(15) Lee, S. W.; Carlton, C.; Risch, M.; Surendranath, Y.; Chen, S.; Furutsuki, S.; Yamada, A.; Nocera, D. G.; Shao-Horn, Y.: *J. Am. Chem. Soc.* **2012**, *134*, 16959-16962.
(16) Serrate, D.; De Teresa, J. M.; Blasco, J.; Ibarra, M. R.; Morellon, L.; Ritter, C.: *Appl. Phys. Lett.* **2002**, *80*, 4573-4575.
(17) Rao, C. N. R.; Vanitha, P. V.: *Curr. Opin. Solid St. M.* **2002**, *6*, 97-106.
(18) Estrade, S.; Arbiol, J.; Peiro, F.; Infante, I. C.; Sanchez, F.; Fontcuberta, J.; de la Pena, F.; Walls, M.; Colliex, C.: *Appl. Phys. Lett.* **2008**, *93*, 112505-3.
(19) Estrade, S.; Rebled, J. M.; Arbiol, J.; Peiro, F.; Infante, I. C.; Herranz, G.; Sanchez, F.; Fontcuberta, J.; Cordoba, R.; Mendis, B. G.; Bleloch, A. L.: *Appl. Phys. Lett.* **2009**, *95*, 072507-3.
(20) Hamada, I.; Uozumi, A.; Morikawa, Y.; Yanase, A.; Katayama-Yoshida, H.: *J. Am. Chem. Soc.* **2011**, *133*, 18506-18509.
(21) Stavale, F.; Shao, X.; Nilius, N.; Freund, H.-J.; Prada, S.; Giordano, L.; Pacchioni, G.: *J. Am. Chem. Soc.* **2012**, *134*, 11380-11383.
(22) Arredondo, M.; Ramasse, Q. M.; Weyland, M.; Mahjoub, R.; Vrejoiu, I.; Hesse, D.; Browning, N. D.; Alexe, M.; Munroe, P.; Nagarajan, V.: *Adv. Mater.* **2010**, *22*, 2430-2434.
(23) Miles, G. C.; Stennett, M. C.; Reaney, I. M.; West, A. R.: *J. Mater. Chem.* **2005**, *15*, 798-802.
(24) Jiang, S. P.: *Journal of Solid State Electrochemistry* **2005**, *11*, 93-102.
(25) la O, G. J.; Ahn, S.-J.; Crumlin, E.; Orikasa, Y.; Biegalski, M. D.; Christen, H. M.; Shao-Horn, Y.: *Angew. Chem. Int. Ed.* **2010**, *49*, 5344-5347.
(26) Brandon, N. P.; Skinner, S.; Steele, B. C. H.: *Ann. Rev. Mater. Res.* **2003**, *33*, 183-213.
(27) Chueh, W. C.; Haile, S. M.: *Annu. Rev. Chem. Bio. Eng.* **2012**, *3*, 313-341.
(28) Adler, S. B.: *Chem. Rev.* **2004**, *104*, 4791-4844.
(29) Shao, Z.; Haile, S. M.: *Nature* **2004**, *431*, 170-173.
(30) Jalili, H.; Han, J. W.; Kuru, Y.; Cai, Z.; Yildiz, B.: *J. Phys. Chem. Lett.* **2011**, *2*, 801-807.
(31) Fister, T. T.; Fong, D. D.; Eastman, J. A.; Baldo, P. M.; Highland, M. J.; Fuoss, P. H.; Balasubramaniam, K. R.; Meador, J. C.; Salvador, P. A.: *Appl. Phys. Lett.* **2008**, *93*, 151904-3.
(32) Dulli, H.; Dowben, P. A.; Liou, S. H.; Plummer, E. W.: *Phys. Rev. B* **2000**, *62*, R14629-R14632.

(33) Katsiev, K.; Yildiz, B.; Balasubramaniam, K.; Salvador, P. A.: *Appl. Phys. Lett.* **2009**, *95*, 092106-3.
(34) Wang, W.; Jiang, S. P.: *Solid State Ion.* **2006**, *177*, 1361-1369.
(35) Szot, K.; Speier, W.: *Phys. Rev. B* **1999**, *60*, 5909-5926.
(36) Liang, Y.; Bonnell, D. A.: *Surf. Sci.* **1994**, *310*, 128-134.
(37) Han, J. W.; Kitchin, J. R.; Sholl, D. S.: *J. Chem. Phys.* **2009**, *130*, 124710-8.
(38) Lussier, A.; Dvorak, J.; Stadler, S.; Holroyd, J.; Liberati, M.; Arenholz, E.; Ogale, S. B.; Wu, T.; Venkatesan, T.; Idzerda, Y. U.: *Thin Solid Films* **2008**, *516*, 880-884.
(39) Lee, J.-R.; Chiang, Y.-M.: *Solid State Ionics* **1995**, *75*, 79-88.
(40) Battaile, C. C.; Najafabadi, R.; Srolovitz, D. J.: *J. Am. Ceram. Soc.* **1995**, *78*, 3195-3200.
(41) Wynblatt, P.; Rohrer, G. S.; Papillon, F.: *J. Eur. Ceram. Soc.* **2003**, *23*, 2841-2848.
(42) Guo, X.: *Solid State Ionics* **1995**, *81*, 235-242.
(43) Cockroft, N. J.; Lee, S. H.; Wright, J. C.: *Phys. Rev. B* **1991**, *44*, 4117-4126.
(44) Lee, H. B.; Prinz, F. B.; Cai, W.: *Acta Mater.* **2010**, *58*, 2197-2206.
(45) van der Heide, P. A. W.; Rabalais, J. W.: *Chem. Phys. Lett.* **1998**, *297*, 350-356.
(46) Lee, W.; Jung, H. J.; Lee, M. H.; Kim, Y.-B.; Park, J. S.; Sinclair, R.; Prinz, F. B.: *Adv. Func. Mater.* **2012**, *22*, 965-971.
(47) Estrade, S.; Arbiol, J.; Peiro, F.; Abad, L.; Laukhin, V.; Balcells, L.; Martinez, B.: *Appl. Phys. Lett.* **2007**, *91*, 252503-3.
(48) Kilner, J. A.: *Chem. Lett.* **2008**, *37*, 1012-1015.
(49) Harrison, W. A.: *Phys. Rev. B* **2011**, *83*, 155437.
(50) Horvath, G.; Gerblinger, J.; Meixner, H.; Giber, J.: *Sens. Act. B* **1996**, *32*, 93-99.
(51) Martin, M.: *J. Kor. Ceram. Soc.* **2012**, *49*, 29-36.
(52) Shannon, R.: *Acta Cryst. Sec. A* **1976**, *32*, 751-767.
(53) D'Souza, C. M.; Sammes, N. M.: *J. Amer. Ceram. Soc.* **2000**, *83*, 47-52.
(54) *NIST Database 82* **2001**, U.S. Department of Commerce.
(55) Kresse, G.; Furthmüller, J.: *Phys. Rev. B* **1996**, *54*, 11169-11186.
(56) Perdew, J. P.; Chevary, J. A.; Vosko, S. H.; Jackson, K. A.; Pederson, M. R.; Singh, D. J.; Fiolhais, C.: *Phys. Rev. B* **1992**, *46*, 6671-6687.
(57) Blöchl, P. E.: *Phys. Rev. B* **1994**, *50*, 17953.
(58) Dudarev, S. L.; Botton, G. A.; Savrasov, S. Y.; Humphreys, C. J.; Sutton, A. P.: *Phys. Rev. B* **1998**, *57*, 1505.
(59) Wang, L.; Maxisch, T.; Ceder, G.: *Phys. Rev. B* **2006**, *73*, 195107.
(60) Han, J. W.; Jalili, H.; Kuru, Y.; Cai, Z.; Yildiz, B.: *ECS Trans.* **2011**, *35*, 2097-2104.
(61) Friedel, J.: *Adv. Phys.* **1954**, *3*, 446-507.
(62) Le Page, Y.; Saxe, P.: *Phys. Rev. B* **2002**, *65*, 104104.
(63) Lee, Y.-L.; Morgan, D.: *ECS Trans.* **2009**, *25*, 2769-2774.
(64) Kuru, Y.; Marrocchelli, D.; Bishop, S. R.; Chen, D.; Yildiz, B.; Tuller, H. L.: *J. Electrochem. Soc.* **2012**, *159*, F799-F803.
(65) Kushima, A.; Yip, S.; Yildiz, B.: *Phys. Rev. B* **2010**, *82*, 115435.
(66) De Souza, R. A.; Martin, M.: *Phys. Chem. Chem. Phys.* **2008**, *10*, 2356-2367.
(67) Wang, R.-V.; McIntyre, P. C.: *J. Appl. Phys.* **2005**, *97*, 023508-8.
(68) Lu, H.; George, T. A.; Wang, Y.; Ketsman, I.; Burton, J. D.; Bark, C. W.; Ryu, S.; Kim, D. J.; Wang, J.; Binek, C.; Dowben, P. A.; Sokolov, A.; Eom, C. B.; Tsymbal, E. Y.; Gruverman, A.: *Appl. Phys. Lett.* **2012**, *100*, 232904-5.
(69) Picozzi, S.; Ma, C.; Yang, Z.; Bertacco, R.; Cantoni, M.; Cattoni, A.; Petti, D.; Brivio, S.; Ciccacci, F.: *Phys. Rev. B* **2007**, *75*, 094418.
(70) Islam, M. S.; Cherry, M.; Catlow, C. R. A.: *J. Solid State Chem.* **1996**, *124*, 230-237.
(71) Kovaleva, N.; Gavartin, J.; Shluger, A.; Boris, A.; Stoneham, A.: *J. Exp. Theor. Phys.* **2002**, *94*, 178-190.

(72) Onufriev, A.: **2010**, http://www.osti.gov/eprints/topicpages/documents/record/705/1923591.html.
(73) Mizusaki, J.; Mima, Y.; Yamauchi, S.; Fueki, K.; Tagawa, H.: *J. Solid State Chem.* **1989**, *80*, 102-111.
(74) Mizusaki, J.; Mori, N.; Takai, H.; Yonemura, Y.; Minamiue, H.; Tagawa, H.; Dokiya, M.; Inaba, H.; Naraya, K.; Sasamoto, T.; Hashimoto, T.: *Solid State Ionics* **2000**, *129*, 163-177.
(75) Liu, Z.; Cheng, L.-Z.; Han, M.-F.: *J. Power Sources* **2011**, *196*, 868-871.
(76) Konysheva, E. Y.; Xu, X.; Irvine, J. T. S.: *Adv. Mater.* **2012**, *24*, 528-532.
(77) Poulsen, F. W.: *Solid State Ionics* **2000**, *129*, 145-162.
(78) Murugavel, P.; Lee, J. H.; Lee, K.-B.; Park, J. H.; Chung, J.-S.; Yoon, J.-G.; Noh, T. W.: *J. Phys. D: Appl. Phys.* **2002**, *35*, 3166-3170.
(79) Kathrin, D.: *J. Phys. D: Appl. Phys.* **2006**, *39*, R125.
(80) Haghiri-Gosnet, A. M.; Renard, J. P.: *J. Phys. D: Appl. Phys.* **2003**, *36*, R127.
(81) Marrocchelli, D.; Bishop, S. R.; Tuller, H. L.; Yildiz, B.: *Adv. Func. Mater.* **2012**, *22*, 1958-1965.
(82) Marrocchelli, D.; Bishop, S. R.; Tuller, H. L.; Watson, G. W.; Yildiz, B.: *Phys. Chem. Chem. Phys.* **2012**, *14*, 12070-12074.
(83) Wu, W.; Wong, K. H.; Mak, C. L.; Choy, C. L.; Zhang, Y. H.: *J. Appl. Phys.* **2000**, *88*, 2068-2071.
(84) Ogale, A. S.; Shinde, S. R.; Kulkarni, V. N.; Higgins, J.; Choudhary, R. J.; Kundaliya, D. C.; Polleto, T.; Ogale, S. B.; Greene, R. L.; Venkatesan, T.: *Phys. Rev. B* **2004**, *69*, 235101.
(85) Yin, Z.; Gao, G.; Huang, Z.; Jiao, X.; Liu, Q.; Wu, W.: *J. Phys. D: Appl. Phys.* **2009**, *42*, 125002.
(86) Oh, D.; Gostovic, D.; Wachsman, E. D.: *J. Mater. Res.* **2012**, *27*, 1992-1999.
(87) Huber, A.-K.; Falk, M.; Rohnke, M.; Luer; Gregoratti, L.; Amati, M.; Janek, J.: *Phys. Chem. Chem. Phys.* **2012**, *14*, 751-758.
(88) Ju, H. L.; Gopalakrishnan, J.; Peng, J. L.; Li, Q.; Xiong, G. C.; Venkatesan, T.; Greene, R. L.: *Phys. Rev. B* **1995**, *51*, 6143-6146.
(89) Seo, S. H.; Kang, H. C.; Jang, H. W.; Noh, D. Y.: *Phys. Rev. B* **2005**, *71*, 012412.
(90) Goyal, A.; Rajeswari, M.; Shreekala, R.; Lofland, S. E.; Bhagat, S. M.; Boettcher, T.; Kwon, C.; Ramesh, R.; Venkatesan, T.: *Appl. Phys. Lett.* **1997**, *71*, 2535-2537.
(91) Salvato, M.; Vecchione, A.; De Santis, A.; Bobba, F.; Cucolo, A. M.: *J. Appl. Phys.* **2005**, *97*, 103712-5.
(92) B.E. Watts; F. Leccabue; G. Tallarida; S. Ferrari; M. Fanciulli; Padeletti, G.: *J. Electroceram.* **2003**, *11*, 139-147.
(93) Watts, B. E.: *Processing and Application of Ceramics* **2009**, *3*, 97-101.
(94) Hwang, H. Y.; Iwasa, Y.; Kawasaki, M.; Keimer, B.; Nagaosa, N.; Tokura, Y.: *Nature Mater.* **2012**, *11*, 103-113.
(95) Petrov, A. N.; Kononchuk, O. F.; Andreev, A. V.; Cherepanov, V. A.; Kofstad, P.: *Solid State Ionics* **1995**, *80*, 189-199.
(96) Kawada, T.; Yokokawa, H.: *Key. Eng. Mater.* **1997**, *125-126*, 187-248.
(97) Jacobson, A. J.: *Chem. Mater.* **2010**, *22*, 660-674.
(98) Orlovskaya, N.; Kleveland, K.; Grande, T.; Einarsrud, M.-A.: *J. Eur. Ceram. Soc.* **2000**, *20*, 51-56.
(99) Rajendran, V.; Muthu Kumaran, S.; Sivasubramanian, V.; Jayakumar, T.; Raj, B.: *Phys. Stat. Sol. (a)* **2003**, *195*, 350-358.
(100) Lee, Y.-L.; Kleis, J.; Rossmeisl, J.; Morgan, D.: *Phys. Rev. B* **2009**, *80*, 224101.
(101) Islam, M. S.: *J. Mater. Chem.* **2000**, *10*, 1027-1038.
(102) Khan, M. S.; Islam, M. S.; Bates, D. R.: *J. Phys. Chem. B* **1998**, *102*, 3099-3104.
(103) De Souza, R. A.; Maier, J.: *Phys. Chem. Chem. Phys.* **2003**, *5*, 740-748.
(104) Jones, A.; Islam, M. S.: *J. Phys. Chem. C* **2008**, *112*, 4455-4462.
(105) Akashi, T.; Nanko, M.; Maruyama, T.; Shiraishi, Y.; Tanabe, J.: *J. Electrochem. Soc.* **1998**, *145*, 2090-2094.

(106) Smith, J. B.; Norby, T.: *Solid State Ionics* **2006**, *177*, 639-646.
(107) Horita, T.; Ishikawa, M.; Yamaji, K.; Sakai, N.; Yokokawa, H.; Dokiya, M.: *Solid State Ionics* **1998**, *108*, 383-390.
(108) Horita, T.; Ishikawa, M.; Yamaji, K.; Sakai, N.; Yokokawa, H.; Dokiya, M.: *Solid State Ionics* **1999**, *124*, 301-307.
(109) Kuru, Y.; Jalili, H.; Cai, Z.; Yildiz, B.; Tuller, H. L.: *Adv. Mater.* **2011**, *23*, 4543-4548.
(110) Labidi, M.; Labidi, S.; Ghemid, S.; Meradji, H.; Hassan, F. E. H.: *Phys. Scripta* **2010**, *82*, 045605.
(111) Jiang, S.: *J. Solid State Electr.* **2007**, *11*, 93-102.
(112) Simner, S. P.; Anderson, M. D.; Engelhard, M. H.; Stevenson, J. W.: *Electrochem. Solid-State Lett.* **2006**, *9*, A478-A481.

TOC Figure

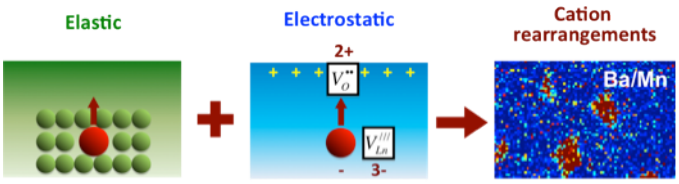

Characterization of the Surface Electronic Structure of Thin-Film Solid Oxide Fuel Cell Cathodes

Michael Weir, Stefan Krause, Lothar Weinhardt and Clemens Heske, *UNLV*

Overview

Catalytic reduction of oxygen is the limiting factor of solid oxide fuel cell (SOFC) performance. In addition to high catalytic activity, candidate materials must be thermally stable and chemically compatible with the electrolyte. Accordingly, many different variations of the perovskite family are being investigated as potential cathode materials for SOFCs. The electronic structure and chemical composition of the surface of these cathode materials will directly determine their catalytic activity. Thus, investigation of the surface of thin-film model cathodes will lead to a fundamental understanding of how to tune the electronic structure and related catalytic activity. The high temperature at which SOFCs operate (600-1000 °C) allows chemical and physical changes in the cathode materials that are not evident at room temperature. This concern has motivated both *ex-situ* and *in-situ* heating experiments, whereby the changes in the surface electronic structure as a function of temperature are elucidated.

Surface Chemical Composition:

In our project, $La_xSr_{(1-x)}MnO_3$ (LSM) samples are grown using pulsed laser deposition (PLD), with *x* reflecting the nominal bulk ratio between La and Sr. Samples referred to as LSMO8020, for example, are $La_{0.8}Sr_{0.2}MnO_3$ using the bulk stoichiometry. However, this does not have to be the chemical composition of the surface. Every crystalline material will show a relaxation of the surface due to the fact that half of the bonding partners of the bulk confirmation are missing. In a compound such as LSM, it can also lead to a segregation or depletion of one element at the

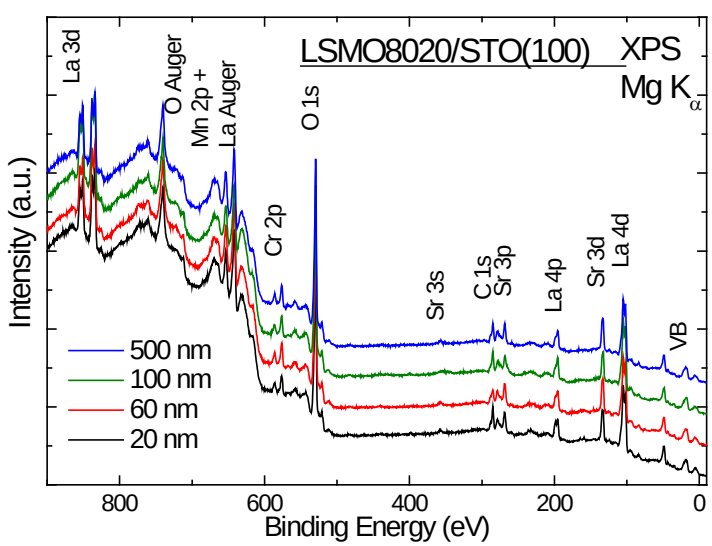

Figure 1. XPS survey spectra of $La_{0.8}Sr_{0.2}MnO_3$ films on STO (100). Each spectrum represents a different LSM film thickness.

surface. One powerful aspect of X-ray Photoelectron Spectroscopy (XPS) is the use of survey spectra to determine the chemical composition of the material *surface*. Furthermore, the relative abundance of different chemical elements can be determined through the relative intensity of various spectral lines. Figure 1 shows an example of XPS survey spectra for $La_{0.8}Sr_{0.2}MnO_3$ grown on the 100 plane of $SrTiO_3$ (STO). In this case, the expected elements are present (La, Sr, Mn, O) as well two elements not intended for the thin film, C and Cr. Carbon is commonly found on surfaces as a contaminant, especially when the sample has been exposed to air. The chromium, however, was the result of a small misalignment of a laser in the PLD, which was corrected for later samples. Confirming the elemental composition of the thin films is necessary to allow reproducibility and correct interpretation of performance results. More detailed analysis of the relative peak intensities reveals that Sr is enriched at the surface beyond the bulk stoichiometry as well as La, whereas Mn is depleted. This is a general trend found across many samples, while the magnitude of this enrichment varies.

In addition to the survey spectra, higher resolution XPS detail spectra were recorded for regions of interest including C1s/Sr 3p, O 1s, and Sr 3d/La 4d as shown in Figure 2. Here, the

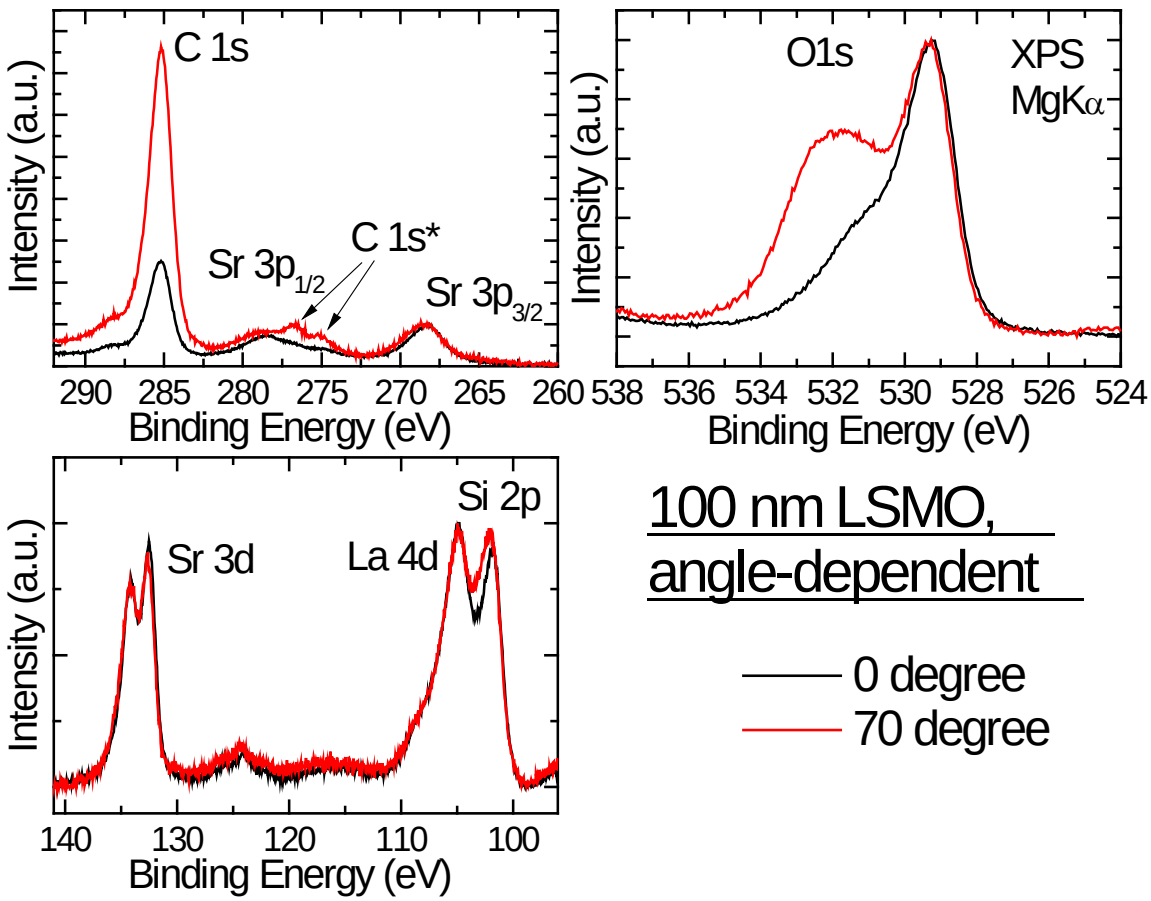

Figure 2. ARXPS detail spectra of a 100 nm LSM film. The figure shows the normal emission (0°) and the 70° off-normal detail spectra for the C 1s and Sr 3p region, the O 1s, and the Sr 3d and La 4d region. The off-normal spectra are more surface-sensitive and allow the comparison of surface and bulk properties of the sample.

sample surface was measured at normal emission (0°, more bulk sensitive) and 70° off-normal (more surface sensitive). By comparison of the two spectra, one can identify surface components and, if signals of different elements are in one window, changes in the relative stoichiometry at the surface. In the C 1s and Sr 3p region spectrum one can clearly see strong changes in the relative carbon-to-strontium ratio, which shows that the carbon is located mostly at the surface. The O 1s region reveals a surface component of the oxygen, which is shifted about 2 eV to higher binding energies.

The significant increase of this component with the strong carbon signal change being the only counterpart (Mn 2p did not show surface components) in the displayed spectra implies the existence of carbon oxide compounds, likely $SrCO_3$, at the surface. The strontium-to-lanthanum ratio stays constant and the change in the relative intensity of the La 4d component at 104 eV can be attributed to an additional spectral contribution of another impurity, namely silicon (Si 2p), at the surface (Si 2s is also visible in the survey spectrum, not shown; we note that the concentration is very small and that a Si contribution could so far only be found in the surface sensitive mode). Various treatments (annealing at 650 °C in 10^{-6} mbar pO_2, ion bombardment for 45 minutes with 500 eV Ar^+ ions) were found to remove the majority of the carbon species from the surface. A variety of other contaminants were found over time, but in close collaboration with the team at CMU we could identify sources of, e.g., sulfur and bismuth, which were then consequently eliminated.

Substrate Effects:

Earlier work of the MIT group showed that the films on the electrolyte substrate YSZ (Yttria-stabilized zirconia) are comparably rough and comprised of small grains. Therefore, other substrates, such as $NdGdO_3$ (NGO) and $SrTiO_3$ (STO), were utilized, which show high degrees of order and larger atomic terraces for thin LSM films. Figure 3 shows the detail XPS spectra (O 1s and C 1s/Sr 3p) of 10 nm LSMO7030 films on all three substrates. The first observable common feature is the oxygen component at the side of higher binding energy (“higher BE”). It is present for all surfaces and depends strongly on the emission angle, which identifies it as a surface component. For the C 1s and Sr 3p spectra, the carbon high-BE component shows a shift in position, while the intensity ratio of the two components remains the same. The strontium signal reveals a shifted high-BE energy component in the surface sensitive spectrum. The small but noticeable shift of the Sr 3p is connected to a second component in the Sr 3d (not shown) that corroborates this finding. The intensity and size of the shift in the oxygen component seems to be correlated with the size of the shift of the Sr 3p, which decreases from NGO to YSZ to STO. From this data, it can be concluded that all of the investigated surfaces are terminated by a Sr-O component, which, in the case of NGO, is also bound to carbon atoms. However, the dominance of this termination varies between the different substrates, which could be explained by a variation of the geometric structure of the films. Depending on the substrate, thin films can grow with different preferred surface facets, which can lead to different local surface termination and different behavior in the incorporation of the carbon impurity atoms during growth. Therefore,

LSMO7030

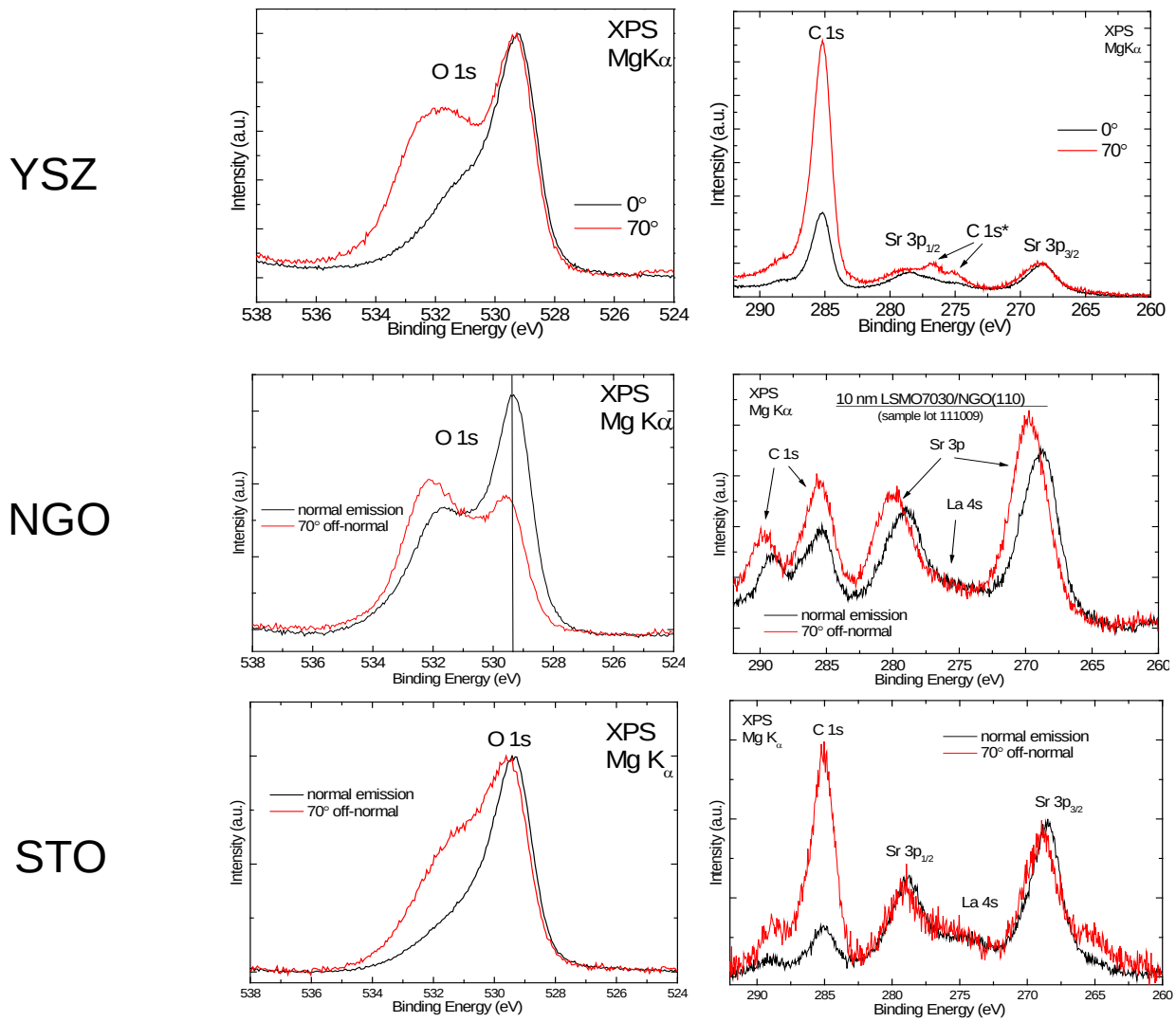

Figure 3. Comparison of detail XPS spectra (O 1s and C 1s/Sr 3p) of LSMO7030 thin films on different substrates. All spectra show a high-BE oxygen component that is more pronounced in the off-normal spectrum. A shift of a second carbon component is only present in the NGO case, and the shift of the Sr 3p is weak, but noticeable in the case of YSZ and STO substrates.

these effects have to be kept in mind when interpreting and comparing thin films grown on different substrates.

Film Thickness:

In the growth on any substrate, the crystal lattice parameters of substrate and film play an important role. Any significant mismatch will introduce strain to the thin film lattice that will decrease with growing thickness and therefore distance from the interface. STO has a larger lattice constant, which leads to tensile strain in the ab-plane and compression in the c-axis. Therefore, four different thicknesses (500 nm, 100 nm, 60 nm, 20 nm) of LSM were deposited on STO to investigate if also the surface chemical composition shows a dependence on strain. XPS detail spectra of this series are shown in Figure 4. These spectra show no consistent trends with film thickness, only that one film (100 nm) is significantly different from the others.

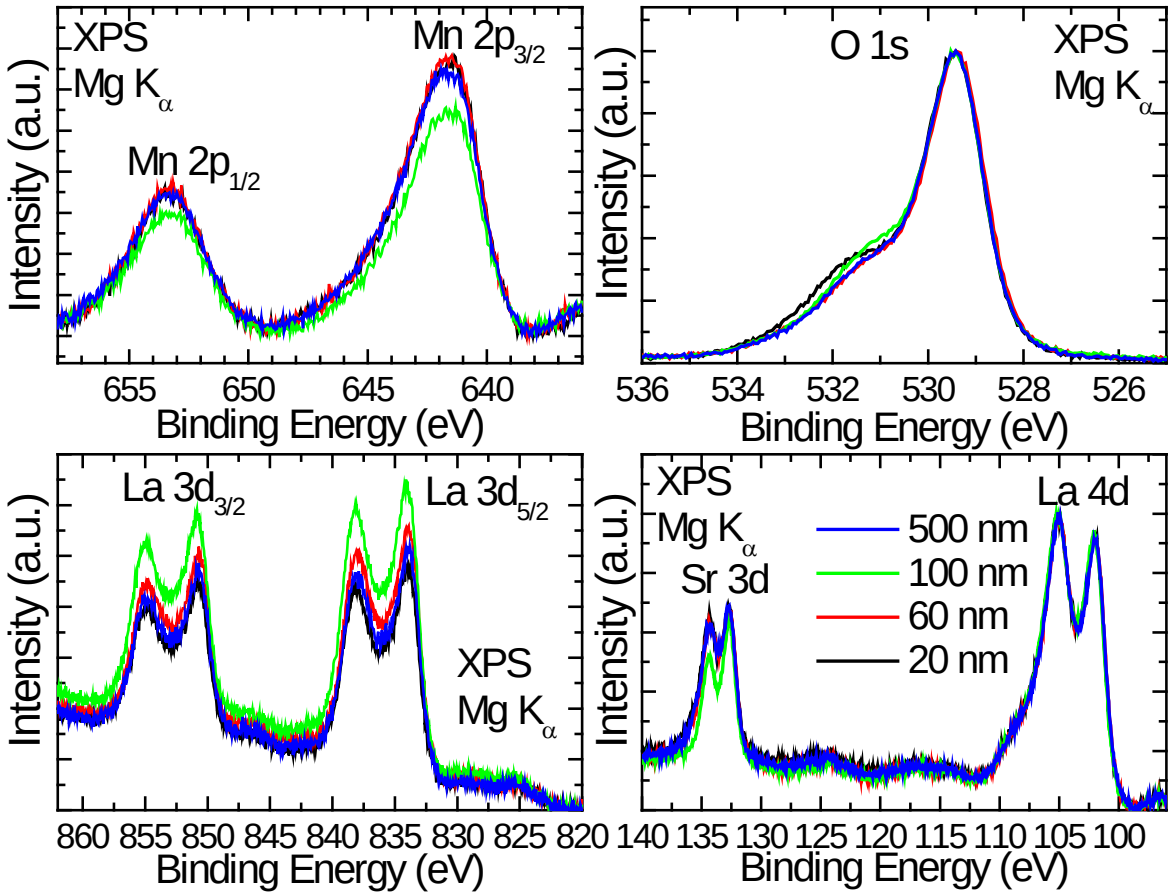

Figure 4. XPS detail spectra of $La_{0.8}Sr_{0.2}MnO_3$ on STO (100) for four different film thicknesses. The regions include Mn 2p, O 1s, La 3d, and Sr 3d/La 4d.

Specifically, there is less Mn and more La in the 100 nm sample. The Sr 3d peak also indicates a different chemical state by the change in ratios between the two peaks. The higher binding energy shoulder for the O 1s signal contains different dominant states. But with no consistent trend, we conclude that film thickness does not affect the surface composition of LSM deposited on STO.

Heating, *ex-situ*:

In addition to investigating synthesis-related changes in the thin-film cathodes, the high operating temperature of SOFCs has motivated studies on the effect of temperature on these films. A special vacuum chamber was commissioned to allow annealing in a controlled atmosphere, followed by transfer to the measurement chamber without exposure to air. Avoiding air exposure means that spectral differences will be caused by the material of interest and not by changes in the laboratory atmosphere (e.g., temperature, humidity). The first of these studies involved an *ex-situ* annealing treatment in 1 x 10^{-6} mbar pO_2 from 300 °C to 650 °C, as summarized in Figure 5. This figure shows the evolution of the surface composition as a function of annealing temperature with the data normalized to the as-received state. First, the most dramatic change is the decrease of the relative carbon surface concentration and an increase of

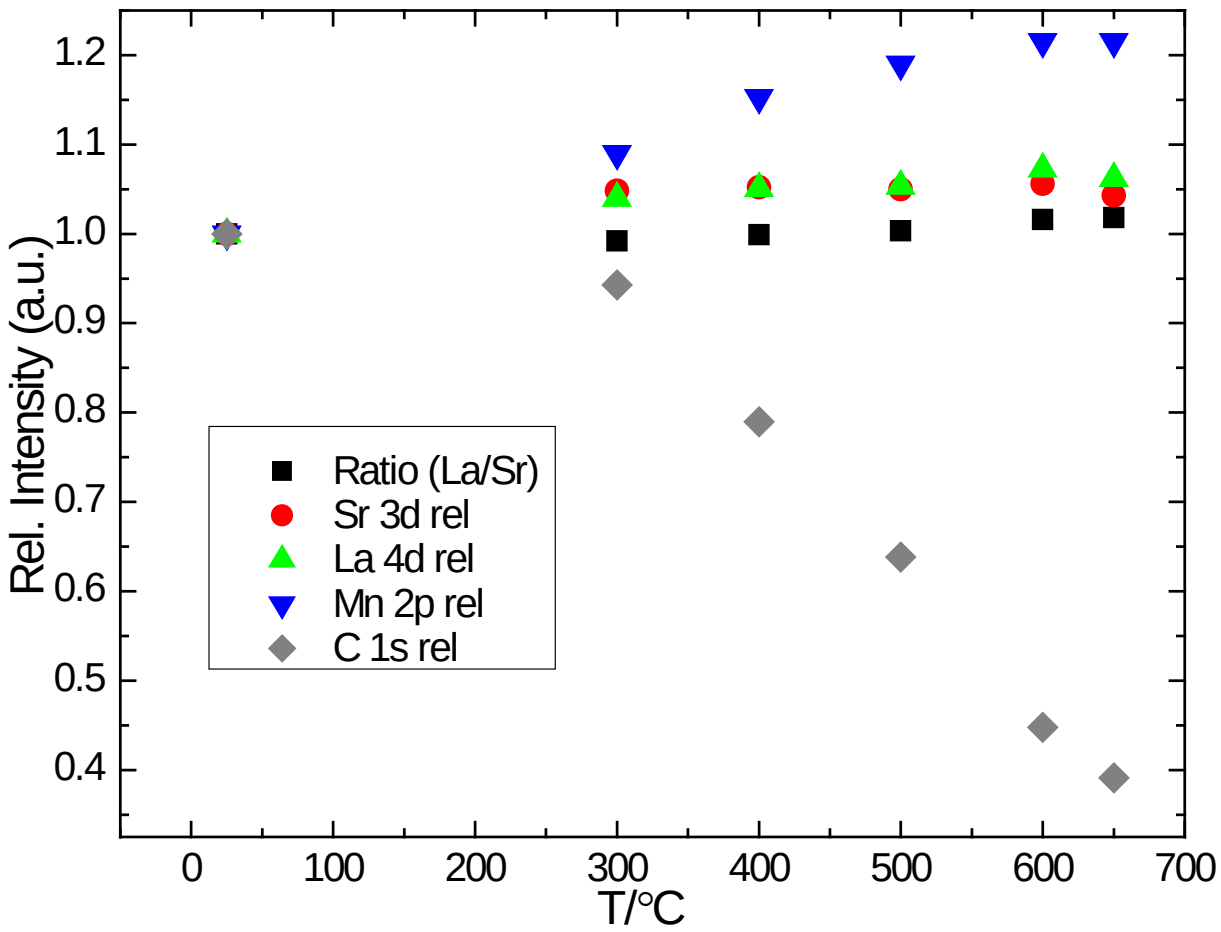

Figure 5. Relative changes of the La, Sr, C, and Mn XPS signal after ex situ annealing in 10^{-6} mbar pO_2.

the manganese intensity. This latter effect is due to the reduced attenuation of the Mn signal by a successively reduced (carbonate) overlayer. The effect is more pronounced for Mn than for La 4d and Sr 3d, which reflects that the higher BE peaks (i.e., Mn 2p) have a lower kinetic energy and thus are more surface-sensitive, i.e., more susceptible to attenuation in surface layers. Consequently, the La 3d peaks, which are found at an even higher binding energy, show an even more pronounced increase. Due to this dependence as a function of binding (kinetic) energy, it is impossible to unambiguously distinguish the effect of reduced attenuation from a potential Mn enrichment at the surface. Nevertheless, such an analysis can be performed for the La/Sr ratio. Using the La 4d and Sr 3d region, the peaks of which are close together in binding energy, a variation in the La/Sr intensity ratio directly relates to a change in the actual composition ratio as well. This ratio (black squares) shows no significant variation up to 500°C and then slightly increases (corresponding to a slight La enrichment of the surface). Even though the changes in this energy regime are very small (~3-4%), it corroborates earlier annealing experiments in air (up to 800°C), in which a 20% increase of the La/Sr ratio was found.

Heating, *in-situ*:

This *ex-situ* heating experiment was complemented by an *in-situ* series. *In-situ* in this case means heating in ultra-high vacuum (UHV) while measuring XPS at temperature. The vacuum environment might lead to a depletion of surface oxygen, but is necessary to perform XPS measurements. The advantage of an *in-situ* experiment is that it is possible to investigate reversible effects that only appear at elevated temperatures. One such series was performed on a 100 nm thick LSM film on STO, heating from room temperature (RT) up to 800 °C in 100 °C steps and then cooled back to RT. The first element of interest is oxygen, as it is generally believed that the surface loses oxygen during heating in UHV. A change in the shape of the O 1s signal after heating in pO_2 had been already observed in the previous annealing series. Figure 6 shows the same behavior for heating in UHV. A high-BE shoulder, which, based on our earlier work and the Sr data discussed below, can be attributed to a strontium oxide component, disappears with increasing temperature. The peaks are all normalized to the low binding energy side of the peak to compensate for background and excitation source intensity changes that are not related to a change in the oxygen content. A trend to an approximately 10% higher oxygen signal at higher temperatures can be seen. Analysis of the total area of the O 1s peaks implies

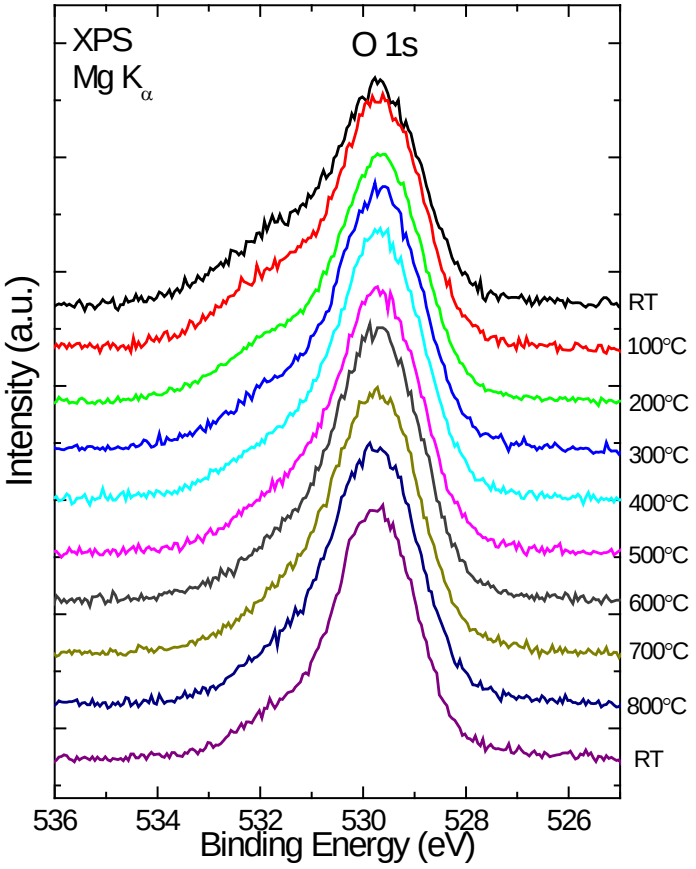

Figure 6. XPS detail spectra for the O 1s region recorded at increasing temperatures (top to bottom), as given on the right ordinate. A clear and irreversible change of the high BE shoulder can be observed.

that the oxygen content is independent of the temperature in this regime and that no detectable oxygen depletion occurs. Note that the overall oxygen signal intensity returns to its original (lower) RT value after complete cooldown. This is particularly interesting since some of the oxygen atoms were bound in a strontium oxide environment before the annealing series. As is evident from the O 1s spectra in Figure 6, however, this species does not return upon cooling to room temperature. With these results we can thus conclude that the overall oxygen content is higher, but constant, at temperatures above 100°C, and that a thermal cycle such as the one performed here modifies the chemical environment of some of the oxygen atoms permanently, while maintaining the overall amount of oxygen atoms on the surface. The experiments show that heating in UHV does not appear to lead to oxygen depletion of the surface. We find additional evidence for the presence of a strontium oxide species at the surfaces, which is removed during annealing. The data confirms the trends of La, Sr, and Mn surface concentration behavior in our earlier pO_2 annealing experiments and identifies them as irreversible. Additionally, a decrease of the Mn signal was found, which was not visible when heating in our earlier pO_2 annealing series due to (reduced) attenuation by the carbon-containing adlayer.

A second *in-situ* heating series was performed in order to correlate the surface chemical composition with Scanning Tunneling Spectroscopy (STS) results from the MIT group, which indicate that the bandgap of LSM changes from semiconductor to metallic behavior below 200°C in UHV. To that end, the same LSM sample was shipped to UNLV and measured using three different X-ray sources (Al K_α, Mg K_α, monochromated Al K_α) at both normal and 45°. The sample was annealed in the UHV system at UNLV using the procedure developed at MIT (1 x 10^{-5} mbar pO_2, 550 °C) in order to ensure the same starting point for the heating series. This heating series was initiated at room temperature (24 °C) and took 50 °C steps from 50 °C to 300 °C. The sample was then cooled back to room temperature for the final measurement. Figure 7 shows the XPS survey spectra for the non-monochromatized Al K_α source at normal emission. The heating series is displayed at each temperature step from room temperature (24 °C, blue, bottom) to the highest temperature (300 °C, red, second from top). The cooled sample was also measured and is shown in black (RT2, top). First, we note that all of the expected elements from the film are present (La, Sr, Mn, O), in addition to C and Mo. Much smaller signals from Na (1071 eV), F (685 eV), and Fe (710 and 722 eV) indicate the presence of these elements in low concentrations. Carbon is expected due to contamination from exposure to air during the various shipping procedures. The sample holder is responsible for the Mo signal. The sample position was adjusted to reduce the Mo 3d signal. However, the signal could not be fully removed due to the small sample size and the sampling area of the electron analyzer.

We also note that the secondary electron background for the 300 °C measurement is increased, especially for higher binding energies. This change in the background has been seen before in previous heating series, but under different conditions. We continue to investigate this phenomenon to determine the source. There are no significant indications of changes in the line shapes of the primary emission lines, i.e., the La 3d and 4d, Sr 3d, and Mn 2p lines. Furthermore, there are no immediately obvious changes in the relative concentrations of the different elements,

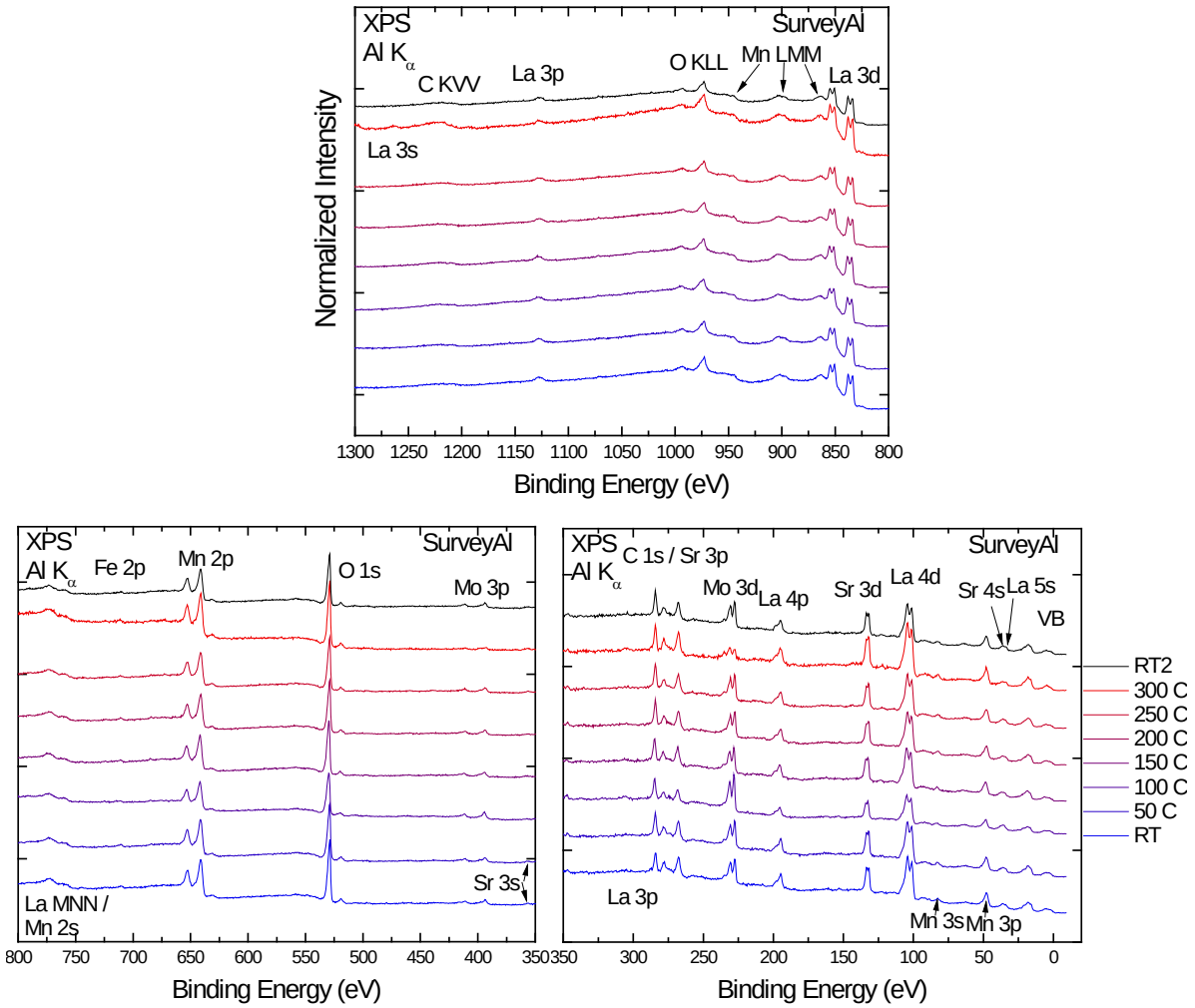

Figure 7. Al K_α Survey spectra of the LSM sample *in-situ* during heating. The spectra were measured at room temperature (RT, 24 °C), every 50 °C from 50 °C to 300 °C, and then again at room temperature after cooling (RT2). The heating series is represented by a transition from blue to red with temperature, while the black spectrum was recorded after cooling. All spectra were taken at normal emission. The spectra were normalized to (approximately) coincide in their overall background shape before being offset for visibility. The spectra were also split across three sections to emphasize low-intensity peaks.

in particular no evidence for a substantial Sr surface segregation due to the annealing in ultra-high vacuum. A thorough analysis of the individual detail spectra of these regions is currently performed to search for variations in the chemical environment of the various elements as a function of annealing temperature. This measurement series has produced a (very large) dataset, which is still under analysis.

Heating under atmosphere:

The *in-situ* studies were furthered by the design and testing of an *in-situ* cell capable of high temperatures (500 °C) and controlled atmospheres (up to 1 bar), spearheaded by our

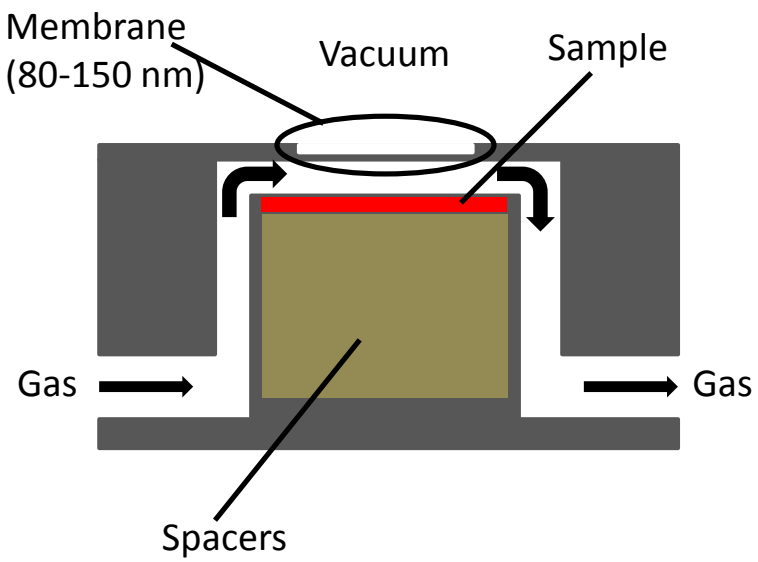

Figure 8. Scheme of the high-temperature *in-situ* gas/solid interface cell.

collaboration partners at the University of Würzburg, Germany. This cell will be used for soft X-ray Absorption Spectroscopy (XAS) and soft X-ray emission spectroscopy (XES) using the custom SALSA (Solid and Liquid Spectroscopic Analysis) endstation at Beamline 8.0.1 of the Advanced Light Source (ALS), Lawrence Berkeley National Laboratory. The SALSA endstation allows unique soft x-ray spectroscopy experiment in a dedicated experimental chamber for *in-situ* cells. The soft X-rays used for both, excitation and emission, exhibit a limited penetration depth even in a gas environment, and thus must be kept in the UHV environment of the beamline. Nevertheless, using a thin membrane to separate the gaseous environment inside the cell from the UHV of the endstation, it is possible to perform measurements under working conditions.

The cell holds samples of varying thicknesses at a constant distance from the X-ray window. Heating both the inlet gas and the sample is controlled by resistive external heaters. High temperatures (500 °C) are achieved by thermal isolation through ceramic barriers in the cell. Both inlet and outlet pressures are monitored and controlled externally. Initial cell testing included successful measurements of gasses and troubleshooting with a solid sample. Work will continue during future experimental campaigns at the ALS.

Successful *in-situ* experiments expand upon *ex-situ* knowledge. Therefore, in parallel with the cell development, initial XAS and XES measurements were performed on LSM samples on two different substrates, $LaAlO_3$ (LAO) and STO. The –A and –B films are nominally identical samples grown and shipped in the same batch. The XAS spectra in Figure 9 include data from both the films and the respective substrates. The spectra were normalized such that the baseline data at 520 eV and the maxima of the first major peak (~ 536 eV and 531 eV for LAO and STO, respectively) have equal intensity. Excitation energies were calibrated using the O K edge of a ZnO reference sample. In each case, the spectra of the LSM films are shown in black

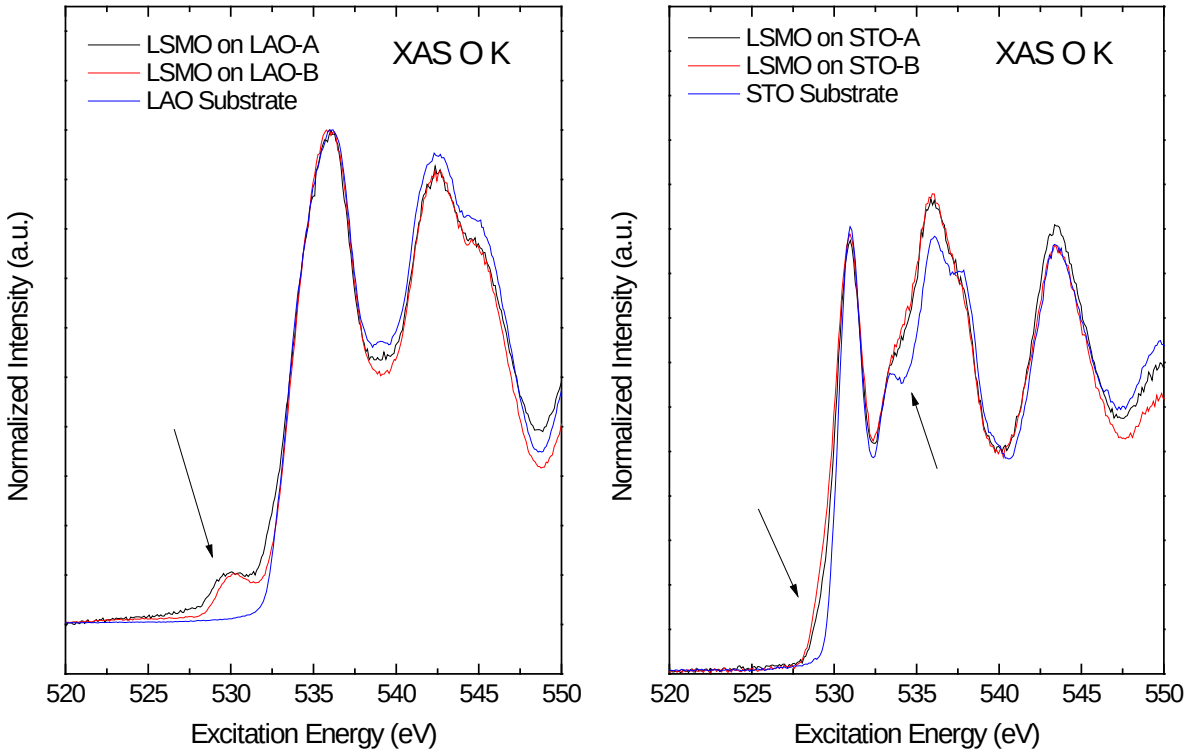

Figure 9. Comparison of XAS spectra of three LSM films on an $LaAlO_3$ substrate (left) or a $SrTiO_3$ substrate (right). Black and red spectra correspond to two different 10 nm $La_{0.8}Sr_{0.2}MnO_3$ films, while the blue spectrum was obtained for the respective bare substrate.

and red, while the spectrum of the bare substrate is shown in blue. It is apparent that the majority of the spectral structure found in the thin-film spectra stems from the underlying substrate. However, some clear differences are also visible. The main difference for the LSM films on LAO is the absence of the pre-edge feature (~530 eV, indicated by the arrow) in the substrate spectrum. The substrate also has a somewhat sharper absorption onset at 532 eV, in particular when compared to the LSM film LAO-A. We would like to point out a unique experimental opportunity that arises from the presence of the pre-edge feature and the fact that it is exclusively associated with the LSM film – when exciting resonantly into this absorption feature, it is possible to probe the oxygen-related occupied electronic states (with XES) *exclusively* for the LSM film, independent of the substrate. Furthermore, we point out that there is a clear difference in this pre-edge feature between the two different samples (–A and –B), indicating a sample-to-sample inhomogeneity.

Comparison of the LSM/STO and STO-substrate data (Figure 9, right) also shows a sharper onset at lower excitation energy (see arrow at ~529.5 eV). Even though this is not a clearly separate pre-edge feature as in the case of LSM on LAO, it is nevertheless the same LSM-related resonance that, with high-resolution excitation, can be used to predominantly probe the oxygen atoms in the LSM film (and not the STO substrate). Note that this resonant excitation is made more difficult by the fact that the absorption onset of STO is at lower energies than that of LAO. Furthermore, several features, in particular minima (see, e.g., the black arrow at ~534.5 eV), are “smeared out” for the thin-film samples as compared to the bare substrate. This indicates additional spectral contributions of LSM in these regions.

Summary

Surface-sensitive measurement techniques provide valuable insights into the active surfaces of $La_{0.8}Sr_{0.2}MnO_3$ (LSM) thin films, giving insights for the use of this material in SOFCs. In the network created by the SECA program, XPS measurements have provided valuable feedback to the growth and other characterization efforts. The close collaboration with CMU enables significant reductions of impurities in the LSM thin films. Results from MIT and CMU show that the crystallinity of the thin films depends strongly on the film thickness, while XPS measurements show that the surface composition does not. With this knowledge, we can ensure that results found on highly ordered thin films are also relevant for thicker films and infiltrated systems. The choice of substrates shows a significant influence on the surface termination of thin (10 nm) LSM films, as seen in the different Sr-C-O components.

Under this program, it has been possible to expand surface measurements, both XPS and XAS/XES, toward *in-situ* studies of the effect of temperature and atmosphere on the surface chemistry and electronic structure. The first of these studies shows no evidence of oxygen depletion or strontium segregation within the limited information depth of XPS measurements. Furthermore, the detailed investigation of all XPS signals reveals that also the La surface content is elevated and that Mn is significantly depleted. Temperature-dependent measurements have shown that the latter trend even continues upon heating. Therefore, the surface chemistry deviates significantly from the intended bulk composition. Several exciting avenues of investigation have been opened with the development of the *in-situ* capabilities and will be pursued as the program moves forward.